UNIVERSITÀ DEGLI STUDI DI PADOVA

Dipartimento di Fisica e Astronomia "Galileo Galilei"

Master's degree in Physics

Final dissertation

Characterization and commissioning of two large volume gaseuos Time Projection Chambers at CERN and JPARC laboratories

Thesis supervisor

Gianmaria Collazuol

Thesis co-supervisor

Stefano Levorato

Candidate

Camilla Forza

Academic Year 2023-2024

Where you invest your love, you invest your life.
Mumford and Sons - Awake My Soul

Contents

Abstract

T2K is a long-baseline accelerator neutrino experiment devoted to the study of neutrino oscillation physics. The experiment measures neutrinos from a ν_μ(or $\bar{\nu}_\mu$) beam produced at J-PARC accelerator and arriving at the far detector Super-Kamiokande. At 280 m from the production of the neutrino beam is placed the ND280 near detector providing flux models and constraints to correct cross section systematics. After a successful first phase of data taking, T2K temporary stopped its operation to prepare and install the beam and near detector upgrades. In this thesis, all the experimental efforts for constructing and testing two High-Angle Time Projection Chambers (HATPCs), which are part of the ND280 Upgrade, are presented and deeply discussed. In this context, I described the technical design of the T2K HATPC monitoring system I contributed to building and testing. A study on the drift velocity inside the HATPC is performed from cosmic ray data taken during the commissioning at CERN, where I was involved in the setup activities. The selection algorithm I developed permits to estimate the drift velocity directly from the detector itself without the need for dedicated external auxiliary detectors. In-depth studies of gas qualities and contamination models support the drift velocity measurement. Moreover, I described and analysed DUV laser tracks taken for calibration purposes. This preliminary study is crucial for optimizing the setup in preparation for an extensive laser data taking campaign planned for 2025. In the last part of the thesis, I summarize the installation of HATPCs at J-PARC and my work experience during the first neutrino run in December 2023 with the new upgrade detectors, opening the T2K second phase of data taking.

Introduction

The T2K experiment [1] is a long baseline accelerator neutrino experiment devoted to the study of oscillation neutrino Physics. The experiment first phase of data taking has been from 2010 to 2021, when it stopped for the preparation and installation of the beam and near detector upgrades. Now is operative again in the new configuration. In the first phase, T2K has successfully seen the appearance of ν_e in a beam of ν_μ [2], conducted measurements of the θ_{13} neutrino mixing angle, performed the current leading measurement of θ_{23} [3], and provided hints on CP-violation by measuring the δ_{CP} phase angle [4]. To confirm or not the CP-violation and to perform precise measurements of the PMNS matrix parameters, the T2K experiment is facing an upgrade phase. At the moment, the T2K neutrino beam and the Near Detector ND280 are respectively being upgraded to increase statistics and to provide constraints for reducing systematic uncertainties at the far detector. A new far detector, referred to as Hyper-Kamiokande [5], is being built with fiducial volume 8 times Super-Kamiokande [6] and will start taking data during 2027 profiting from the upgraded ND280 Near Detector.

The ND280 detector already finished the hardware upgrade [7]. The P0 detector has been removed and three new detectors have been placed in the same volume: the Time-of-Flight (TOF), an active plastic scintillator target called Super Fine-Grained Detector (SFGD), and two High-Angle Time Projection Chambers (bottom and top HATPC). The University of Padova and INFN are involved in the ND280 Upgrade project, in particular two large gaseous Time Projection Chambers (TPCs) have been assembled, characterized and calibrated at the CERN Neutrino Platform. The HATPC installation has been completed during Spring 2024 at the J-PARC laboratory (Tokai, Japan) and they have been fully integrated into the T2K ND280 Near Detector. The first data taking with the finalized ND280 upgraded apparatus has been recently completed.

During my thesis I joined the commissioning activities at CERN for the HATPCs and their installation at J-PARC.

In Chapter 3 I describe the technical design of the HATPC. The first part delves into the construction of the Field Cage (FC), including all necessary validation and characterization tests. The second part focuses on the ERAM detector, detailing its construction and the quality tests performed. Finally, I present my technical contribution to the assembled HATPC.

In Chapter 4 I focus on estimating the drift velocity from cosmic ray data. The initial part of the chapter is dedicated to the study of the performance needed by the re-circulation gas system, the analysis of the TPC out-gassing properties of the inner detector walls and to the analysis of the residual gas contamination. I describe the gas quality and its monitoring during the purging and data-taking phases. Specifically, for the purging phase, I check if gas-quality models are confirmed by data. In the second part, after summarizing

the trigger system for the cosmic rays data taking that I contributed to build. I present a selection algorithm that I developed to discriminate particle crossing the anode and/or the cathode. From the subset of data selected by the code, I could measure the drift velocity for each ERAM detector mounted on the endplates.

Furthermore, in Chapter 5, I present measurements of laser tracks conducted using a Nd:YAG Q-switching laser for calibration purposes. Initially, I describe the laser-induced charge production processes that generate tracks inside the HATPC. During the study of these laser tracks, an unexpected modulation in the time spectrum was discovered. One of the achievements of my thesis was successfully identifying the origin of this modulation. Afterwards, I analyzed laser tracks with the Principal Component Analysis (PCA) to estimate the beam spot size. Finally, I computed the drift velocity from laser runs. A series of runs were taken, varying the cathode voltage from 10 kV to 30 kV in steps of 2 kV.

At the end, in Chapter 6, I summarize the achievements of the Run 12. At J-PARC I joined the technical run in December 2023 (Run 12) where very early data were collected with the first neutrino beam on the upgraded ND280.

Chapter 1

Long-baseline neutrino oscillation physics

1.1 The PMNS matrix

Neutrinos are electrically neutral massive fermions interacting only via weak interactions with matter. There are three neutrinos, in the mass basis, that can be detected in the three flavour eigenstates ν_α of leptons, with $\alpha = e, \mu, \tau$, when interacting. They are determined as coherent superpositions of the three mass eigenstates ν_i, with $i = 1, 2, 3$, by the action of the neutrino mixing matrix, also known as Pontecorvo-Maki-Nakagawa-Sakata matrix U_{PMNS} [8][9][10]:

$$\begin{pmatrix} \nu_e \\ \nu_\mu \\ \nu_\tau \end{pmatrix} = \begin{pmatrix} U_{e1} & U_{e2} & U_{e3} \\ U_{\mu 1} & U_{\mu 2} & U_{\mu 3} \\ U_{\tau 1} & U_{\tau 2} & U_{\tau 3} \end{pmatrix} \cdot \begin{pmatrix} \nu_1 \\ \nu_2 \\ \nu_3 \end{pmatrix} \tag{1.1}$$

The flavor eigenstates can be expressed in the mass basis and viceversa exploiting the unitarity of the U_{PMNS} matrix. This feature allows the following formalism:

$$|\nu_\alpha\rangle = \sum_{i=1}^{3} U_{\alpha i} |\nu_i\rangle , \qquad |\nu_i\rangle = \sum_{\alpha=1}^{3} U^*_{\alpha i} |\nu_\alpha\rangle . \tag{1.2}$$

Wolfenstein parametrization

Usually the PMNS matrix in the Standard Model is expressed using the Wolfenstein parametrization originally developed for the quark sector [11]. The matrix terms depend on a total of four variables, counting three mixing angles (θ_{12}, θ_{13}, θ_{23}) and one phase angle δ_{CP}. The U_{PMNS} matrix can be rewritten by applying the parametrization and expressed as a product of matrices depending on the three mixing angles. The given formula holds in the vacuum:

$$\begin{pmatrix} \nu_e \\ \nu_\mu \\ \nu_\tau \end{pmatrix} = \begin{pmatrix} 1 & 0 & 0 \\ 0 & +c_{23} & +s_{23} \\ 0 & -s_{23} & +c_{23} \end{pmatrix} \cdot \begin{pmatrix} +c_{13} & 0 & +s_{13}e^{-i\delta_{CP}} \\ 0 & 1 & 0 \\ -s_{13}e^{i\delta_{CP}} & 0 & +c_{13} \end{pmatrix} \cdot \begin{pmatrix} +c_{12} & +s_{12} & 0 \\ -s_{12} & +c_{12} & 0 \\ 0 & 0 & 1 \end{pmatrix} \cdot \begin{pmatrix} \nu_1 \\ \nu_2 \\ \nu_3 \end{pmatrix} \tag{1.3}$$

In this way, the PNMS matrix results divided in three sectors. The first one describes the so called *atmospheric neutrinos* where parameters are measured from atmospheric and accelerator neutrinos in LBL experiments. The first measurement of θ_{23} has been performed by Super-Kamiokande detecting neutrinos generated by cosmic ray collisions

with the atmosphere [12]. At the moment, T2K has the leading measurement of this parameter [3]. The second sector contains the mixing angle θ_{13} and the phase δ_{CP}. Both these quantities are measured by LBL experiments, in addition, the θ_{13} angle can also be determined with reactor neutrinos. The measurement of θ_{13} has been made by Daya Bay [13] and RENO [14] experiments after the indication of possible non-zero values from T2K [2], while the δ_{CP} phase is measured by T2K [4] and NOvA [15] nowadays favoring the maximum violation and excluding the CP conservation at $\sim 2\sigma$. The last sector depends on the angle θ_{12} and describes the traditionally called *solar neutrinos*. The measurement of this angle has been made exploiting the solar neutrinos in the case of the Sudbury Neutrino Observatory (SNO) [16] and reactor neutrinos in the case of the KamLAND experiment [17].

Majorana neutrinos

For the following discussion, it is useful to recall the difference between a Dirac and a Majorana fermion. In the Weyl representation for the Dirac algebra, the Dirac matrices and the Dirac spinor can be written in the following way:

$$\gamma^\mu = \begin{pmatrix} 0 & \sigma^\mu \\ \bar{\sigma}^\mu & 0 \end{pmatrix}, \quad \sigma^\mu = (\mathbb{1}, \sigma^i), \quad \bar{\sigma}^\mu = (\mathbb{1}, -\sigma^i), \qquad \psi = \begin{pmatrix} \chi_L \\ \chi_R \end{pmatrix}, \tag{1.4}$$

where $\sigma^i,\ i = 1, 2, 3$ are the Pauli matrices, while χ_L and χ_R are respectively a left-handed and a right-handed Weyl two-component spinors. In the case of the Dirac fermion, these two spinors are independent objects, but in the case of a Majorana fermion, they are not, since the right-handed component can be defined in terms of the left-handed one. Indeed, a Majorana spinor in the Weyl basis can be written as:

$$\psi_M = \begin{pmatrix} \chi_L \\ C\chi_L \end{pmatrix} \tag{1.5}$$

where C is the Charge Conjugation operator acting on χ_L as follows:

$$C\chi_L = i\sigma^2\chi_L^*. \tag{1.6}$$

Therefore, we can see that a Majorana fermion has half of the degrees of freedom of a Dirac fermion, because a Dirac fermion has four independent components, while a Majorana fermion has only two. As a consequence for what concerns neutrinos, if these particles were Majorana fermions then we would have at our disposal a smaller number of degrees of freedom to reabsorb unphysical phases of the PMNS matrix with respect to the case of Dirac neutrinos. Hence, the parametrization of this matrix would count two more phases in the case of Majorana neutrinos. The PMNS mixing matrix for Dirac and Majorana neutrino are related by:

$$U_{Majorana} = U_{Dirac} \times \begin{pmatrix} 1 & 0 & 0 \\ 0 & e^{i\alpha_1} & 0 \\ 0 & 0 & e^{i\alpha_2} \end{pmatrix} \tag{1.7}$$

where α_1, α_2 are the additional phase angles.
Unfortunately, the neutrino oscillation phenomenon under investigation is not sensitive to these additional phases. Hence, experiments devoted to oscillation measurements cannot contribute to understanding whether the neutrino is a Dirac-type or a Majorana-type fermion.

1.2 Neutrino oscillation

The phenomenon of neutrino flavor oscillation is deeply related to the property of neutrinos to have mass. Non-diagonal elements of the mixing matrix are indeed different from zero, making the $U_{PMNS} \neq \mathbb{1}$.
In order to approach the oscillation problem, a neutrino detector is supposed to be placed at a distance L from a source of neutrinos with initial flavor α. In this configuration, neutrinos arrive at the detector at time t. Starting from 1.2 definitions, the oscillation probability can be computed as:

$$P_{\alpha\beta}(t) = |\langle \nu_\alpha(0)|\nu_\beta(t)\rangle|^2. \tag{1.8}$$

This formula describes the probability of detecting at time t (so at distance L) a neutrino of flavor β if at the time $t = 0$ its flavor was α. Since neutrinos oscillate, two probabilities can be defined: the survival probability (or disappearance of ν_α) and the conversion probability (or appearance of ν_β). Oscillation experiments measure these quantities by exploiting sources of reactor neutrinos or accelerator neutrinos, characterizing the flux in terms of the energy spectrum and flavor composition at the near detector. Counting in the far detector the events of neutrino of the same initial flavor and the oscillated one respectively the two probabilities can be computed.

N=2 flavors case Supposing to have two possible flavors α and β and a neutrino with energy E, the initial state at the source can be written as:

$$|\nu_\alpha(0)\rangle = U_{\alpha1}|\nu_1\rangle + U_{\alpha2}|\nu_2\rangle \tag{1.9}$$

The evolution of the state in time, considering again t as the time of arrival of the particle at the far detector, is

$$|\nu_\alpha(t)\rangle = U_{\alpha1}e^{-iE_1t}|\nu_1\rangle + U_{\alpha2}e^{-iE_2t}|\nu_2\rangle \tag{1.10}$$

The energies associated to the mass eigenstates are $E_{i=1,2} = \sqrt{p^2 + m_i^2} \approx E + \frac{m_i^2}{2E}$ with $E \approx p$.
From these definitions, in the ultra-relativistic limit where $L \approx ct$, the *survival probability* is defined as

$$P_{\alpha\alpha}(L) = |\langle \nu_\alpha(0)|\nu_\alpha(L)\rangle|^2 = 1 - 4|U_{\alpha1}|^2|U_{\alpha2}|^2 \sin^2\left[\frac{(m_2^2 - m_1^2)L}{4E}\right]. \tag{1.11}$$

The form of the mixing matrix in the case of N=2 is

$$U = \begin{pmatrix} \cos\theta & -\sin\theta \\ \sin\theta & \cos\theta \end{pmatrix}, \tag{1.12}$$

therefore, the formula 1.11 becomes

$$P_{\alpha\alpha}(L) = 1 - \sin^2 2\theta \sin^2\left[\frac{\Delta m_{12}^2 L}{4E}\right] \tag{1.13}$$

with $\Delta m_{12}^2 = m_2^2 - m_1^2$.
The *conversion probability* is given from the conservation of probability $P_{\alpha\beta} = 1 - P_{\alpha\alpha}$

$$P_{\alpha\beta}(L) = \sin^2 2\theta \sin^2\left[\frac{\Delta m_{12}^2 L}{4E}\right] \tag{1.14}$$

At the experimental level, the effect of neutrino oscillation can be preferably observed if the ratio $\frac{\Delta m^2 L}{4E} \sim O(1)$. The formula showing the order of magnitude of values for parameters, at which the phenomenon is visible, is:

$$\frac{\Delta m^2 L}{4E} \simeq 1.27 \times \left(\frac{\Delta m^2}{\mathrm{eV}^2}\right)\left(\frac{L}{\mathrm{km}}\right)\left(\frac{\mathrm{GeV}}{\mathrm{E}}\right) \tag{1.15}$$

N=3 flavors case A generalization of the 2-flavor case is possible starting from the evolution of the flavor states as follows:

$$|\nu_\alpha(t)\rangle = \sum_{i=1}^{3} e^{-iE_i t} U_{\alpha i} \, |\nu_i(0)\rangle \, . \tag{1.16}$$

The oscillation probability from a flavor α to a flavor β is given by

$$\begin{aligned} P(\nu_\alpha \to \nu_\beta) &= \left| \sum_{i=1}^{3} U^*_{\beta i} e^{-iE_i t} U_{\alpha i} \right|^2 \\ &= \delta_{\alpha\beta} - 2Re\left[\sum_{i>j} U^*_{\alpha i} U_{\beta i} U_{\alpha j} U^*_{\beta j} \left(1 - \cos \frac{\Delta m^2_{ji} L}{2E}\right)\right] \\ &+ 2Im\left[\sum_{i>j} U^*_{\alpha i} U_{\beta i} U_{\alpha j} U^*_{\beta j} \sin \frac{\Delta m^2_{ji} L}{2E}\right], \end{aligned} \tag{1.17}$$

where $\Delta m^2_{ji} = m^2_i - m^2_j$ and $\delta_{\alpha\beta} = \sum_i U^*_{\beta i} U_{\alpha i}$.

The expression of the probability found in this section considers the phenomenon occurring in vacuum. A more comprehensive treatment should also account for matter effects, however for the T2K experiment the contribution is very low, about 5% of the total probability.

1.3 CP violation

All the previous definitions are expressed considering only neutrinos, while in this section antineutrinos are taken into account. For this purpose, a Charge-Parity (CP) transformation is applied to the probability 1.17 to exchange each particle with its own antiparticle. Hence, the flavor oscillation appearance probability formula for antineutrinos is computed in the following way:

$$P(\nu_\alpha \to \nu_\beta) \overset{\mathrm{CP}}{\Longrightarrow} P(\bar{\nu}_\alpha \to \bar{\nu}_\beta) = P(\nu_\alpha \to \nu_\beta)(U_{\alpha i} \to U^*_{\alpha i}). \tag{1.18}$$

The CP symmetry is conserved for electromagnetic interactions and it is not observed in strong interactions, however experiments [18] showed that, in some rare cases where weak interactions are involved, the CP symmetry applied to the quark sector is violated. Whether this kind of violation is a feature also of the leptonic sector is still unknown. In 2020, the results of the T2K experiments indicated the possibility of CP violation in leptons. To study the presence or not CP violatiom the *Asymmetry* can be defined by exploiting the conversion probability for neutrinos and the one for the antineutrinos.

$$A^{\alpha\beta}_{CP} = P(\nu_\alpha \to \nu_\beta) - P(\bar{\nu}_\alpha \to \bar{\nu}_\beta) = +4Im\left[\sum_{i>j} U^*_{\alpha i} U_{\beta i} U_{\alpha j} U^*_{\beta j} \sin \frac{\Delta m^2_{ji} L}{2E}\right] \tag{1.19}$$

An important property of A_{CP} is

$$A_{CP}^{\alpha\beta} = -A_{CP}^{\beta\alpha} \qquad \rightarrow \qquad A_{CP}^{\alpha\alpha} = 0 \tag{1.20}$$

By definition, the asymmetry term for the disappearance is 0. Since the T2K experiment utilizes a beam of ν_μ and $\bar{\nu}_\mu$ peaked at 0.6 GeV, a useful expression to be given is $A_{CP}^{\mu e}$, which can be easily obtained from the definition 1.19 as

$$A_{CP}^{\mu e} = 16J \sin\left(\frac{\Delta m_{12}^2 L}{4E}\right) \sin\left(\frac{\Delta m_{23}^2 L}{4E}\right) \sin\left(\frac{\Delta m_{13}^2 L}{4E}\right), \tag{1.21}$$

where J is the Jarlskog invariant [19]:

$$J = c_{12}c_{23}c_{13}^2 s_{12}s_{23}s_{13} \sin\delta_{CP}. \tag{1.22}$$

In $P(\nu_\alpha \rightarrow \nu_\beta)$ the term violating the CP symmetry is sub-leading, so the effects have a very low probability to be observed (max 10% in T2K).

1.4 Neutrino mass ordering

In Section 1.1 the PMNS neutrino mixing matrix is defined in the case of 3 flavor eigenstates and 3 mass eigenstates. As can be appreciated from the observables defined in Section 1.2, neutrino oscillation experiments are sensitive only to the square of neutrino mass differences. An additional degree of freedom of the oscillation parameters is the fact that the mass m_3 can be larger or smaller than m_1. The issue is commonly referred as Neutrino Mass Ordering (NMO) problem. In Figure 1.1 [20] are graphically shown the three neutrino mass eigenstates in the two possible mass ordering. Experimental data from neutrino oscillation experiments provide the results shown in Tab. 1.1 for the PMNS matrix parameters. Two of the mass differences are also named $\Delta m_{12}^2 \equiv \Delta m_{sol}^2$ and $\Delta m_{23}^2 \equiv \Delta m_{atm}^2$, with $\Delta m_{ij}^2 = m_j^2 - m_i^2$.
In both the configurations Δm_{sol}^2 fixes $m_2 > m_1$ and the squared difference value is provided from experiments measuring solar neutrinos. The atmospheric neutrino data give instead two possibilities:

$$\begin{aligned} m_3 > m_1 \qquad &\rightarrow \qquad \Delta m_{13}^2 = \Delta m_{atm}^2 + \Delta m_{sol}^2 \quad \text{(NO)} \\ m_1 > m_3 \qquad &\rightarrow \qquad \Delta m_{13}^2 = \Delta m_{atm}^2 - \Delta m_{sol}^2 \quad \text{(IO)} \end{aligned} \tag{1.23}$$

The Normal Ordering (NO) occurs in the first case, while we refer to the Inverted Ordering (IO) in the second case.

Neutrino mixing parameters	
$\sin^2(\theta_{12})$	0.307 ± 0.013
Δm_{12}^2	$(7.53 \pm 0.18) \times 10^{-5}$ eV^2
$\sin^2(\theta_{23})$	$0.534^{+0.021}_{-0.024}$ (IO)
$\sin^2(\theta_{23})$	$0.547^{+0.018}_{-0.024}$ (NO)
Δm_{23}^2	$(-2.519 \pm 0.033) \times 10^{-3}$ eV^2 (IO)
Δm_{23}^2	$(2.437 \pm 0.033) \times 10^{-3}$ eV^2 (NO)
$\sin^2(\theta_{13})$	$(2.20 \pm 0.07) \times 10^{-2}$
δ_{CP}	1.23 ± 0.21 π rad

Table 1.1: Most updated values of neutrino mixing parameters from the PDG 2023 [11].

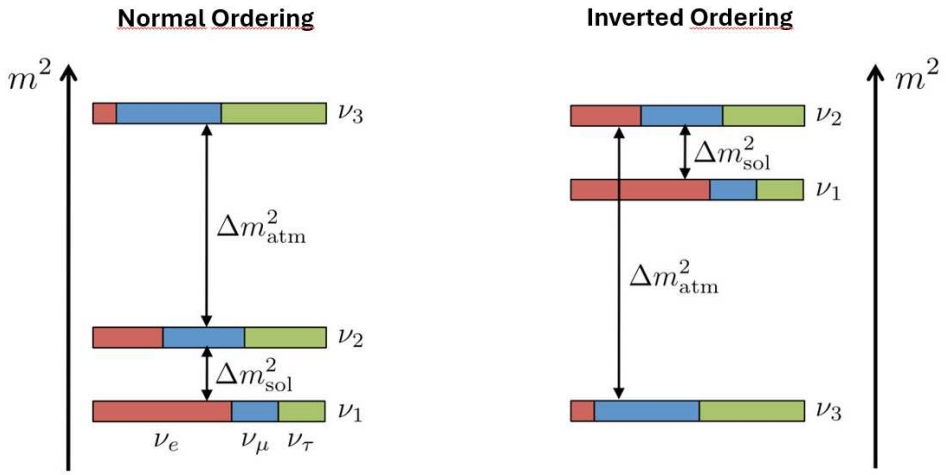

Figure 1.1: Neutrino Mass Ordering scheme with 3 neutrinos (ν_1, ν_2, ν_3) ordered from the bottom to the top increasing the mass magnitude. On the left is shown the Normal Ordering, while on the right is the Inverted Ordering. Each neutrino mass eigenstate is represented highlighting the probability of finding the neutrino in one of the three flavors: red for ν_e, blue for ν_μ and green for ν_τ.

1.4.1 Future experiments studying neutrino oscillation

Oscillation neutrino physics is significantly contributing to advancing our understanding of fundamental particle physics and the scientific community is investing in this research field. The possibility of CP violation in the lepton sector, as T2K is indicating, may help explain the matter-antimatter asymmetry in the Universe through leptogenesis. As challenging as the δ_{CP} measurement, the NMO problem is expected to be solved in the next decade by new experiments currently under construction.

Hyper-Kamiokande (HK)

Hyper-Kamiokande [5] (also referred to as Hyper-K or HK) is a water Cherenkov neutrino experiment which construction is ongoing under the Mt. Nijuugo, in Hida city, Gifu Prefecture, in the Japanese Alps. It is the successor of the Super-Kamiokande experiment and will be the far detector of the T2K experiment. It is designed for detecting neutrinos from many sources like atmosphere, the Sun, the Earth, supernovae and from the J-PARC accelerator neutrino beamline in the context of the T2K experiment. The detector will be a huge tank filled with 258 kton of ultrapure water (5 times SK) divided in Inner Detector (ID) and Outer Detector (OD). More than 20000 50 cm PMTs and 800 multi-PMTs will face the inside of the ID while the OD will be equipped with ∼3600 8 cm PMTs to provide the veto for the ID. Data collection is scheduled to begin in 2027. The physics program is very large and includes the search for the proton decay and the very precise measurement of oscillation parameters δ_{CP}, $|\Delta m^2_{32}|$, the sign of Δm^2_{32}, θ_{32} and θ_{31}. Among astrophysical goals, are the detection of supernova neutrinos providing warnings to other telescopes for multi-messenger observations, the detection of relic neutrinos and neutrinos from the Sun.

Deep Underground Neutrino Experiment (DUNE)

The Deep Underground Neutrino Experiment (DUNE) [21] is a long baseline neutrino experiment with a near detector to be installed at Fermilab and a far detector at the Sanford Underground Research Facility in the United States. The baseline is approximately

of 1300 kilometers. The data-taking will last more than 20 years, starting from 2032. Neutrinos are provided by the neutrino beam produced from the Main Injector accelerator at Fermilab with a power of 1.2 (up to 2.4) MW. Several subdetectors composing the near detector will be placed at 600 m from the beam production. The far detector exploits the Liquid Argon Time Projection Chamber (LArTPC) technology building 2(up to 4) modules for a total volume of 35(70) kton of liquid argon, installed at a depth of 1.5 km below the Earth's surface. DUNE claims to test the CP violation, to determine the NMO, to study supernovae neutrinos, and to search for the proton decay.

Jiangmen Underground Neutrino Observatory (JUNO)

Jiangmen Underground Neutrino Observatory (JUNO) [22] is a multi-purpose neutrino experiment in South China foreseen to start data taking in 2025. The detector under construction is an acrylic sphere surrounded by 18000 20" PMTs and 25000 3" PMTs that will contain 20 ktons of highly transparent liquid scintillator providing energy resolution better than 3% at 1 MeV. The experiment main goal is the solution of the NMO problem to be solved by detecting reactor antineutrinos ($\bar{\nu}_e$) at a distance of $\sim$ 53 km from the Yangjiang and Taishan nuclear power plants. After six years of data taking JUNO is expected to determine the NMO at 3-4 σ significance. JUNO will also be able to perform measurements of the solar neutrino oscillation parameters, $\sin^2\theta_{12}$, Δm^2_{21} and $|\Delta m^2_{32}|$, with a very high precision (subpercent level), improving the current measured values.

Chapter 2

The upgrade of the T2K experiment

2.1 The T2K experiment

The T2K experiment is a long baseline accelerator neutrino experiment devoted to the study of oscillation neutrino Physics. In the last decade, T2K took data from 2010 to 2021 when it stopped for the preparation of the second phase of data taking. The main results achieved in the first phase are the estimation of the θ_{13} neutrino mixing angle different from zero [2], the world best determination of atmospheric parameters [3] and of the δ_{CP} phase angle [4], giving hints on CP-violation in the leptonic sector. The experiment is composed by a near and a far detector, and it is located in Japan where the two main experimental sites are 295 km from each other. The neutrino beam is produced at the Japan Proton Accelerator Research Complex J-PARC laboratory in Tokai in the east part of Japan. The Near Detector (ND280) has been built in the same location, 280 m away from the production of the neutrino beam where the neutrino oscillation has not yet taken place. Characterizing the neutrino beam and measuring neutrino cross sections at the near detector is necessary to provide constraints for reducing systematic uncertainties at the far detector. The Super-Kamiokande experiment is situated underground, inside the Kamioka mines, on the west side of Japan and is the far detector. The journey of neutrinos is schematically represented in Figure 2.1.

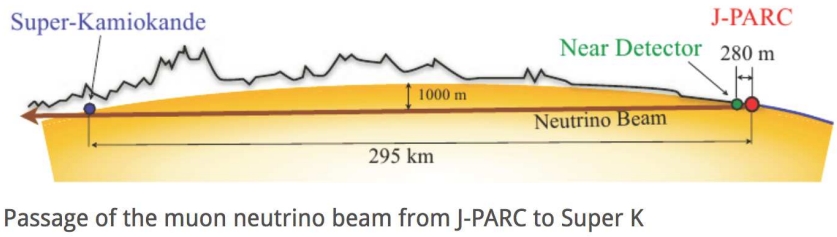

Figure 2.1: Schematic view of site locations.

In this section I will describe the original T2K experiment as it was before the upgrade phase to highlight the reasons behind the upgrade.

2.1.1 The neutrino beam

At the laboratory, the neutrino beam production starts in the Main Ring (MR) accelerator where protons are accelerated up to 30 GeV every 2 to 3 seconds before being directed inside the dedicated neutrino line. Two types of bunch extraction are possible, the slow extraction and the fast extraction, in two separated points of the MR. The first type directs bunches to the hadron beamline, the second one to the neutrino line. In the

fast extraction the spill consists of all the 8 bunches circulating in the MR, in this way protons are directed inside the neutrino line where the neutrino beam is produced. Once extracted from the MR, protons strike into a graphite target inside the target station producing mostly pions and a small fraction of kaons. The produced charged particles subsequently travel within a series of three horns where the charge selection is made, the beam is focused and the peak energy is chosen. The current inside the horns flows in one sense or in the other, depending on the necessity to run in neutrino mode or antineutrino mode. Supposing in this discussion to run the beam in neutrino mode, positive charged particles are selected. After the horns, the beam travels inside a decay volume where the greater part of the particles decay into muons and muonic neutrinos. At the end of the decay volume, at the most downstream end of the beamline, the beam is finally dumped in a stack of graphite blocks. All the particles (non interacted protons, non decayed mesons and muons) are stopped but neutrinos. A list of the most probable particle decays, producing neutrinos inside the decay volume, is presented in Table 2.1. Muons and kaons decaying inside the decay volume produce the greater part of the ν_e

Particle decay products	**Branching ratios (%)**
$\pi^+ \to \mu^+\nu_\mu$	99.9877
$\pi^+ \to e^+\nu_e$	1.23×10^{-4}
$K^+ \to \mu^+\nu_\mu$	63.56
$K^+ \to \pi^0\mu^+\nu_\mu$	3.352
$K^+ \to \pi^0 e^+\nu_e$	5.07
$K^0_L \to \pi^-\mu^+\nu_\mu$	27.04
$K^0_L \to \pi^- e^+\nu_e$	40.55
$\mu^+ \to e^+\bar{\nu}_\mu\nu_e$	100

Table 2.1: Most updated values of neutrino-producing decays and correspondent branching ratios from the PDG 2023 [11]. In this table the decay modes for $\bar{\nu}_\mu$ and $\bar{\nu}_e$ are omitted. Decay modes for π^-, K^- and μ^- are charge conjugates of π^+, K^+ and μ^+ respectively.

and $\bar{\nu}_e$ contamination in the beam which have to be considered in the flux model. In particular, the 48% of ν_e and the 90% of $\bar{\nu}_e$ are produced from kaon decays. The off-axis neutrino beam contamination is composed by 1.1% of ν_e, 6.1% of $\bar{\nu}_\mu$ and 0.1% of $\bar{\nu}_e$.
The beam performance in the first phase of data taking set the beam power up to 500 kW and the horn currents at 250 kA.
As already mentioned, the T2K experiment studies the flavor oscillation of neutrinos exploiting a near and a far detector placed at fixed distances. Neutrinos produced at the beam line have a momentum spectrum peaked at $\sim$1 GeV in the direction of the beam. The T2K experiment chose to place both the near and the far detectors 2.5° off-axis respect to the beam direction selecting the angle in order to work with a beam peaked at $E_\nu = 0.6$ GeV. Fixing the distance, the off-axis angle and the beam energy can be tuned to satisfy the following requirements:

- to narrow as much as possible the neutrino energy spread;
- to minimize $P(\nu_\mu \to \nu_\mu)$ and $P(\bar{\nu}_\mu \to \bar{\nu}_\mu)$, the survival probability;
- to maximize $P(\nu_\mu \to \nu_e)$ and $P(\bar{\nu}_\mu \to \bar{\nu}_e)$, the conversion probability;

With this configuration, the experiment mostly works with Charged Current Quasi-Elastic interactions (CCQE), which are the most recognizable and precisely measurable type of

interaction to be seen in Super-Kamiokande. Among these, the CC0π interactions, which do not involve the emission of a pion, are the most important:

$$\begin{aligned} \nu_\mu + n &\rightarrow \mu^- + p \\ \bar{\nu}_\mu + p &\rightarrow \mu^+ + n \end{aligned} \tag{2.1}$$

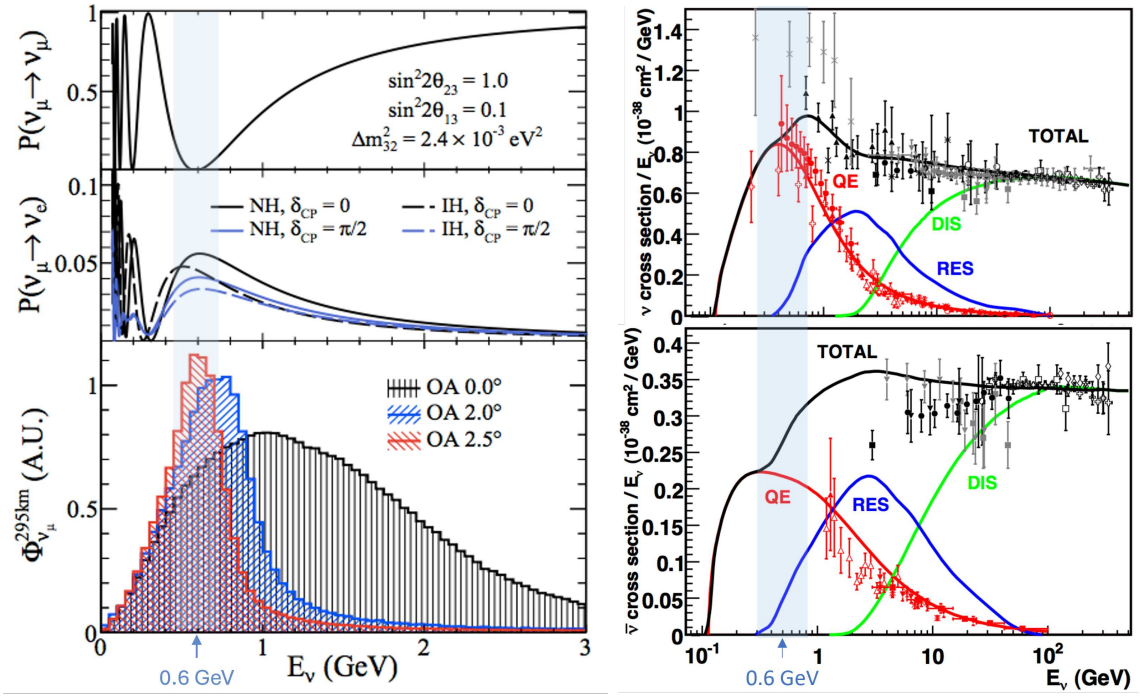

(a) (b)

Figure 2.2: (a): T2K neutrino flux at different off-axis angles compared with the ν_μ and $\bar{\nu}_\mu$ oscillation probabilities. (b): Neutrino and antineutrino cross section as function of the momentum. The light blue band indicates the momentum range of T2K beam at 2.5° off-axis.

The two plots (Figure2.2(a) and Figure2.2(b)) show respectively the energy spectrum of the neutrino beam, to be compared with the survival and conversion probability plotted above, and the cross-sections of both the neutrino and antineutrino interactions.

2.1.2 The ND280 detector

Placed 280 m far from the neutrino beam start, the ND280 detector is ~30 m underground inside a pit, together with the Interactive Neutrino GRID (INGRID) on-axis detector which is designed to measure the neutrino beam direction with a precision better than 1 mrad [1]. ND280 dimensions are defined by the UA1 magnet $(5.6 \times 6.1 \times 7.6)\text{m}^3$ enclosing the several sub-detectors working together to reconstruct neutrino interactions. A 3D view of the near detector complex is shown in Figure 2.3 together with a schematic picture of the ND280 sub-detectors.
The core of the original ND280 was a composition of detectors meant to optimally measure the kinematics of muons released in ν_μ or $\bar{\nu}_\mu$ interactions, in particular in the forward direction. The neutrino energy reconstruction is made exploiting the CCQE formula 2.2 that depends only on the kinematic of the muon ($p_\mu \cos\theta_\mu$).

$$E_{\nu_\mu} = \frac{m_p^2 - (m_n - E_b)^2 - m_\mu^2 + 2(m_n - E_b)E_\mu}{2(m_n - E_b - E_\mu + p_\mu \cos\theta_\mu)} \tag{2.2}$$

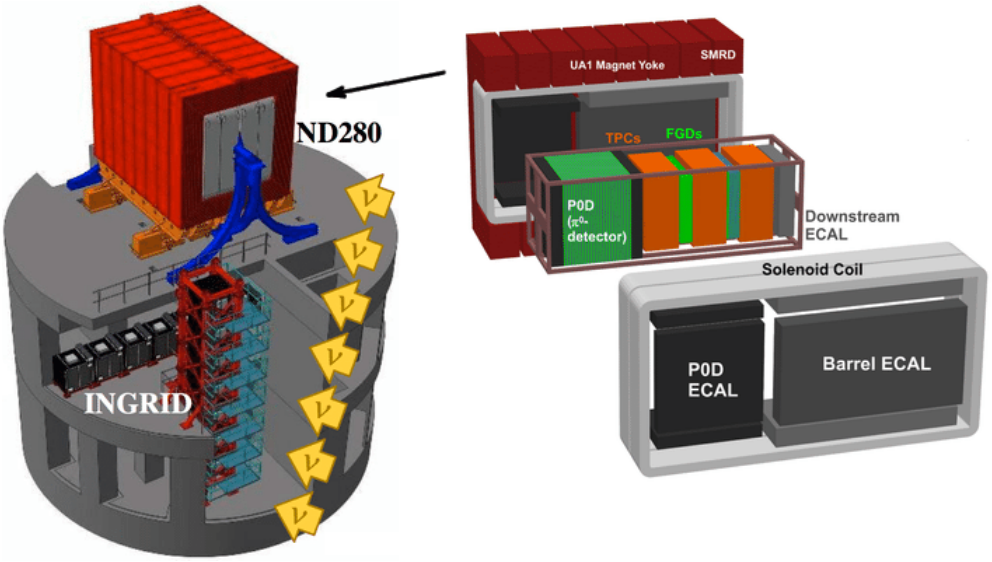

Figure 2.3: Schematic drawing of the Near Detector complex at the J-PARC laboratories. On the left, the ND280 and INGRID detector positions in the pit. On the right, the original detectors inside ND280.

The other constants m_p, m_n and m_μ are respectively the proton, neutron and muon masses together with the nuclear binding energy E_b.
The CCQE channel is not the only one studied at the near detector but it is the most frequent and cleaner channel to reconstruct the neutrino energy. The fraction of CCQE is $\sim$ 86%. The beam firstly arrives in the π_0 detector (P0D) [23], a scintillator target whose role was to reveal the presence of π_0, selecting good events in the channel CC0π. After the P0D, a sandwich of gas TPCs and scintillator active targets called Fine-Grained Detectors (FGDs) is placed to reconstruct the interaction vertex and the particle tracks produced in the neutrino interaction, in particular muons, and to study specific cross sections to provide constrains for the fit model at the far detector. One TPC [24] has a height of 2.5 m, a depth of 2.5 m and a width of about 1 m. The gas flowing inside is an argon-based mixture and electrons drift to the anode in a drift field approximately of 275 V/cm. On the readout plane twelve 34.3 cm $\times$ 35.9 cm Micromegas Modules (MM) face the inside of the volume and record the charge after a multiplication stage. The FGDs [25] are made of scintillator bars arranged in modules counting 192 bars in the x direction and 192 in the y direction for each module (see Figure 2.4). Each bar is coated with a reflective material and a wavelength shifting (WLS) fiber drives the light signal to a Multi-Pixel Photon Counter (MPPC) which senses and digitizes it. The FGD1 is made of fifteen modules while the FGD2 contains seven because six water targets are placed between the scintillator modules to measure neutrino cross section in water.
Finally, these sub-detectors are surrounded by an electromagnetic calorimeter (ECAL) and the whole volume is closed inside the UA1 Magnet Yoke providing a magnetic field of 0.2 T.

2.1.3 The Super-Kamiokande detector

Placed 1000 m underground (2700 m water equivalent) inside the Kamioka mines under the Mt. Ikeno, in the Gifu prefecture, the Super-Kamiokande (SK) [6] neutrino observatory is used by the T2K experiment as far detector. Since 1996 SK has been taking data detecting neutrinos from various sources and achieving great results. Excluding the

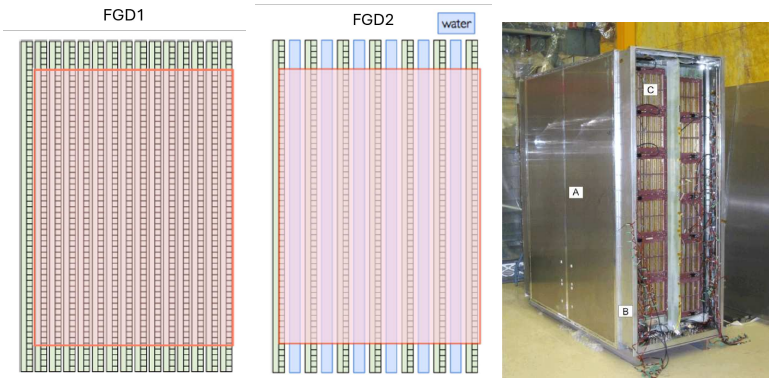

(a) (b) (c)

Figure 2.4: Lateral side view of the two Fine-Grained Detectors and a picture of one Time Projection Chamber. (a): FGD1 made of 15 xy-layers each one consisting of 192×2 scintillator bars. (b): FGD2 made of 7 xy-layers of scintillator + 6 water modules. The red area is the fiducial volume considered in the reconstruction analysis. [25] (c): Photo of one TPC [24].

results obtained within T2K, the list includes: the first evidence of neutrino oscillation in atmospheric neutrinos [12], the confirmation of the Solar neutrino detection and of the related flux deficit, the solar neutrino energy spectrum above 5 MeV [26], upper limits for the proton decay [27] and other significant measurements in astrophysics.

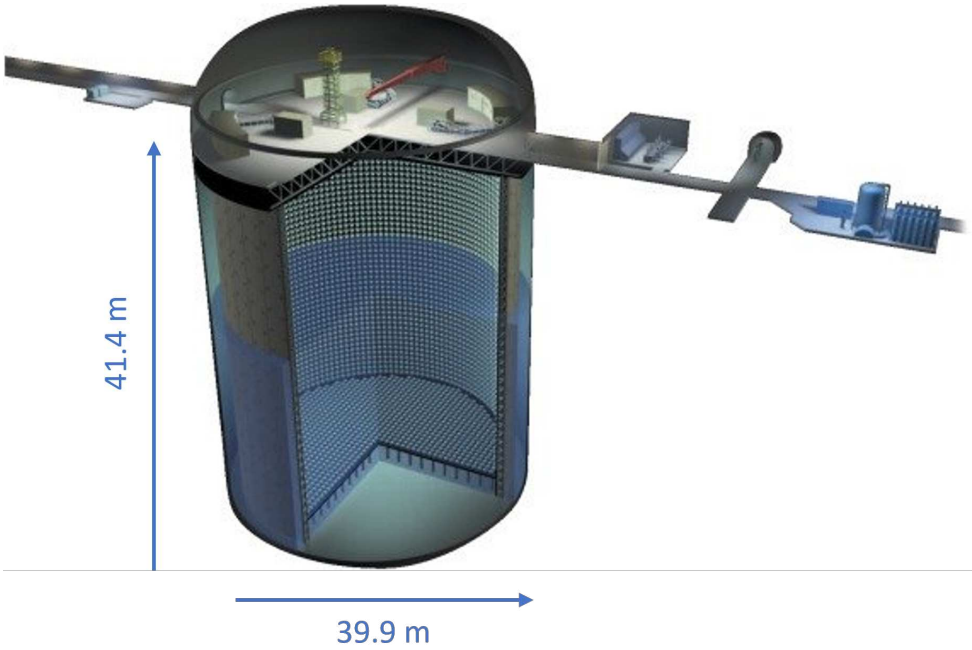

Figure 2.5: Drawing of the Super-Kamiokande detector.

As his predecessor Kamiokande (in the context of the proton decay), Super-Kamiokande in 2015 has been awarded of the Nobel Prize '*for the discovery of neutrino oscillations, which shows that neutrinos have mass*'. The detector itself is a water Cherenkov detector, specifically a huge cylindrical tank filled with water that has a diameter of 39.9 m and a height of 41.4 m, see Figure 2.5, divided in two regions, one inside the other: the Inner Detector (ID) and the Outer Detector (OD). It contains 50000 tons of ultrapure water divided in the ID volume of 32 ktons and OD volume of 18 ktons. More than 11000 20-inch PMTs face the inside of the inner region and are devoted to the readout of

the Cherenkov light in the ID, while 1885 8-inch PMTs face the outer region to identify incoming and outgoing charged particles, mostly muons, crossing the ID wall. A nominal fiducial volume of ~ 22.5 ktons is the region defined by a surface 2.00 m far from the ID wall taken into account for the analysis to minimize the anomalous response caused by natural radioactivity in the surrounding rock. In the last phase of data taking, Gd was added to the water in order to increase the neutron detection efficiency and better identify antineutrinos. The Cherenkov light emitted by a charged particle propagates in the transparent water projecting rings in the PMTs. The particle type is recognizable from the ring shape, but the charge is not directly measured from the projected rings. This latter information is derived by the detection of the scattered nucleon. Super-Kamiokande works as far detector in T2K counting the neutrino (or antineutrino) coming from the beam, identifying their flavor and measuring their energy. Data collected at the far detector are inserted in the fit model, corrected using the information given by the near detectors and compared with the non oscillated values to estimate the PMNS parameters.

2.2 The Upgrade

The T2K experiment stopped its first phase of data taking in 2021 for the preparation of the second phase including the installation of the upgrades. Searching for CP-violation confirmation, the upgrade involves both enhancing the neutrino beam power and installing new detectors in the ND280 complex. The beam luminosity is already significantly increased and will continue to grow in the next years, while the ND280 detector completed its upgrade and it is ready to take physics run. Together with the above mentioned changes, a new detector called WAGASCI-BabyMIND [28, 29] has been recently installed in the ND280 pit and measures the difference in cross sections from neutrinos interacting with water and scintillator targets with the help of a magnetic spectrometer.
The last step of the upgrade will happen at the end of 2027, when the T2K experiment will refer to the new Hyper-Kamiokande detector as far detector.

2.2.1 The beam upgrade

The J-PARC neutrino beam has been able to deliver till 2019 around 7.8×10^{21} Proton-On-Target (POT). The T2K collaboration proposed to extend the run by 5-6 years in order to reach the cumulative value of 20×10^{21} POT in the second phase of data taking. The foreseen MR beam power and integrated delivered POT in the next years are shown in Figure 2.6. The beam upgrade is ongoing and includes two parallel working areas. The upgrade of the MR accelerator and the upgrade of the neutrino beam line. The MR upgrade is also divided in two stages: in the first, already achieved, the power supply has been changed to increase the number of protons in each bunch, and the second stage is instead dedicated to increment the Radio Frequency (RF) of bunches. The beam power will pass from 500 kW to 1300 kW as the RF upgrade will be completed. In the run of Nov-Dec 2023 I was honoured to be in the ND280 control room when a milestone was reached stably running the beam at 760 kW together with the first tracks of neutrinos detected within upgrade detectors.
On the other hand, the neutrino beam line main upgrade is completed and consists in passing from 250 kA to 320 kA of current in the horns. This upgrade allows better selection and focusing at the meson production.
The final effect of the upgrade will be a high power neutrino beam peaked at 0.6 GeV in the T2K off-axis angle.

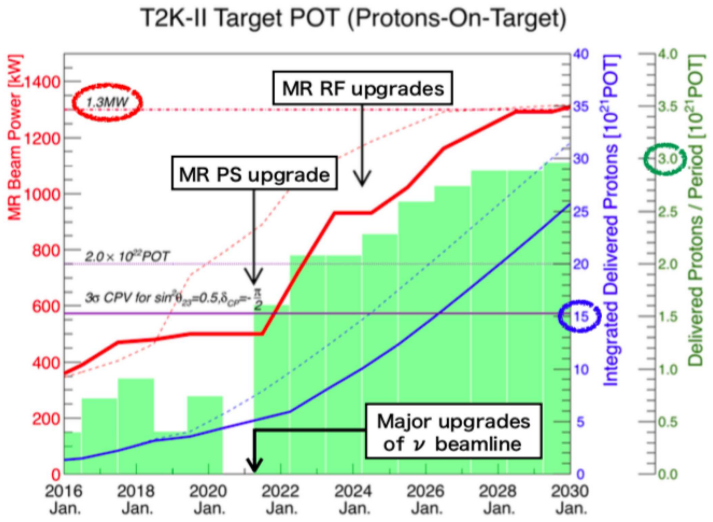

Figure 2.6: Simulation of the foreseen integrated Proton-On-Target for the next years. In the same plot, the phases of the beam upgrade are shown with the red line.

2.2.2 The ND280 upgrade

For the upgrade, the P0D is removed and in the same volume, inside the magnet, new detectors are placed. The new configuration includes a scintillator tracker called Super Fine-Grained Detector (SFGD), two High-Angle TPCs (HA-TPC) and the Time of Flight (ToF) [7]. The position of each detector inside the basket is shown in Figure 2.7.

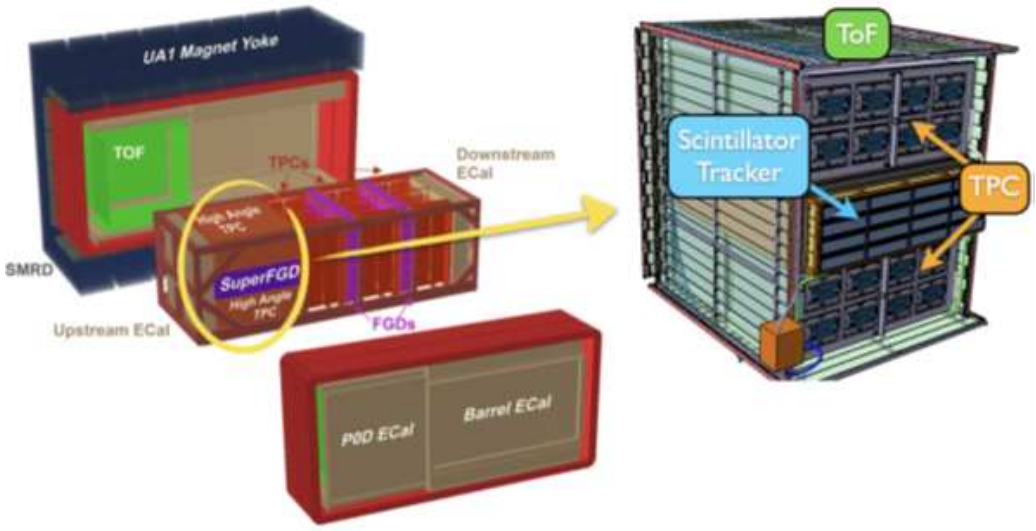

Figure 2.7: ND280 3D model highlighting the sector where the detectors for the upgrade will be installed.

Time of Flight

The Time of Flight detector is formed by six panels of plastic scintillator bars covering the SFGD and the two TPCs volume. It provides a trigger for cosmic muons and a precise timing reference for the upgrade detectors inside the basket volume. Each ToF module has a total active area of 5.4 m^2 and counts 20 plastic scintillator bars placed one next to each other. The size of each bar is $220 \times 12 \times 1$ cm^3 and the material choice settled on the plastic scintillator EJ200 due to its very good timing and optical properties, a

picture of the ToF panels is displayed in Figure2.8. The readout of each bar is made by 8 large-area SiPM (6×6 mm^2) placed at both ends. The required timing resolution for this detector is 0.5 ns to determine the direction of the particle crossing a layer, if the resolution is better than 0.2 ns the detector is able to contribute to particle identification. The achieved average resolution for one bar is 0.14 ns.

Figure 2.8: Picture of the ToF panels ready to be shipped to Tokai.

Super Fine-Grained Detector

The Super Fine-Grained Detector is the new active plastic scintillator target. It has a sufficiently large mass to provide a useful number of neutrino interactions (∼2 tons). The active volume dimensions are $192 \times 184 \times 56$ cm^3. Placed between the two HA-TPCs it is a 3D tracker with very high spatial resolution thanks to the 1 cm^3 scintillator cubes providing very high granularity. The SFGD has a fast intrinsic time resolution nominally around 0.6 ns for a minimum ionizing particle (MIP) due to the choice of the material. It is composed by more than 2000000 cubes of scintillating material read by 60000 WLS fibers in the three orthogonal directions. Each one of these cubes has a volume of 1 cm^3 and it is optically isolated being covered by a reflective layer of white polystyrene. The WLS fibers are inserted in the holes made in each cube and are read on one side by Multi Pixel Photon Counter (MPPC). The SFGD has a very good acceptance for charged leptons scattered with large angles from CC neutrino interactions. The low-mass material also permits the detection of low momentum protons and neutrons around the vertex detector. The shape of the detector is shown in Figure 2.9.

High-Angle Time Projection Chambers

The two High-Angle TPCs are large gaseous TPCs and are positioned on top and bottom of the SFGD. They are devoted to the detection of high angle scattered leptons identifying the particle type through the dE/dx information, measuring the transverse momentum and the charge thanks to the 0.2 T magnetic field provided by the UA1 magnet. The technical description of this detector will be extensively discussed in Chapter 3.

2.2.3 The impact of the upgrade

The original ND280 had an optimal configuration in detecting particles propagating in the forward direction with respect to the neutrino beam, while momentum measurements

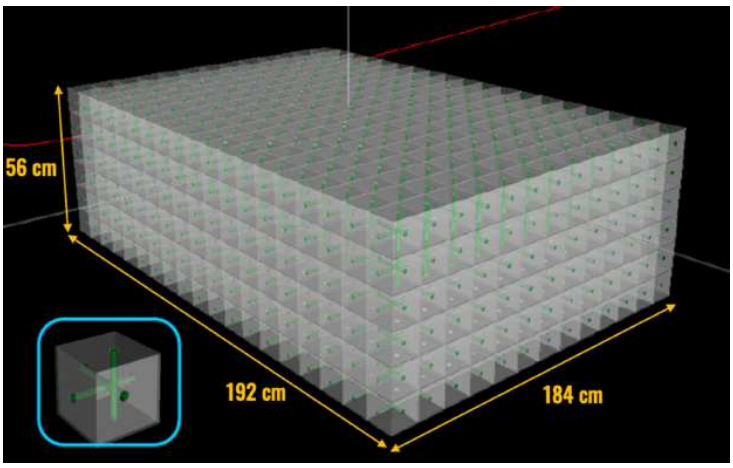

Figure 2.9: SFGD scintillator volume scheme. In the left corner there is a focus on one cube showing WLS fibers' positions.

of particles going backward or scattered at high angles resulted in low acceptance (e.g. high angle muon acceptance <20%). Before the upgrade, the vertex reconstruction was carried out only by the two FGDs. After the removal of the P0D and the installation of the SFGD, the active target mass is significantly increased. For what concerns systematic uncertainties in the energy reconstruction, estimated using the QE formula, they mostly come from the nuclear models considered to calculate the nuclear binding energy correction. With the new configuration of the ND280 detector a different estimator for the neutrino energy reconstruction, not directly requiring the information on nuclear models, will be available.
The impact of the ND280 upgrade can be summarized as follows [30]:

- Full 4π angular coverage (same as SK): higher efficiency and larger acceptance is expected for muons at high angles. The efficiency at high scattering angles will pass from less than 20% to $\sim$ 80% mostly thanks to the presence of the two HA-TPC. See Figure 3.1.

- Increasing of the proton detection efficiency. Setting a low momentum threshold for detecting protons (expected 300 MeV while it is 450 MeV in FDGs), the full final state in neutrino interactions (FSI) can be reliably measured.

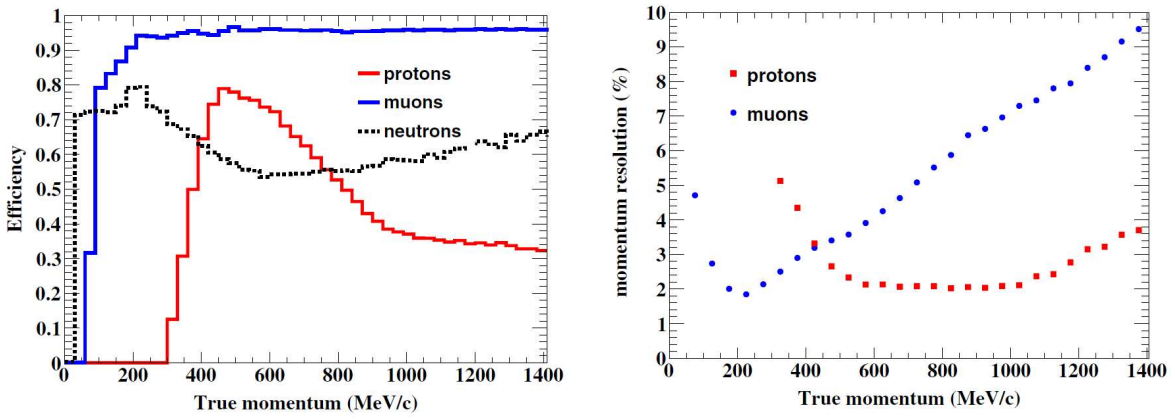

(a) (b)

Figure 2.10: In (a), the detection efficiency of protons, neutrons and muons. In (b), the momentum resolution for protons and muons in function of the true momentum [31].

- Capability to measure, not just tag, neutrons. Thanks to the high granularity of the SFGD, the 3D reconstruction of the neutrino interaction vertex and of the neutron second vertex is possible. Measuring the two vertex positions and the time of flight information, the SFGD will be able to measure the kinematics of neutrons.

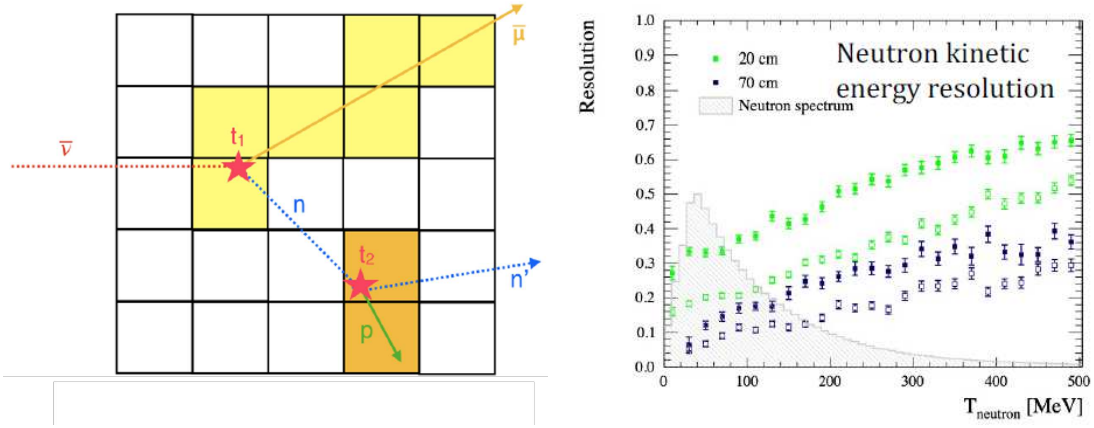

(a) (b)

Figure 2.11: The drawing in (a) is represented how the SFGD performs the measurement of the neutron time of flight thanks to its high granularity. In (b), the kinetic energy resolution for neutrons at different lever arms.

- Calorimetric estimators for neutrino energy can be used including the kinematics of the nucleons. The kinematics of the proton (or neutron) complete the reconstruction of the neutrino (or antineutrino) interaction giving the possibility to use the following estimator:

$$E_{vis} = E_{\mu} - T_N \tag{2.3}$$

where E_{vis} is the total visible energy of the detected outgoing particles, E_{μ} is the energy of the scattered muon and T_N is the kinetic energy of the nucleon. This type of estimator should not require corrections from nuclear physics, since it depends on the detector resolution and is not directly dependent on the nuclear model as in the CCQE formula.

Chapter 3

Technical design and construction of the ND280 HATPCs

Two High-Angle Time Projection Chambers are part of the ND280 Upgrade project and are positioned on bottom and top of the SFGD, inside the UA1 magnet. The already installed TPCs, similar to the new ones, have been very useful in the previous ND280 configuration providing crucial information for the event reconstruction and analysis. The role of a TPC inside the detector is to provide 3D reconstruction of particle tracks, charge measurement, momentum measurement, particle identification by combining dE/dx with momentum measurement. The possibility of measuring low-momenta tracks inside the TPC, as ones produced in neutrino interactions, is one of the key motivations for placing new TPCs below and above the SFGD.
The requirements to be matched for the new HATPCs are very similar to the old ones and include:

- dE/dx resolution better than 10% for all the incident angles and for all drift distances.
- Space resolution better than 800 μm.
- Since the ν_e flux is $\sim 1\%$, the electron and muon separation must be done properly to perform ν_e studies. The old TPC achieved a dE/dx resolution of 8% for minimum ionizing particles providing e and μ separation at 4σ. New HATPCs must satisfy at least the same requirement.

The two main differences from the old TPCs are the field cage structure and the readout detectors changing from bulk Micromegas technology [32] to resistive bulk Micromegas. The field cage has been manufactured with layers of very light materials in order to minimize the dead space still ensuring the structure robustness. The field cage detailed description is done in Section 3.1. Regarding the readout detector, the resistive anode technique improves the spatial resolution of the Micromegas spreading the amplified charge on a resistive layer and measuring the induced one with the pads. The resolution is enhanced without increasing the number of pads, so without increasing the electronic channels, actually decreasing them for the same readout area as described in details in Section 3.2.

The upgrade configuration has been chosen to improve the performance of cross section measurements, as already explained in Section 2.2.3. New HATPCs allow the detection of muons, scattered inside the SFGD, FGD1 or FGD2, at high angles with an improved efficiency from less than 10% to $\sim$50% at $\sim$90° muon scattered angle. Figure 3.1 shows

simulated values of the Charged-Current (CC)ν_μ selection muon efficiency as a function of the cosine of the scattering angle. The difference between the purple data, referring to the original configuration of ND280, and the blue data, including all the TPCs (old and new), shows a clear performance improvement. If also muons stopping in the SFGD are considered, the selection efficiency is steadily better than 70% as indicated by the data in green in the same plot.

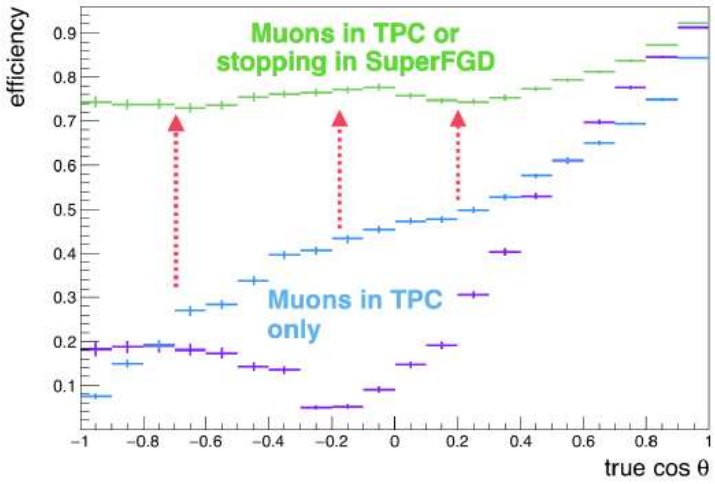

Figure 3.1: Charged-Current (CC)ν_μ selection muon efficiency plot.

The HATPC (top or bottom) dimensions are $2.0 \times 0.8 \times 1.8$ m^3 composed by two FCs divided by the cathode plane. They are filled with a dedicated gas mixture, known as "T2K mixture", mainly composed by Argon (Ar:CF_4:iC_4H_{10} - 95:3:2). A time projection chamber relies on the presence of an extremely uniform electric field keeping the detector working in drift regime. Charged particles from the neutrino interactions, or cosmic muons, ionize the gas inside the chambers. Electrons and ions do not recombine thanks to the electric field, which also allows them to drift towards the anode and cathode respectively. In a TPC, electrons drifting to the anode provide the spatial information about the original track: the measurement of the electrons impact position on the anode provides a 2D projection of the track image. The third dimension is obtained by multiplying the drift velocity and the drift time. Accurate 3D space reconstruction of the tracks is enabled by the uniform electric field: it guarantees a constant drift velocity inside the volume thanks also to the absence of electric field distortions. However, a small amount of moisture and oxygen gas contamination might respectively affect drift velocity and electron recombination. Thus gas properties must be monitored and checked regularly.

3.1 Field Cage

The total volume of one HATPC is $2.0 \times 0.8 \times 1.8$ m^3, divided in two symmetric FCs by the cathode plane. In Figure 3.2 a CAD sketch of the HATPC highlights the principal parts. Each drift volume corresponds to the dimension of the FC box, where the electric field is present and the tracks are generated by ionizing the gas. The FCs construction was in charge of INFN (Padova and Bari). The mechanical and electrical requirements to be matched include:

- to provide sufficient robustness to withstand gravitational and thermal loads, while ensuring reliable mechanical structure in overpressure conditions;

- use of light (low-density and low-Z) materials to build the FC and wall thickness resulting in less than 4% of radiation length in order to minimize multiple scattering and conversion processes occurring with the cage material;
- very high uniformity of the generated electric field, keeping field distortions small enough to displace primary electrons reconstructed position less than 0.2 mm and affect the momentum scale less than 2%;
- high gas tightness so that the permeability of O_2, N_2 and H_2O gases from air results in a contamination lower 10 ppm at the nominal flow of 300 l/h;
- a volume resistivity larger than 10^4 Ω cm and a surface resistivity larger than 100 T$\Omega\square$;
- high surface smoothness.

In this section I describe the Field Cage construction, the quality tests performed for its validation and the new HATPC monitoring system.

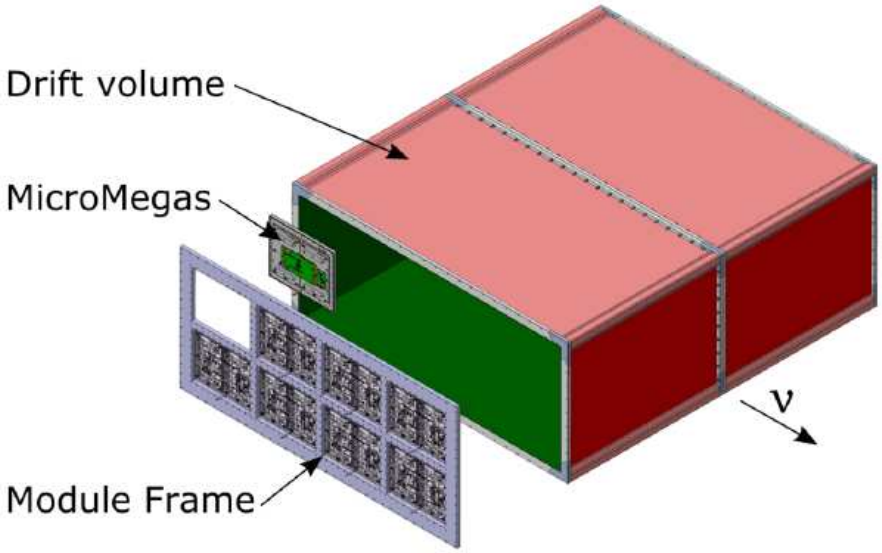

Figure 3.2: HATPC CAD drawing where the two drift volumes are divided by the cathode plane and the Micromegas are fixed to the module frame closing the HATPC at the anode side.

3.1.1 Field Cage construction

The Field Cage production was done by NEXUS (Barcelona, Spain), successfully managing to deliver 4 FCs to CERN satisfying the requirements and passing all the validating tests. As explained in the previous section, one HATPC is composed by two FCs.

Starting from an initial mold, layers of different materials are glued in sequence (Figure 3.3). The innermost layer is the strip foil, where two sets of copper strips, each 0.5 cm in width and 0.3 cm pitch, are separated by a 50 μm Kapton sheet: the field and the mirror strips. Both are devoted to generate and shape the electric field along the drift direction. The aim is to provide the most uniform electric field in the chamber and next

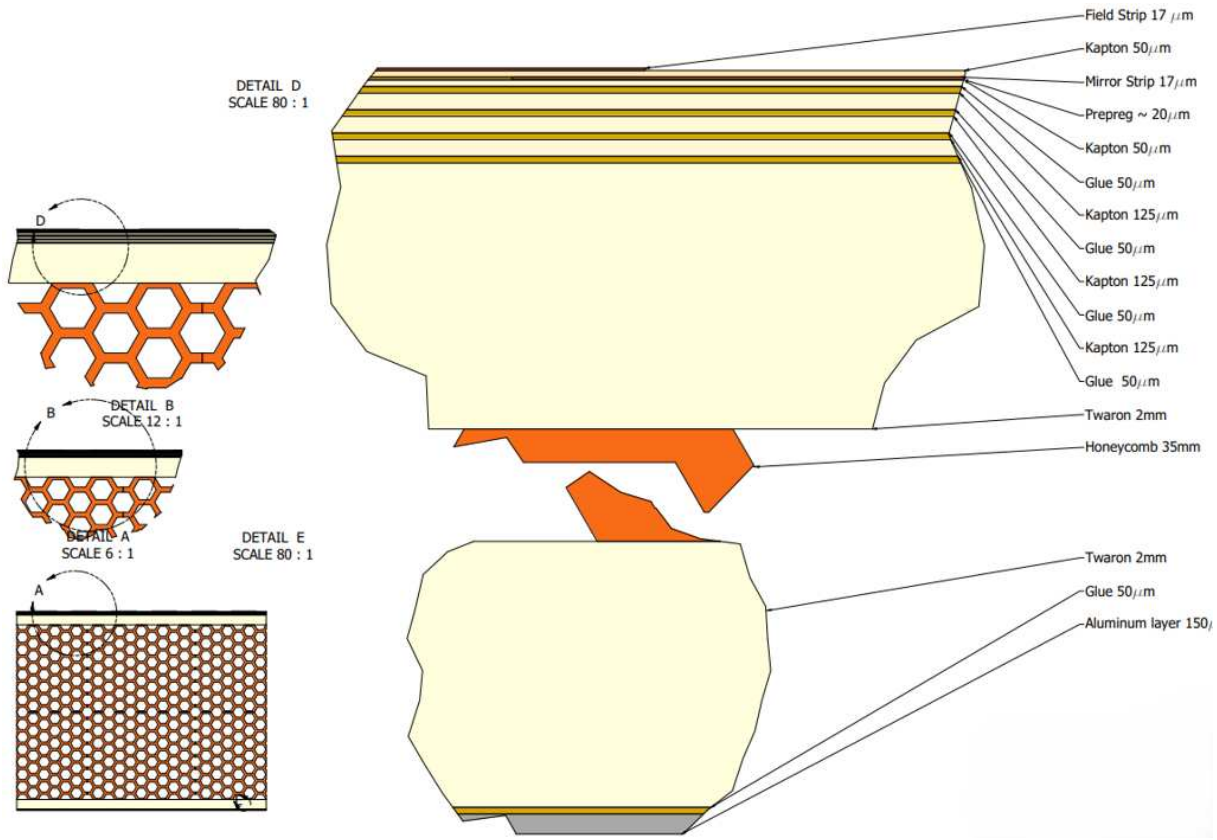

Figure 3.3: This CAD drawing shows how the layers are glued together and the proportional thicknesses between them.

to the walls. A total of 784 resistors of 5.1 MΩ were soldered at CERN, at the end of validating procedures, forming two dividers (392 for each) connected in parallel providing a $R_{eq} = 1$ GΩ, where R_{eq} is the equivalent resistance. The connection of both the field and the mirror strips is illustrated on the strip foil design in Figure 3.4.

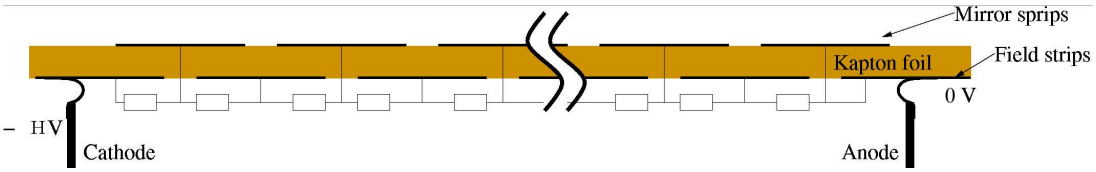

Figure 3.4: Strip foil scheme with resistor positioned facing the inside of the chamber.

Another 50 μm Kapton sheet, glued with Resoltech 1054 [33] insulates the mirror strips from the back. The strip layer has been made at the CERN laboratory of the Experimental Physics Detector Technology (EP-DT) section and then shipped to NEXUS. Three layers of 125 μm Kapton are subsequently glued together on the strip foils to form a ∼500 μm insulation thickness, realizing the first inner part of the FC walls. Once these steps are completed, the proto-FC is moved inside the autoclave, where the temperature is set to 100°C to harden the glue. After 6h the FC is taken out of the autoclave and prepared for the following steps. The robustness of the walls is obtained by a sandwich of materials glued together one after the other: 2 mm of Twaron, 35 mm of HoneyComb and again 2 mm of Twaron. These special materials were chosen for their strength, light weight and insulation properties. The corners are instead made of G10 (fiberglass) due to the presence of a very intense electric field in that part of the FC, where the field lines are denser.

In order to dry the glue, the FC is moved again inside the autoclave at 30°C, 6 bar for 12h.
Finally, one last Aluminum sheet (150 μm) is added via 50μm of glue covering all the FC outside surfaces to define the ground, i.e. the electrical closure of the TPC.
After this final step, each FC was shipped to CERN.

3.1.2 Field Cage quality tests

Once arrived at CERN, the FC undergoes a visual inspection to search for defects. The list includes the Kapton layer delamination from Twaron, the presence of air bubbles between the layers, electrical interruptions of the strips, the correct positioning and alignment of the strip foil.
From the inspection, no delaminations were found for all the FCs, while only a few little bubbles were identified and cured. This last process is of crucial importance since bubbles deform the electric field in the FC. The absence of interruptions along the path of each strip is verified through electrical continuity checks at the sheet junction and through dedicated vias for the mirror strips. No electrical interruption was found in the strips. Concerning the alignment of the strip foil, the relative displacement affecting the parallelism between the strip and the flange is minimal (< 100 μm over 2 m).

A series of tests were conducted to check the electrical properties:

- Measurement of electrical insulation between the external aluminum electrode and the field strips: a voltage of 10 kV is applied between all the field strips of the FC and the external aluminum electrode, while measuring the insulation as a function of time. A resistance larger than 1.4 TΩ has to be measured after 2 hours.

- Measurement of electrical insulation between the field strip and the mirror strip: the resistance is measured by applying 2.5 kV to 10 strips connected in parallel to other 10 strips, separated by 40 strips. A resistance larger than 4 TΩ has to be measured.

- Measurement of strip-to-strip insulation and verification of the absence of short circuits: an initial check of electrical insulation is done using a multimeter to identify any short circuits. In a second phase, resistance is measured using an insulation tester at 500 V to reveal resistive channels that may cause breakdown under operational conditions, as well as to exclude parasitic resistances comparable to the nominal 5.1 MΩ divider resistance.

After cleaning, testing and eventually curing procedures, resistors are soldered. Another important step to complete is metrology, and this measurement is conducted twice. The first measurement is carried out at NEXUS to verify dimensional conformity to the required specifications. The second measurement is performed by the Metrology Laboratory at CERN after the assembly of the module frame and cathode.
One last test to perform is the gas leakage measurement. The pressure inside the FC volume is raised to 20 mbar with respect to the atmosphere pressure and the value is monitored for some hours. Once corrected for the environmental condition changes, the leak rate has to be less than 5 l/h at 4 mbar.
After these tests, the FC is ready to enter the clean room and to be instrumented with the ERAM readout detectors.

3.1.3 The T2K HATPC monitoring system

During the construction phase of the two HATPC, I contributed to develop and test a system capable of monitoring the macroscopic parameters of the TPC gas, i.e. pressure, temperature, and relative humidity. The system monitors the same quantities for the environment and is completed by a dedicated high-resolution system able to monitor the HATPC resistive divider currents via an 18-bit ADC. The system has been fully developed via the Kikad[1] open-source software employing when possible commercial ready on shelf modules that later I have mounted and soldered on the PCB realized at the SCEN[2] company. The system complements the Gas Monitoring Chamber (GMC), and the ND280 gas systems, presenting several advantages: it provides all the monitored quantities online and for each of the TPC gas volumes indipendently.
A Raspberry PI-Pico-based microcontroller system [34] manages the communication via the I2C and SPI protocol with the peripherals, collects the data, send them via a Wiznet Ethernet interface to a Raspberry PI for the visualization and storage on the ND280 Global Slow Control (GSC). Dedicated alarms are implemented at the GSC level to trigger the operator/shift intervention during the data-taking in case of unexpected out-of-range measured values. The fast response of the system and the independent per each volume sensor sets enable fast and localized detection of the possible HATPC anomaly.

Technical design

The T2K HATPC monitoring system is built by four equal devices each for the four halves of the two HATPCs (top and bottom). Each device includes a set of sensors mounted on two separate Printed Circuit Boards (PCBs). One is placed inside the Aluminum box, visible in Figure 3.5 (a) and (b), fixed on the top left side of the Module Frame. The other is situated outside the TPC volume but inside the magnet. The devices are connected to a relay system that allows to control the powering of each of the 4 independent systems. The internal PCB hosts:

- a BME280 sensor from BOSCH [35] to measure internal pressure, relative humidity and temperature;
- a thermocouple K type, employed for its small thermal inertia;
- a PT100 NTC, employed for its large temperature sensitivity range;
- an infrared sensor for measuring the gas temperature at a different distance from the thermocouple;
- a white LED enabling the illumination of the TPC volume for the visual inspection of the inner volume through the 1-inch quartz window mounted on the sensor box.

On the external PCB a set of other sensors provides information about the environmental conditions outside the HATPC:

- a BME280 sensor [35] to measure internal pressure, relative humidity and again the temperature;

[1] www.kikad.org
[2] SCEN, Muggia, Trieste italy www.scen.it

- the MPU6050 from Sparkfun [36], a MEMS technology sensor working as accelerometer and gyroscope, providing the acceleration measurements in units of gravitational acceleration and the angular velocity in degree/s;
- a MCP3424 18-Bit ADC-4 to monitor the resistive divider current;
- a MAX31856 thermocouple-to-digital converter [37];
- a MAX31865 resistance-to-digital converter [38] for resistance temperature detectors.

The sensors use I2C protocol or the SPI interface and are connected to the microcontroller Raspberry PicoPI 2024. The Raspberry provides the clock, collects data and sends them to the computer via ethernet or USB connection, and checks the sensor status.
The microcontroller has been fully programmed via MicroPython code. The firmware can be remotely uploaded via the serial port even after the installation on the detector and magnet closure, for bug fixes or further developments.

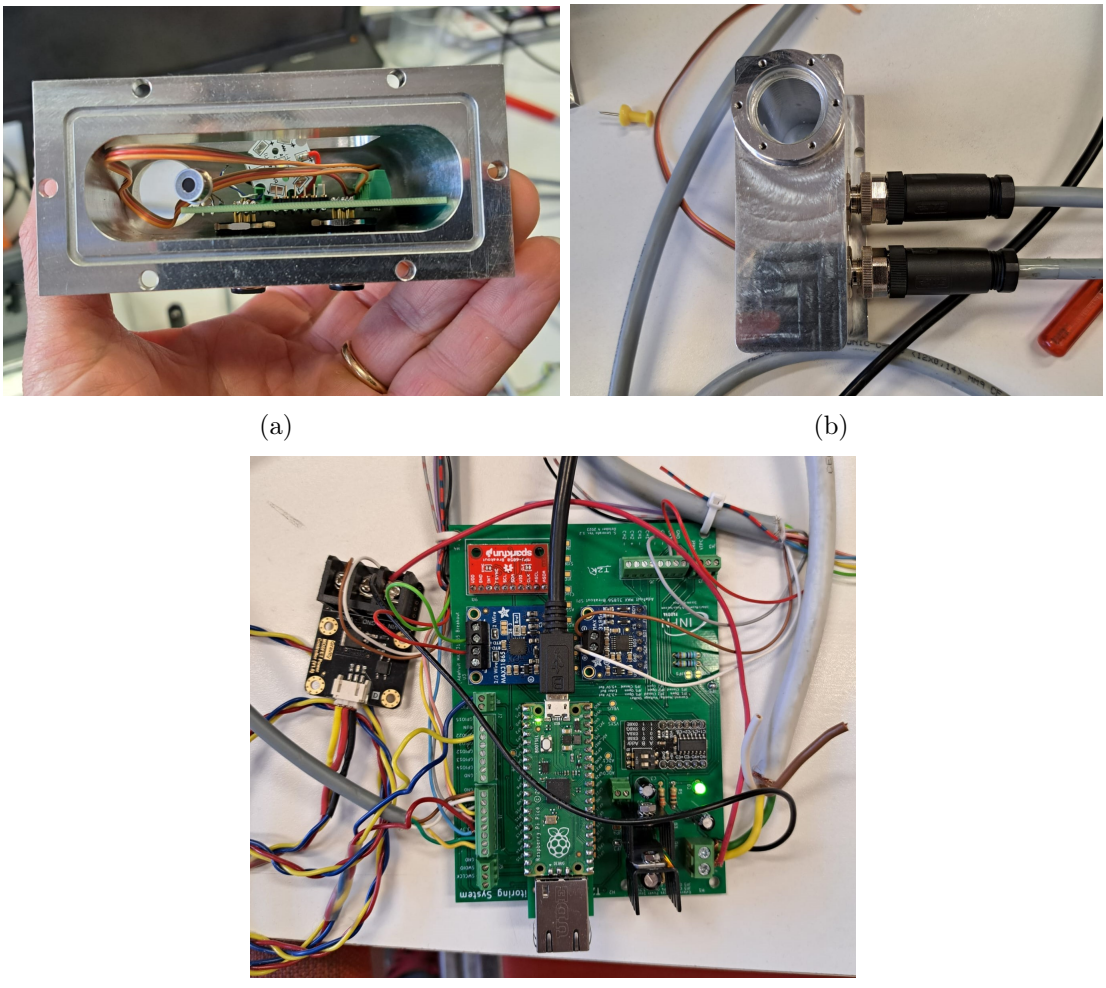

(a) (b)

(c)

Figure 3.5: The T2K HATPC monitoring system is shown in these three photos. In (a) and (b) the Aluminum box is seen from the inside of the TPC and from the outside respectively. In the first picture, sensors are clearly visible, while in the second there is a focus on the connectors. In (c) is shown the main controlling board of the monitoring system.

After completing the assembly of the four boards I have performed an accurate check of the performance, stability, digital communication and network communication. The

tests confirmed that all four monitoring systems were optimally functioning before the shipment to Japan. The technical scheme of the two PCBs circuits can be found in the Appendix (Figure A.2 and A.3).

3.2 Encapsulated Resistive Anode Micromegas (ERAM)

Once FC passes all the tests, resistors are soldered, the cathode and the module frame are assembled, and it is moved into a clean room where the ERAMs and internal monitoring sensors are installed. The readout electronics is already mounted on each ERAM before the HATPC instrumentation phase. The cooling system is assembled outside the clean room, and the connection to the gas system is also performed separately. In this section an overview of ERAM detector functioning, construction and characterization is presented.

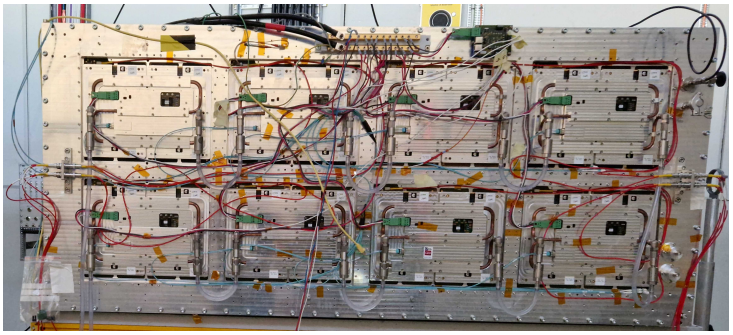

Figure 3.6: Photo of the one endplate equipped with all 8 ERAMs. The detectors are fully instrumented with the readout electronics, cooling system and all the cables.

The anode endplate of each half TPC is instrumented with eight Encapsulated Resistive Anode Micromegas (ERAM) modules, shown in Figure 3.6, providing the drift electron sensing and readout system of the TPC. Once collected, shaped and digitized, the signal is sent to the Trigger and Data Concentrator Module (TDCM) and then to the Data Acquisition system. The primary ionization electron created in the chamber drifts inside

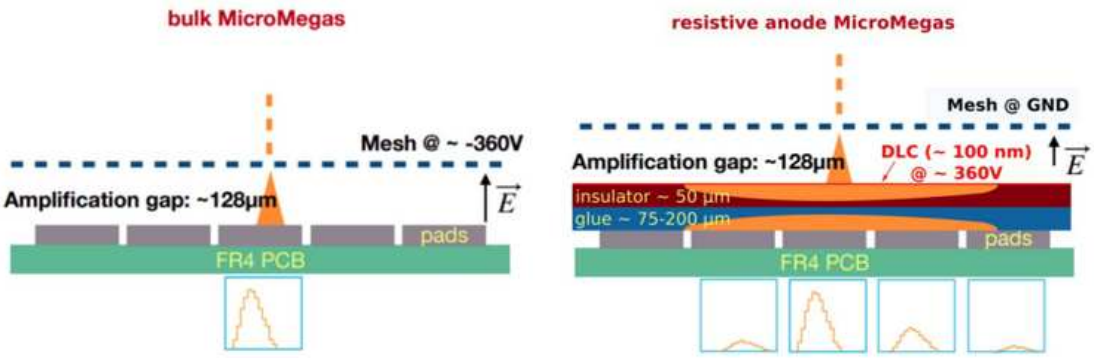

(a) (b)

Figure 3.7: In (a) the bulk Micromegas transverse section [32], in (b) the resistive Micromegas transverse section. On the bottom side of each drawing the number of involved pads is highlighted for a typical signal. In the resistive Micromegas the pad with the highest peak is the leading pad, while the others are neighbour pads.

the gas along the direction of the electric field till it arrives to the woven mesh, which is the anode of the TPC. After crossing the mesh, there is a space of 128 μm where a very

intense electric field O(30 kV/cm) is applied allowing an electron to develop an avalanche and, as a consequence, generate the detector signal. For the ERAM modules, developed using the former bulk-Micromegas technology and implemented in ND280 as read out of the vertical TPCs, the avalanche charge is directly collected by the pads, so that most of the times only one pad is involved in the charge collection process (See Figure 3.7(a)). For the new resistive Micromegas a resistive foil (50 μm thick) is located between the mesh and the pad layers. The resistive layer, which is set at positive potential, spreads the charge over the layer. A layer of glue underneath the resistive foil completes the necessary insulation over the sense pads (see Figure 3.7(b)). The charge moving on the resistive layer induces signal currents on the pads in such a way that for the avalanche several pads are involved. The possibility of using both the charge and time information of the leading pad, and the ones of the neighbour pads, leads to a better spatial reconstruction of the charge. This upgrade of bulk-Micromegas technology allows a more precise measurement of the xy-position without incrementing the number of readout channels (number of pads) with respect to the non resistive ones.
Better performance in terms of space and dE/dx resolution is achieved reading out in the same area with less pads than non resistive bulk-Micromegas. A further advantage of the presence of resistive layer improves the stability of the detector and protects the front-end electronics from sparks. As anticipated, the information on z position inside the TPC is provided by the measured drift time and drift velocity.

Having a homogeneous and constant drift velocity inside the gas volume is one of the most important requirements for a TPC. Therefore, in Chapter 4 I will present a method I developed to estimate the drift velocity for each ERAM using cosmic ray tracks.

3.2.1 Construction

CEA had the responsibility for the ERAM production, but it was carried out at CERN by the EP-DT-EF MPT workshop. The production starts from the PCB layer, which has a thickness of 2.21 mm, where the matrix of pads is placed. The size of the ERAM modules is 420×340 mm^2, counting a total of 1152 rectangular gold-coated copper pads disposed in a matrix with 36 pads in the x direction and 32 in the y direction. The area of each pad is 10.09×11.18 mm^2. The resistive layer is produced from a 50 μm Apical polyimide foil, which is an insulator. Diamond-Like Carbon (DLC) is deposited on the layer by electron beam sputtering providing a surface resistivity R about 400 k$\Omega\square$. In order to control the homogeneity of the DLC and tune the surface resistivity, an annealing process has been developed at CERN. It consists in a baking step inside an oven reaching higher temperatures with respect to the production step ones (200°C). The procedure permits to avoid the resistivity to drop the DLC resistivity of a factor $\sim$2 during the manufacturing process and can be easily reproduced for many foils. The best foils, in terms of homogeneity and R values, are used to build the ERAM.
The resistive layer is attached to the pad plane by pressing 150 μm of glue, glass fiber tissue filled with epoxy resin, forming an insulating layer. This layer determines the capacitance value C between the DLC and the pads, forming a continuous RC network.
The next step is the creation of the amplification gap: two 64 μm foils of photoresist are used to create a 128 μm layer on top of the DLC layer to space the woven stainless steel mesh from it. In this gap, the electrons arriving from the TPC are accelerated by the electric field, creating the avalanche. One last photoresist layer of 64 μm is placed over the mesh. A specific mask is used to image the photoresist surface and create the pillars. A chemical etching and demineralized water washing is used to remove the photoresist leav-

ing only the pillars. A baking step is required to harden the pillar. This procedure ensures very good parallelism of anode mesh and DLC layer, within the requirement specification.

A characteristics specific of the ERAM detector is the possibility to set the mesh at ground, while the DLC is set at high voltage. The working point is chosen to be ~ 350 V, depending on the mean gain value of the singular ERAM. A quality assurance test is performed before doing the last step of the production which is gluing the stiffener on the back side. The mesh pulsing test allows to quickly check for dead pads injecting a signal on the mesh and reading the output on the pads. If the ERAM passes this quality test, the aluminum mechanical stiffener hosting the front-end electronics is glued on the backside.
A precise mapping of the RC value on the full surface is the final quality step and I will talk about these measurements in Section 3.2.4. The presence of recursive patterns or very different RC values in different areas of the same ERAM is a reason for exclusion. A compromise between charge spreading, signal amplitude and detector stability must be taken into account.

3.2.2 Signal formation

The charge generated in the chamber by gas ionization drifts to the mesh, which is at ground, entering the amplification gap where the electric field forms an avalanche. The signal arrives to the resistive surface and spreads in all directions inducing a signal on the pads. The following diffusion equation models the spatial spread of the charge on the resistive layer:

$$\frac{\partial \rho(r,t)}{\partial t} = \frac{1}{RC}\Delta\rho(r,t) \tag{3.1}$$

where $\rho(r,t)$ is the charge density function depending on the radial distance and the time, R is the surface resistivity, C is the capacitance and Δ is the Laplace operator. The RC value of the leading pad, the initial charge and the neighbour pad position determine the magnitude of induced charged and the arrival time. A solution for the equation 3.1, supposing a charge arriving at $r = 0$ and $t = 0$ with a delta function profile, could be this Gaussian distribution:

$$\rho(r,t) = \frac{1}{2t/\tau} e^{-\frac{r^2}{4t/\tau}}, \qquad \text{with } \tau = RC. \tag{3.2}$$

A more realistic description of the charge spreading on the DLC is given by the following Gaussian distribution:

$$\rho(r,t) = \frac{Q_e}{2\pi\sigma^2(t)} e^{-\frac{r^2}{2\sigma^2(t)}}, \qquad \text{with } \sigma(t) = \sqrt{\frac{2t}{\tau} + \omega^2} \tag{3.3}$$

considering the initial charge distribution as a Gaussian with finite width ω and total charge Q_e and modeling the diffusion with a convolution of the two distributions. The charge induced on one pad below the resistive layer Q_{pad} is computed by integrating the distribution 3.3 over the pad area, which is rectangular. Finally, the charge signal model could be given taking into account the electronics response in the following convolution:

$$S(t) = Q_{pad}(t) \circledast \frac{d(ADC^D(t))}{dt} \tag{3.4}$$

where $\frac{d(ADC^D(t))}{dt}$ is the derivative of the electronic response function. The waveform shape is critical for understanding the charge distribution and timing information, essential for

accurately reconstructing the tracks of particles passing through the detector. In Figure 3.8 some examples of simulated waveforms.

Another important quantity is the gain and it is defined as:

$$G = \frac{Q_{Anode}}{Q_{Primary}} \tag{3.5}$$

where Q_{Anode} is the charge arrived at the resistive anode and $Q_{Primary}$ is the initial charge produced by a particle ionizing the gas. A valid method to compute the Q_{Anode} is considering the waveform of the leading pad, the one with the highest peak, and sum the waveforms of the 8 neighbour pads around it. Taking the maximum of the resulting waveform (ADC^{Σ}_{max}) and converting it to a charge, the gain becomes:

$$G = \frac{Q^{\Sigma}_{max}}{Q_{Primary}} = \frac{ADC^{\Sigma}_{max}}{ADC_0}\frac{Q_0}{Q_{Primary}} \tag{3.6}$$

This method relies on the assumption that the charge spreading on the resistive layer over the nine selected pads is constant within the time scale of the electronics response.

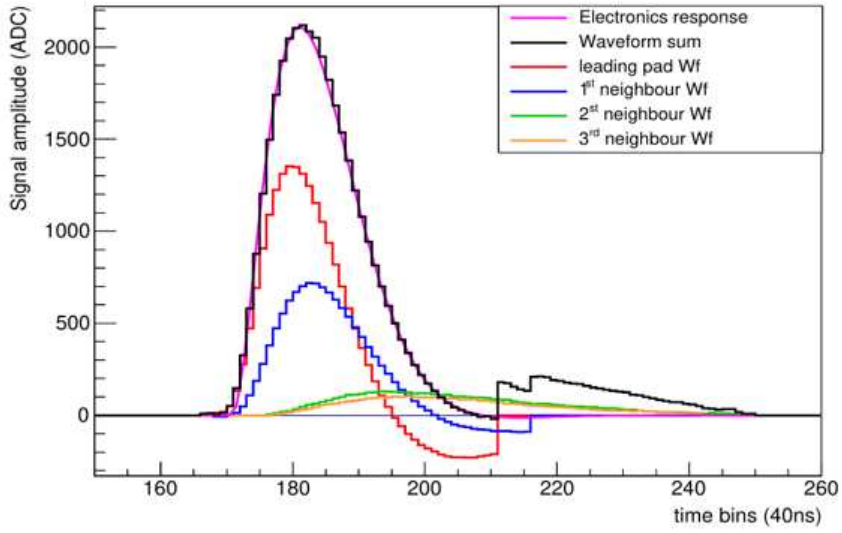

Figure 3.8: Plot of the expected shape of waveforms generated for one ERAM pad.

3.2.3 Readout electronics

The ERAM detector readout electronics is fixed directly on the PCB where the pads are located. It relies on the AFTER chip already used for bulk-Micromegas of the vertical TPCs. This chip reads the charge of 72 pads arranged in a matrix 8×9, so a total of 16 AFTER ASIC chips are needed to read one ERAM. The ASIC operates at the sampling frequency of 25 MHz and maximum ADC counts (4096) corresponds to the full charge range of 120 fC. The peaking time can be set to 200 ns or 412 ns.
A Front End Card (FEC) hosts 8 AFTER chips, hence, two of them are necessary to operate all the AFTER chips. Finally, the Front End Mezzanine (FEM) synchronizes signal digitization by distributing the clock, previously provided by the TDCM, to the two connected FECs. The two FEM cards dedicated to the two halves of the HATPC send the data from ERAMs to the TDCM. The temperature of electronics is controlled by a water cooling system circulating cold water from a chiller inside copper pipes, attached through aluminum plates to the backside of the ERAM module.
In Figure 3.9 the assembling sequence is shown.

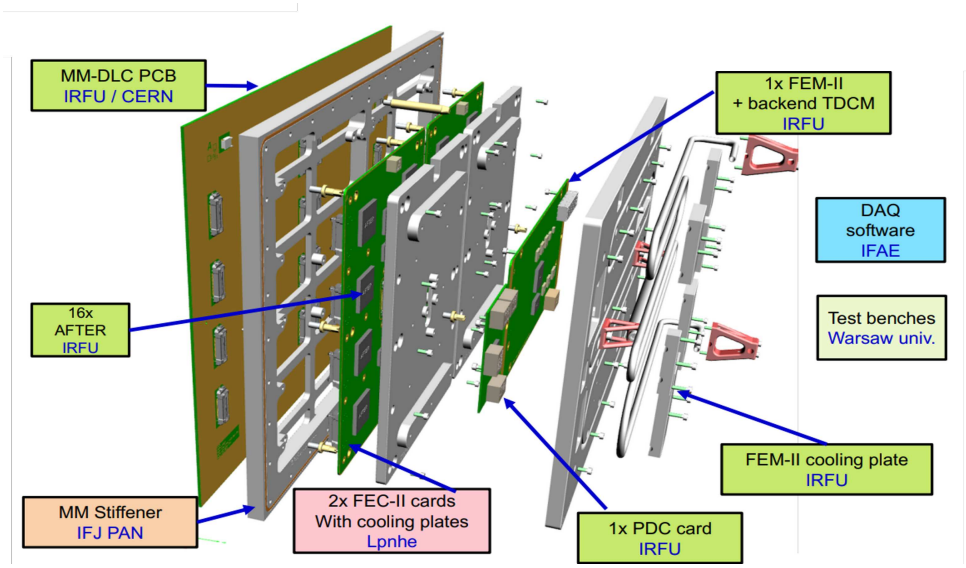

Figure 3.9: CAD-based drawing of the electronics fixed on the backside of the ERAM.

3.2.4 ERAM characterization

These new detectors have undergone a rigorous phase of characterization and calibration. The characterization phase is fundamental to ensure the quality of the detectors, to study the response and to provide data for calibration.

Mesh pulsing

Once a detector is delivered, the first step is to spot any electrical or geometric defects before gluing the Aluminium stiffener on the backside. This is performed by injecting on the mesh, this is possible thanks to a connector on the PCB allowing to connect the mesh to ground during normal operation or to a signal generation. The signal on the mesh is inducing a uniform signal on the whole readout plane. Performing the readout of each pads and comparing the average maximum amplitude and the standard deviation of each waveform allows to detect if one or several pads have issues. On the figure 3.10, one can see two examples of issues. The first one is a pillar not well glued on the DLC, while on the second one it is a bunch of noisy pads. This is usually indicating that pads are connected two by two providing a noise level twice higher. In both cases it has been solved by sending back the detector to the manufacturer. The criteria applied in order to accept or not a detector are the following:

- Not more than four dead pads and not adjacent.
- A non-uniformity of the pad signal amplitude of 15%.

If the detector is accepted then the stiffener is glued on its backside and is stored in the clean room waiting to be scanned on the X-ray test bench.

ERAM characterization using X-rays from ^{55}Fe source

Each ERAM module has been tested and characterized before being chosen and assigned to a specific position on the endplate, or selected as spare. The goal was to scan the pads to reconstruct the RC mapping and a gain mapping. This characterization step is of utmost importance to have a precise knowledge of the detector response. A dedicated experimental setup has been built for this task. A test bench has been developed to

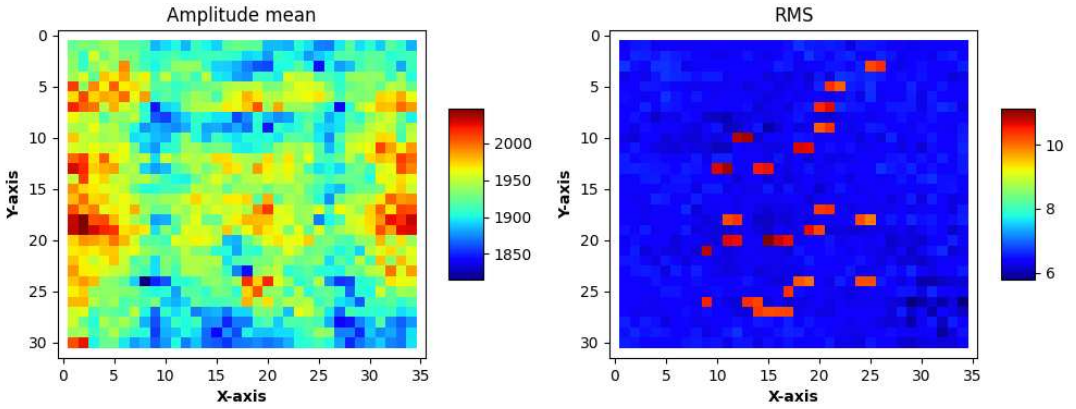

(a)

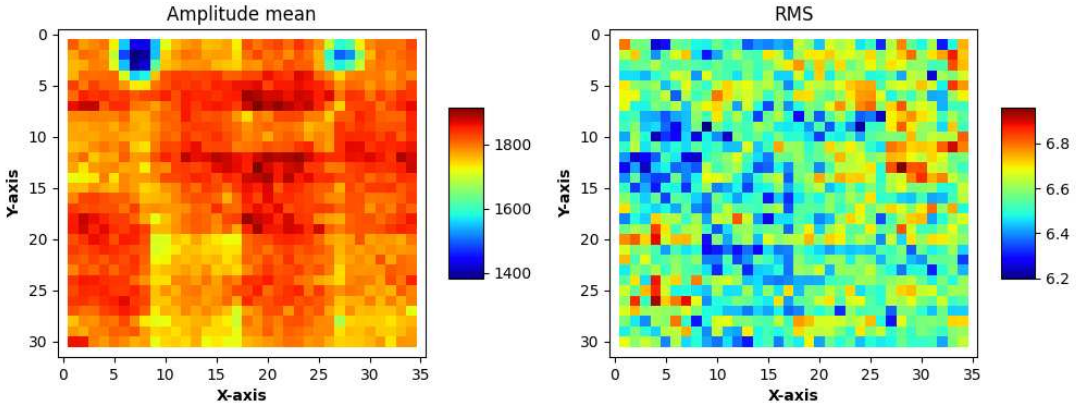

(b)

Figure 3.10: Results of the mesh pulsing tests with the amplitude and the RMS of signal displayed for each pads. On the figure (a) one can see lot of noisy pads that have the double of the expected RMS values. On the figure (b) one can see a region with a lower amplitude, indicating a pillar not well connected to the DLC. In both cases, it has been solved after sending the detector back to the manufacturer.

characterize the ERAM scanning each pad with X-rays produced by a 280 MBq ^{55}Fe radioactive source. In Figure 3.11 a photo of the setup is shown. The ERAM is fixed to an aluminum chamber filled with T2K gas providing a drift distance of 3 cm. The ^{55}Fe source is located inside a specific box, fixed to a movable mechanical arm, equipped with a collimator orthogonal directed respect to the pad plane. A Mylar foil covered with aluminum lets X-rays enter the chamber and a mesh, working as cathode, generates the necessary electric field in the drift volume. The DLC voltage is set to 350 V, while the ERAM mesh is at ground. The mechanical arm step of 0.1 mm permits a very precise alignment of the source with the center of each pad.

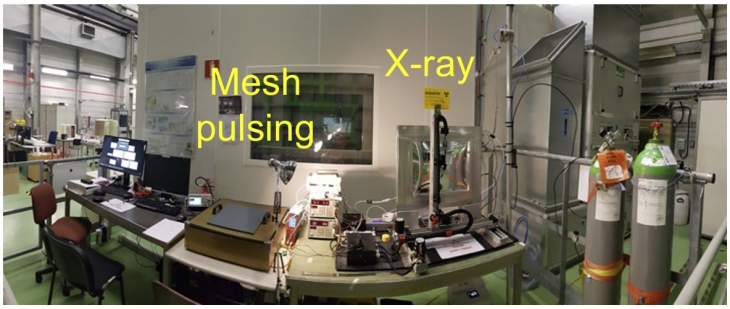

Figure 3.11: Photo of the Test Bench with X-ray setup.

This method allows to estimate the RC and the gain values for each pad. In Figure 3.12 there is an example of RC and gain mapping for one ERAM measured with the ^{55}Fe source, where the two quantities are calculated following the method explained at the beginning of Section 3.2.4.

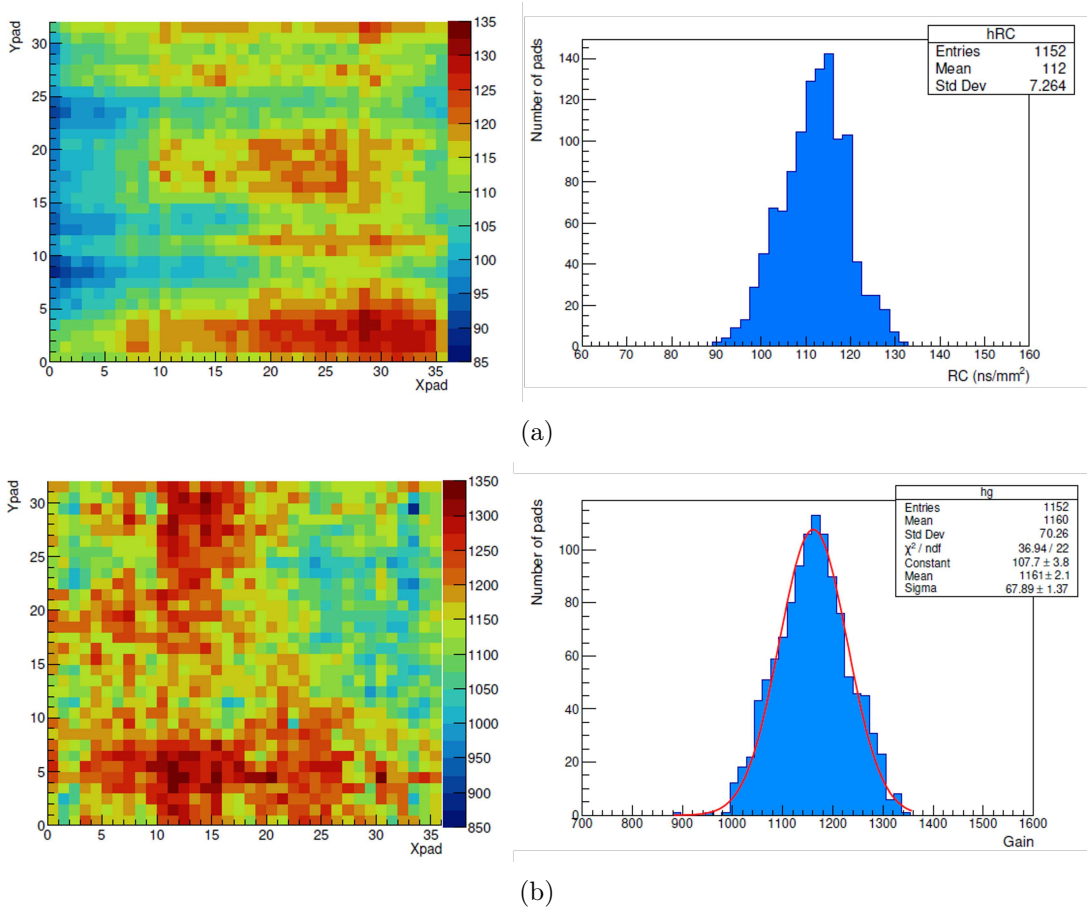

Figure 3.12: Test bench measurements with^{55}Fe (a) RC map of ERAM 30 on the left and the distribution of single pad RC values on the right, (b) gain map of ERAM 30 on the left and the distribution of single pad gains on the right.

Test Beam 2022

In Summer 2022 a full scale FC, also referred to as the "Mock-up", has been illuminated with particle beams during a two week "Test Beam" period [39]. The purpose was to simultaneously test 8 ERAMs with straight particle tracks from a beam, while also having the capability to select particle momenta. Since it was the first time with 8 ERAMs working together, the test beam also provided an opportunity to test and optimize the DAQ system. Previously, another test beam was conducted at DESY where only one ERAM was tested attached to a small prototype [40].
A specific experimental setup was built in the available area to safely switch on the detectors and provide different triggers for the the different particles. In this test beam campaign the setup of scintillators for the trigger was a task under my responsibility and I put in a lot of effort into setting up the trigger system with NIM modules together with colleagues. Together with the "Mock-up" TPC under test, the setup (see Figure 3.13 and 3.14) included the following ancillary detectors: 2 threshold Cherenkov detectors, 2 scintillator pads (included within the beam instrumentation), 4 plastic scintillators readout by PMTs and a Cherenkov Lead Glass block (positioned before the last scintillator

along the beam line). Some iron blocks were located in front of the Lead Glass block for filtering out electrons and tagging μ and π.

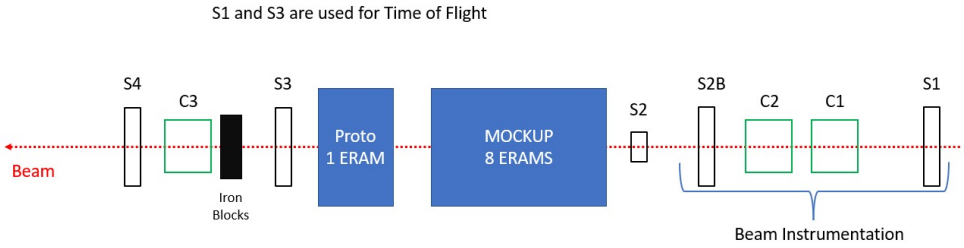

Figure 3.13: Test beam setup scheme: S1, S2, S2B, S3, S4 are scintillators, C1, C2 are gaseous Cherenkov detectors, C3 is a lead-glass Cherenkov detector, in blue the TPCs under test.

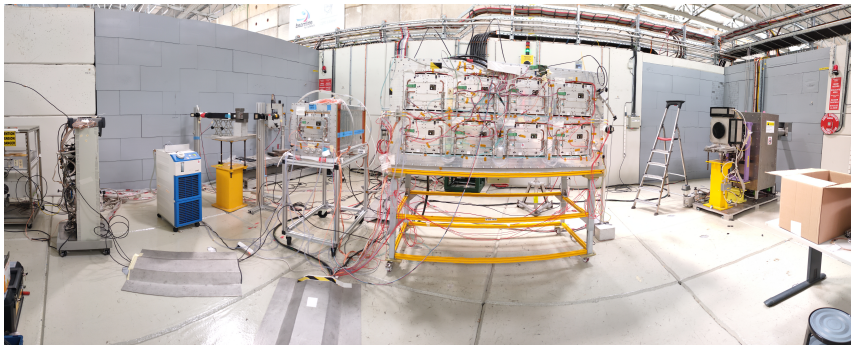

Figure 3.14: Photo of the T10 zone with all detectors aligned.

The Proton Synchrotron (PS) at CERN accelerates particles from the Proton Synchrotron Booster (PBS) reaching a maximum energy of 26 GeV before entering the SPS. Along the PS ring there are some extraction points where the primary proton beam can be diverted to the beam lines available for fixed target experiments and test beams. Along the beam lines, targets, collimators and dipole and quadrupole magnets are located, in order to produce secondary particles from primary protons and for selecting particle momenta and types. The T10 beam line provides hadrons, muons and electrons with momenta in the range between 0.1 to 15 GeV. Users are allowed to select the proper particles momenta

Figure 3.15: Photo of the CERN PS T10 line: the yellow arrow indicates the direction of the beam, the blue magnets are quadrupoles dedicated to squeeze the beam, the yellow and the green magnets are the collimators.

and the intensity of the beam by means of dedicated files present in the PC of T10 control room. The characteristics of the beam is varied from the control room adjusting magnets and collimators, and putting in and out the beam stopper and checking the completion of the operation from the dedicated computer. In general, the beam momentum is defined at $\sim 1\%$ and the maximum dimension of the beam entering the test beam hall is about 10×10 cm^2. A picture of the T10 line highlighting the beam direction is showed in Figure 3.15.
Thanks to the movable table where the Mockup was placed, all eight ERAMs could be partially scanned using beam ionization tracks. The most important results of the test beam are shown in Figure 3.16 and 3.18. The first group of plots shows the mean dE/dx in function of the particle momentum, the second shows the spatial resolution. The relevant result is measuring that the proton behaves like an electron when it has a momentum of 1 GeV, while at 1.5 GeV it behaves like a π^+ or a μ^+. Hence, test beam data are well reproducing the simulation in plot in Figure 3.17 [41].

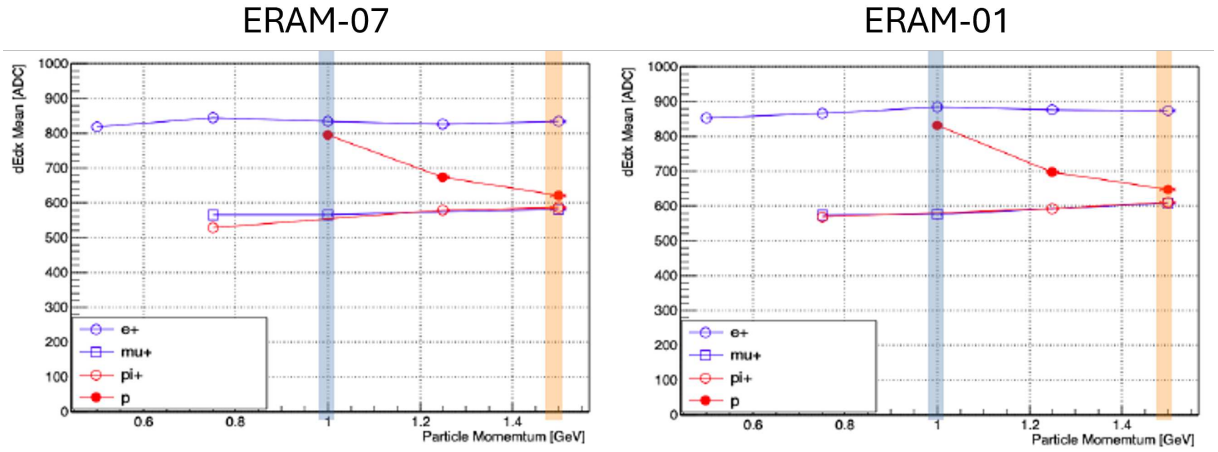

(a)

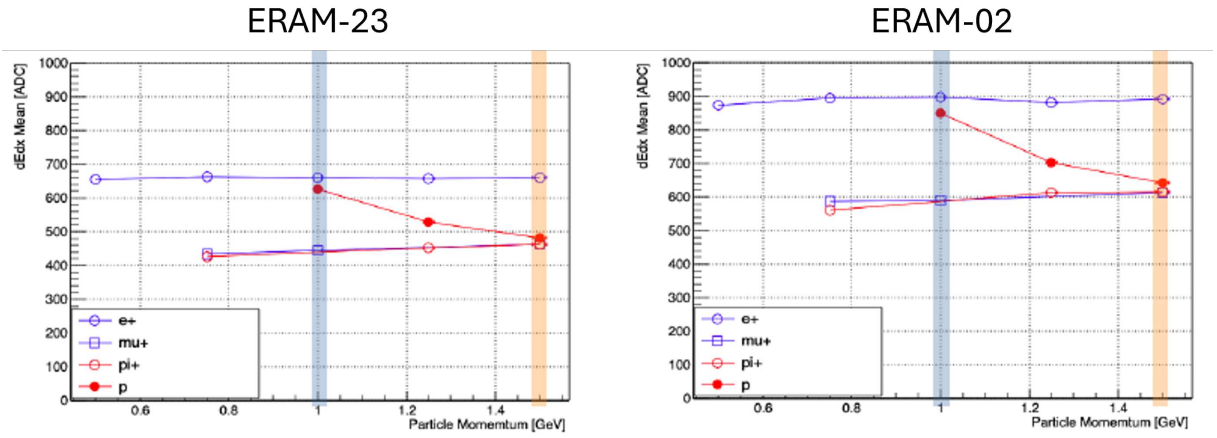

(b)

Figure 3.16: Plot of the mean dE/dx in function of the particle momentum for each ERAM. Four kind of particles are selected by different triggers: electrons, protons, muons and pions. The bars highlight the relevant particle momenta where the proton has the same dE/dx of electrons (blue bar) and of muons or pions (orange bar). Private communication at the weekly HATPC meeting.

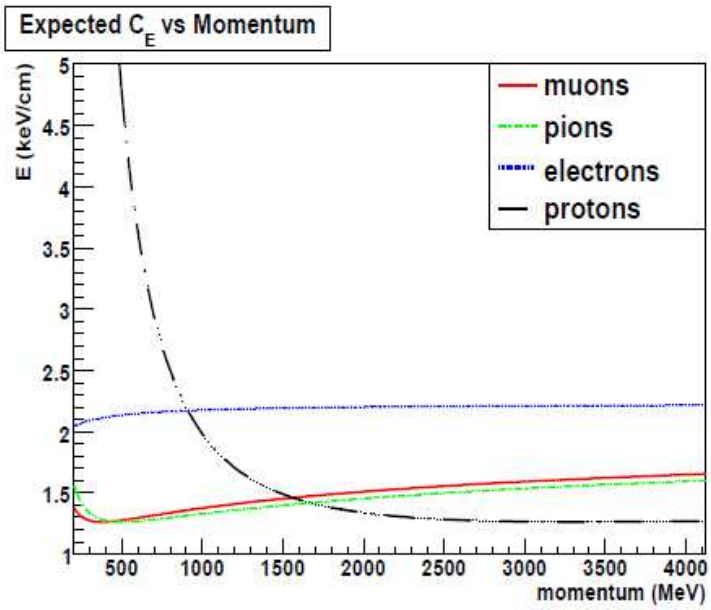

Figure 3.17: Expected dE/dx for different particles in the T2K TPC [41].

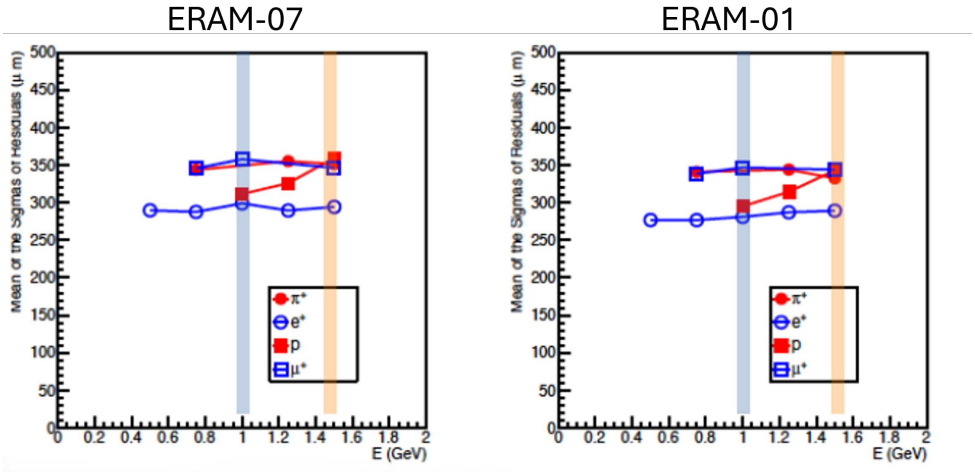

(a)

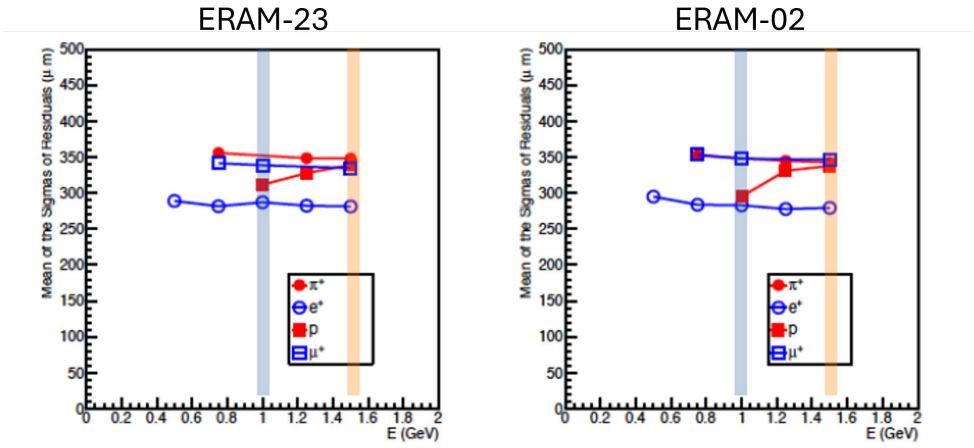

(b)

Figure 3.18: Spatial resolution computed from test beam data. Private communication at the weekly HATPC meeting.

3.3 Full HATPC assembling

I joined the CERN laboratories at the time the second half TPC was tested and validated. As part of my thesis I joined the ongoing construction activities effectively working on the HATPC.

Once completed and tested the two FCs, they were ready to be assembled together to form the full HATPC. With the support of trained experts using the crane, one of the two FCs was rotated with the cathode plane facing the ceiling. The other was lifted, rotated with the cathode side facing the floor, and positioned over the first one. A very precise alignment was necessary to fit all the 78 screws in G10 material (see Figure 3.19(a) and (b)). Screws and nuts were thoroughly cleaned with isopropanol before being used to

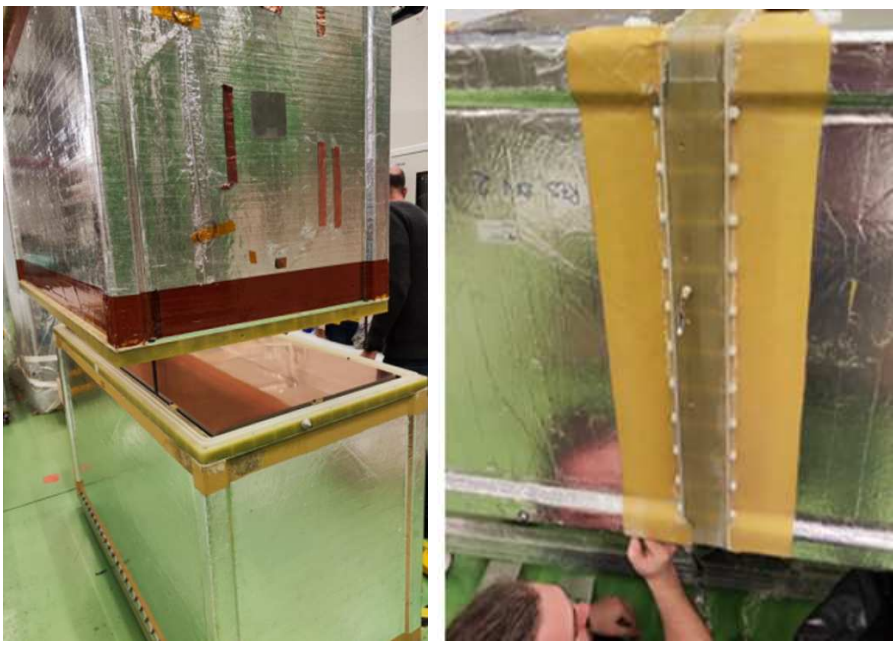

(a) (b)

Figure 3.19: In (b) the moment of the alignment of the two halves, while a focus on the screws is provided in (b).

close the two halves.
After this phase, the assembled HATPC entered the 182 clean room to be equipped with the ERAM detectors. To ensure that during the module frame equipping all ERAMS were operational and no damage occurred, a voltage of ≈ 100 V has been applied to the DLC layer: this guarantees the absence of shorts between the mesh and the resistive plane that would prevent the full HATPC commissioning and would require a second intervention in the clean room. To check that the o-ring positioning, which guarantees the gas tightness between the ERAM stiffener and the module frame, is correct a leak search via He sniffer is performed. The TPC gas outlet is closed and an overpressure on 10 mbar (≈ 30 liters) is obtained by injecting pure He gas. All the 16 regions around the ERAM stiffener are checked via a high-sensitivity sniffer to exclude major leaks: values below 10^{-6} mbar L/s are normally obtained. If we consider that the Helium was the 1% of the gas inside the TPC, no local leak at the level of 10^{-4} mbar L/s was found.

The HATPC is then moved out of the clean room and it is connected to the gas system (see Section 4.1) for long-term leakage tests.

In the meantime, the HV input connector box was fixed in the final position and the wire supplying the voltage from the connector to the cathode was soldered. My responsibility was to definitely seal all the screws employing a very strong glue Araldite 2012. Since the cathode voltage could be raised up to 30 kV, I also sprayed anticorona lacquer on the entire cathode perimeter, the HV input connector box, and the screws as an additional precaution.
The further step was the covering of the junction with insulating layers. In Figure 3.21 is shown a schematic drawing of the different materials I used and their sequence. First, I taped the edge of the TPC with Kapton, ensuring the junction was covered. I used a double-sided adhesive tape to fix a ≈ 200 μm thick and 55 cm wide layer of Mylar. Two layers of ~ 2 m and two layers of ~ 1 m were attached carefully stretching each sheet. Using the double-sided tape again, I covered the Mylar foils with aluminum sheets of the same length, but 300 μm thick and 60 cm wide. With the Aluminum tape, I fixed the sides of the Aluminum sheet to the TPC walls, leaving some space for the air to circulate in order to prevent condensation. In those sections only I covered the sharp edges of the foil.
Finally, I performed a test with the multimeter to ensure that the entire surface was connected at ground. The bottom HATPC was tested and commissioned at CERN and then shipped to the J-PARC laboratories in Japan. The installation fitted the bottom HATPC in the new ND280 upgrade basket as shown in Figure 3.22.

(a) (b)

Figure 3.20: In (a) the photo of the first covering layer in Mylar positioned over the junction is shown and, in (b), the photo of the second layer made of Aluminum.

The first part of my thesis work contributed to the construction of the bottom HATPC, providing me with the opportunity to acquire extensive technical and mechanical expertise.

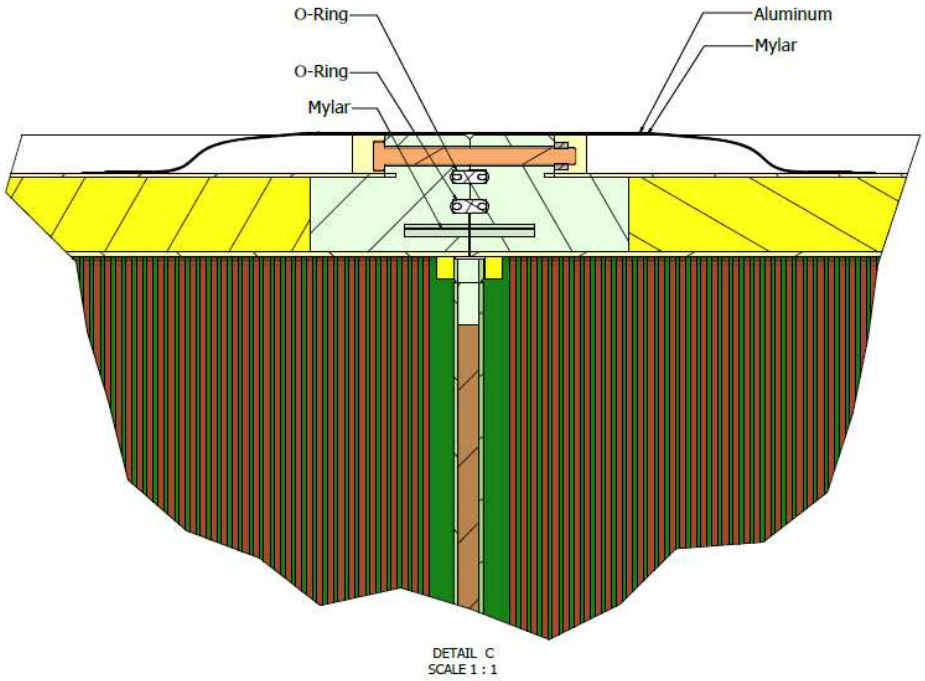

Figure 3.21: Schematic representation of the cathode junction with covering layers of Mylar and Aluminum.

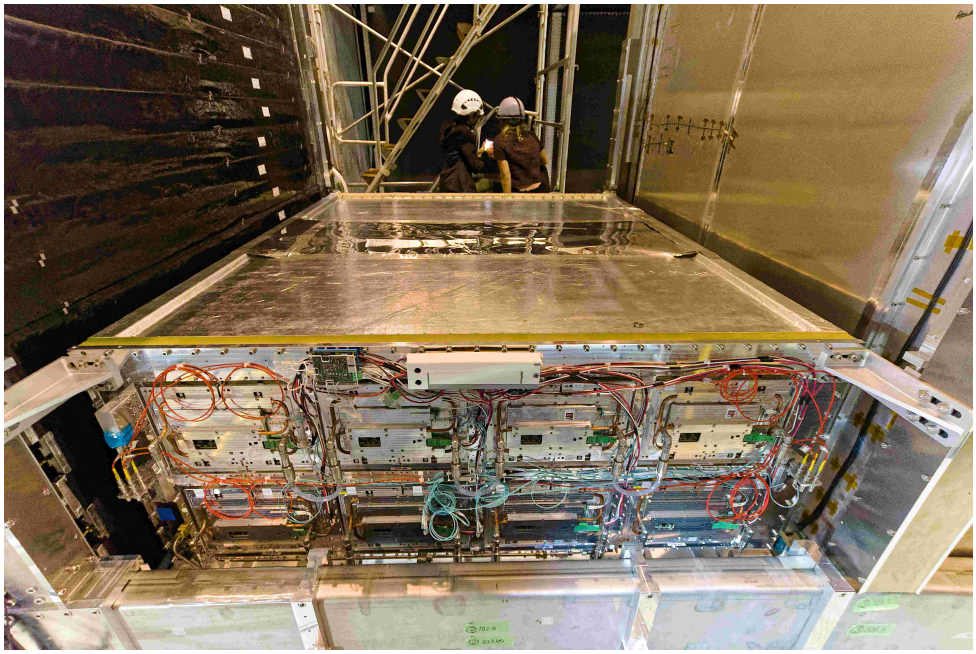

Figure 3.22: Bottom HATPC installed inside the ND280 basket surrounded by TOF panels.

Chapter 4

Drift velocity measurements from cosmic ray data

A very stable drift velocity is one of the most important requirements for a TPC. When a particle crosses the TPC volume ionizing the gas, the electrons produced in the ionization drift to the anode because of the electric field. If the x and y projected positions are measured in the ERAM plane from the position of the pads reading the signal, the z position is determined by measuring the time interval between when the particle crosses the TPC (generating electron-ion pairs) and when the electrons reach the anode. The time interval is then multiplied by the drift velocity to obtain the distance. For this reason, the stability and uniformity of the drift velocity is of utmost importance. As already mentioned, a dedicated small TPC called Gas Monitoring Chamber (GMC), read by the same ERAM detector (one unit), and with the same electric field inside the chamber, is used to continuously monitor the drift velocity and the gas quality. The GMC achieves high performances measuring the drift velocity using two radioactive sources ^{90}Sr placed at a known distance. However, the GMC is a separate detector, and the drift velocity measurements, while precise and rapidly obtainable, could contain biases. The gas flowing inside the GMC is the same gas exiting the HATPC, and it is possible that some contaminants could mix with the HATPC gas from pipes or junctions.

In this chapter, I begin by exploring the properties of the gas and their evolution from the purging phase to the optimal conditions for data taking. As a second point, I present a study on the drift velocity computed with a new method directly from the cosmic data collected by the HATPC itself. During my stay at CERN I collaborated to build the gas system and to set up the detector for the cosmic test, which was a compulsory part of the commissioning before the shipment to the ND280 site in Japan. The aim of the method is to select cosmic tracks crossing the anode or the cathode or both, and to look for the drift velocity calculation from the anode and cathode peaks in the time spectrum. The selection is done without any signal convolution with the neighbouring pads, however it permits to rapidly estimate the drift velocity from the HATPC and to study the uniformity for each ERAM.

4.1 The gas system for the HATPC commissioning at CERN

A dedicated gas distribution system was built for the commissioning of the HATPCs at CERN. Its scheme is illustrated in Figure 4.1. The Ar gas or the T2K mixture, according

to the different needs, is stored in a set of 12 bottles, 50 liters each, outside the 182 building at CERN. A main pressure reducer brings the gas to a pressure of approximately 5 bar. The gas is transferred to the main gas distribution and control panel, inside the 182 building, next to the HATPC via a 6/4 mm pipe. A system of valves allows for the line purging at each gas bank change avoiding contaminating the gas lines and the HATPC under test. The flow is adjusted via a Vögtlin manual flowmeter, able to control the flow from few liters per minute till 500 L/h. The typical flow is 200 L/h. To avoid the HATPC from being subject to pressure larger than 20 mm a high-pressure safety bubbler is connected at the TPC input. The TPC volume can be isolated via manual valves and bypassed: in this way it is possible to measure the leak rate via the dedicated pressure sensors and it is possible to sample the input gas excluding the TPC. The gas exiting the TPC volume can be directly vented via a low impedance line ending in a bubbler for fast gas purging operations or sampled via a Vaisala DMT152 [42] dew point transmitter in series with a Teledyne Oxygen InstaTrans detector. The first span a sensitivity range from 0 to -60° dew point, while the second is capable to measure the O_2 contamination at the ppm level. These devices are fundamental to monitor the gas quality evolution after the connection of the TPC. The flow through the sensors is adjusted via a Vögtlin flowmeter up to the maximum value of 20 L/h. An extra pick-up line, normally closed by a valve enables the sampling of the gas for gas chromatography studies. The system is complemented by a further gas line, parallel to the previously described one to send the gas to the Gas Monitoring Chambers. Also in this case due to the different impedance of the lines a flowmeter enables the adjustment the gas flow to the desired values of ≈ 6 L/h.

4.2 Gas contaminants and gas quality models

The T2K gas mixture inside the HATPC is Ar:CF_4:iC_4H_{10} (95:3:2). The drift velocity and gas gain of T2K TPC gas are sensitive to the stability of the gas mixture composition and to CO_2, N_2 and H_2O contamination. In addition, O_2 impurities have to be minimised to avoid electron attachment. In order to prevent contamination of the pure (T2K) gas by air from the surrounding athmosphere, an overpressure is usually applied inside the TPC vessel, so that the outstreaming gas hinders the air to flow in. And the contaminants present at the beginning of operations are removed by flushing fresh T2K gas inside the vessel. The sensor line in Section 4.1 was built for the purpose of monitoring the gas properties and composition dynamics.
The sources of contaminants may be multiple: the air initially present inside the TPC and the water adsorbed into Kapton inner surface layers are the most important. It is mandatory to measure the amount of O_2 in order to keep under control gas gain: electrons recombination with Oxygen molecules decreases gas gain and introduces biases respectively in the 3D reconstruction of tracks and in the Particle Identification. For this reason, only a very tiny contamination in the order of tens of ppm is allowed. On the other hand, moisture contamination of the gas mixture reduces the drift velocity: for instance, 1000 ppm of moisture contamination degrades drift velocity by more than 10%.

4.2.1 Models for the removal of gas contaminants

Concerning O_2, we expect this contaminant to come mainly from the air initially present in the TPC volume and negligible contribution due to adsorption from detector wall surfaces.

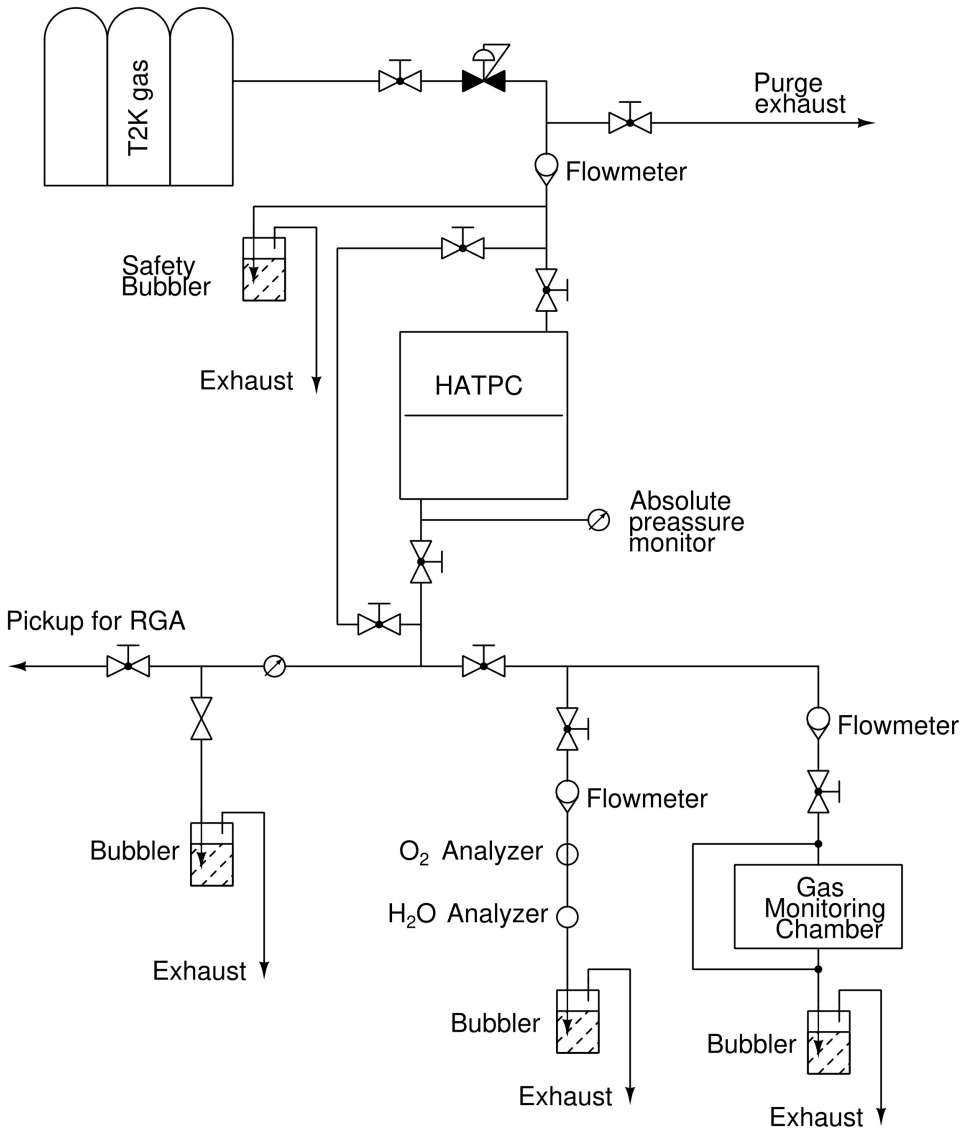

Figure 4.1: Schematic view of the gas system used at CERN for the HATPC commissioning.

The variation of Oxygen concentration as a function of time could be described by the following differential equation:

$$\frac{dc(t)}{dt} = -\frac{f}{V}c(t), \tag{4.1}$$

where f is the fresh gas stationary flux and V is the volume of the vessel. A solution for this equation is, with c_0 the initial concentration:

$$c(t) = c_0 e^{-\frac{f}{V}t} \tag{4.2}$$

The model can be adapted to flux variation considering the different fluxes $f_1, f_2, ..., f_i$ and the corresponding duration $t_1, t_2, ..., t_i$.

$$c(t) = c_0 e^{-\frac{(f_1 \cdot t_1 + f_2 \cdot t_2 + ... + f_i \cdot t_i)}{V}} \tag{4.3}$$

Given the "exchange volume" defined as $V_s = f \cdot t$, we may express the Formula 4.3 in function of V_s substituting $t = \frac{V_s}{f}$.

$$c(V_s) = c_0 e^{-\frac{(V_{s_1} + V_{s_2} + ... + V_{s_i})}{V}} \tag{4.4}$$

The initial concentration of O_2, from the air trapped inside the TPC, is 209500 ppm as for the atmosphere at sea level. In the next Section 4.2.2 I apply this model to estimate the necessary volume changes to reach the required value of 10 ppm, under which data are considered good.

Concerning the estimation of water contamination, the main sources of contamination moisture are two: the presence of moisture in the air and the desorption from the innermost layers of the walls made of 0.5 mm of Kapton. The large amount of water at the start of the gas flushing procedure is expected to decrease rapidly, following the exponential curve in Form. 4.4 as a function of the exchanged volume, as previously discussed for the case of Oxigen contamination.
This model is no more followed once the concentration of water reaches the level where the water evaporation rate becomes competitive with the purging rate. In Kapton exposed to the environment at STP atmospheric conditions, moisture is adsorbed up to saturation, reaching about 4% of Kapton mass. Then, when Kapton is exposed to a dryer environment, it may release moisture inside the vessel. Water concentration is then expected to decrease much slower due to the combination of vessel purge rate and the rate of evaporation from surfaces. The following equation might be used to describe contaminant concentration, including water desorption from walls at constant rate δ:

$$\frac{dc(t)}{dt} + \frac{f}{V}c(t) = \delta \tag{4.5}$$

whose solution yields a constant concentration level equal to $V\delta/f$ after the exponential term becomes negligible with respect to $V\delta/f$. Such steady concentration remains until moisture is completely removed from Kapton.

Concerning N_2 we expected the main contributions by the air initially present in the TPC volume as for O_2. Not being equipped with a dedicated sensor for N_2, we analyzed its content with a Residual Gas Analyzer, working as mass spectrometer. Thanks to it we could verify also the validity of the other measurements i.e. H_20 and O_2 and to study the presence of additional contamination molecules. The analysis was quite complicated by the overlap at the same atomic mass of different molecules or atoms with the same A/Z ratio. A detailed analysis is still in progress.

4.2.2 Gas analysis plots

In this section the analysis of the most important quantities concerning the gas are presented. Data are collected with the available sensors in the gas analysis line of the gas system or with the HATPC monitoring system. During the commissioning phase, some sensors were added at different time. The first part of analysis is dedicated to gas quality, before starting cosmics data taking, while flushing Argon, to evaluate if the models for oxygen and water concentration in the gas, presented in Section 4.2, can describe data. The second part is a collection of plots from both the analysis sensor line and the monitoring system, showing the gas properties in working conditions, during the data taking. During the data taking the gas flushed inside the HATPC is the T2K mixture.

Oxigen concentration plots

The following study aims to test the model for oxygen contamination presented in the previous section. The goal is to determine the quantity of gas (number of exchanged volumes) needed to reduce the concentration below the required threshold of 100 ppm for

the TPC to operate properly, and below 10 ppm to collect good data.

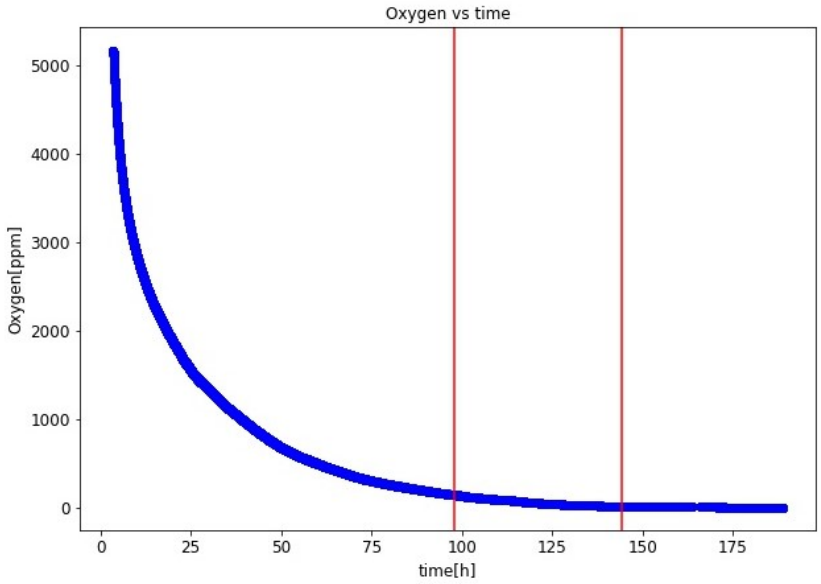

Figure 4.2: Oxigen concentration as a function of time (hours) measured by the dedicated sensor. The total hours taken into account are those spent flushing Argon in the TPC.

This plot shows the O_2 concentration in the gas, measured by the Oxigen analyzer in the analysis line of the gas system (Figure 4.1), in function of time. The two red lines delimits the subset of data I studied in detail to test the model. In the following plots I computed the O_2 concentration in function of the exchanged volume, keeping the total volume of the gas in the TPC constant. The plot in Figure 4.3(a) shows the O_2 concentration in

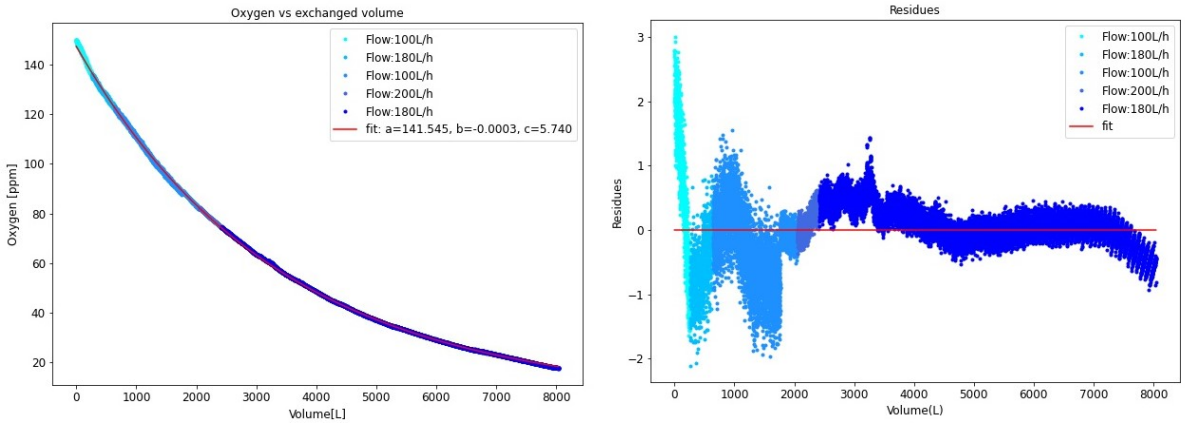

(a) (b)

Figure 4.3: Fit of the oxigen concentration as function of exchanged volume in (a), and the plot of the residuals in (b). The considered range is the one between the red lines in Figure 4.2.

function of the exchanged volume. The latter quantity is calculated taking into account the flux variation, changed five times in the time interval I considered, and by applying a correction for Argon gas measurement using the available flow-meter. The interest on this plot relies in the possibility of computing the necessary volume changes to reduce the O_2 concentration below 100 ppm. Data are fitted with a generic exponential function

Flux f[L/h]	Time Δt[h]
100	2.18
180	1.84
100	11.98
200	1.57
180	26.59
Full time interval:	44.16 h

Table 4.1: Parameter values of the fit performed in the plot shown in Figure 4.3(a).

following the already mentioned model:

$$y = ae^{bx} + c \tag{4.6}$$

and the fit results are presented in Table 4.2. The effect of assuming constant the volume

Parameter	Fit results
a	141.55 ± 0.02 [ppm]
b	$(-3.523 \pm 0.001) \cdot 10^{-4}$ [1/L]
c	5.74 ± 0.02 [ppm]

Table 4.2: Parameter values of the fit performed in the plot shown in Figure 4.3(a).

of the gas inside the TPC is clearly visible plotting the residuals as in Figure 4.3(b). The oscillations are due to pressure and temperature variation directly affecting the volume. A correction for $\frac{P}{T}$ is needed. The available data, collected at the beginning of the commissioning, do not permit the correction on the volume variation. Other sensors were added in the following days, when the gas was switch to the T2K mixture, measuring the missing quantities (internal temperature).

From the fit parameters, imposing the initial concentration of O_2 equal to 209500 ppm (20.9%) from air, I computed that a level lower than 10 *ppm* should be reached after changing 10 volumes of gas. This conclusion is in fair agreement with the measurement performed with the electrolytic cell based sensor. Five volume changes were done with Argon and at least 5 with T2K gas.

Water concentration plots

The other quantity to analyse is the water content. The requirement to safely switch on the ERAM detectors is to have a relative humidity less than 4%, corresponding to a concentration of 630 ppm and a dew-point ~ -20°C at 25°C gas temperature. A Vaisala dew-point temperature sensor was installed in the analysis line of the gas system. The data collected during the purging phase by the dew-point sensor are visible in the plot in Figure 4.4.
I converted the data from dew-point values to ppm values using the information on the internal pressure provided by the Vaisala sensor. I started from the calculation of $e_w(T)$, which is the saturation vapor pressure in pascals. For temperatures ranging from -45°C to +60°C, the Magnus equation given below can estimate the vapor pressure over water with 95% confidence:

$$ln(e_w(T)) = ln(611.2) + \frac{17.62T}{243.12 + T}. \tag{4.7}$$

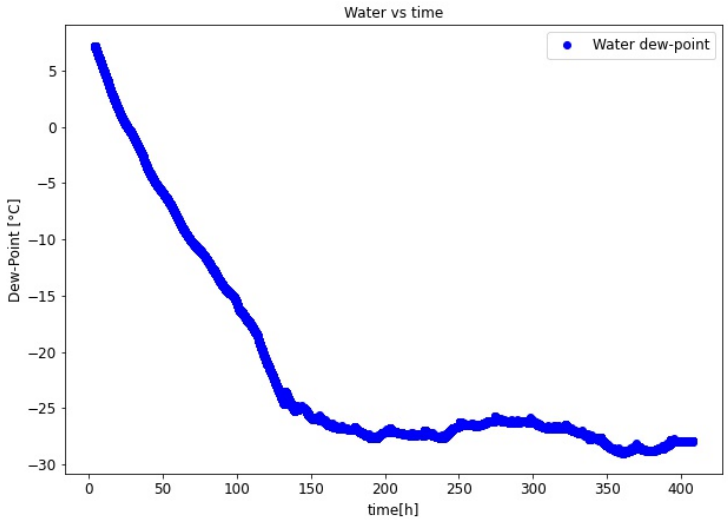

Figure 4.4: Plot of dew-point temperature (°C) measured by the Vaisala sensor in function of the cumulative time (h).

The water concentration in ppm is found using the following formula:

$$ppm = \frac{Partial\ Pressure}{Total\ Pressure} \times 1000000 = \frac{e_w(T)}{P} \times 1000000. \tag{4.8}$$

The plot in Figure 4.5 shows the dew-point measurements as function of the time converted in ppm as function of exchanged volume. As already mentioned in Section 4.2, the

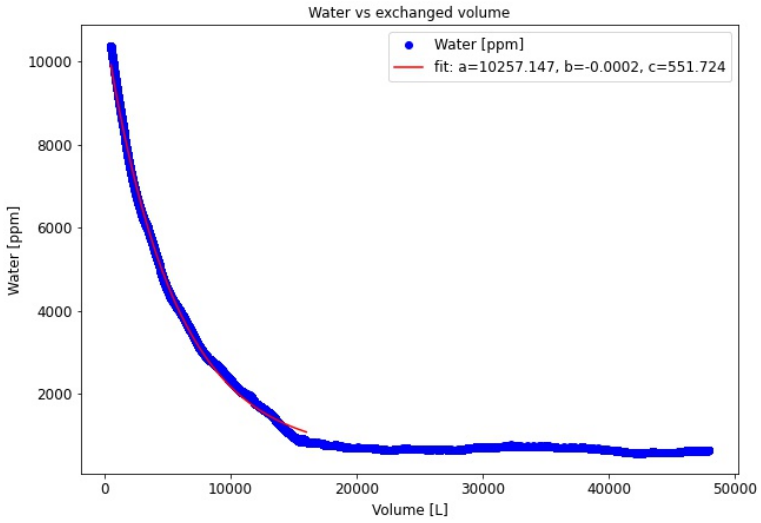

Figure 4.5: Plot of water concentration [ppm] in function of the exchanged gas volume [L]. An exponential fit is performed to the initial part of the plot.

rapidly descending of water concentration is expected to follow the exponential trend in Form. 4.4. Hence, a generic fit (Form. 4.6) is performed in that range and the results are shown in Table 4.3.

The results from the fits point to a moisture purging rate about half that of Oxigen,

Parameter	Fit results
a	10257 ± 2 [ppm]
b	$(-1.846 \pm 0.001) \cdot 10^{-4}$ [1/L]
c	552 ± 2 [ppm]

Table 4.3: Parameter values of the fit performed in the plot shown in Figure 4.4(a).

which might be due to a lower drag coefficient for T2K gas to purge water molecules than Oxigen molecules. As a consequence in order to reach a fixed contamination level, for water it would take double number of exchanged volumes compared to Oxigen, that means double time at fixed rate.
On the other hand, for water, also desorption had to be accounted for. My measurements (see Figure 4.5) indicate that after about 15000 L (i.e. about 3 TPC volumes) of fresh gas fluxed into the vessel, water concentration reaches a steady level of about 500 ppm due to the desorption dominance, as described by equation 4.5. Given the large amount of water uptake by Kapton (2% in mass, with respect to dry Kapton, according to ref. [43]) we expected that the corresponding amount of water (about 50 cc) would be purged within a couple of months.

In conclusion, due to the time constraints related to the experiment installation at J-PARC, we had to conduct the TPC commissioning with Cosmic Rays at CERN with very good conditions concerning O_2 contamination (below 10 ppm) and with reasonable conditions for Water contamination (500 ppm).

T2K gas plots during cosmics data taking

After the purging phase the gas was switched from Ar to T2K gas. Five volume changes were performed to ensure >90% of T2K gas mixture inside the HATPC. Once the water contaminants were controlled, the ERAM detectors were switched on and data taking started. The presence of O_2, shown in Figure 4.6 (a), is very stable around 1 - 1.5 ppm and the spread is due to the reached sensibility value of the sensor. The water content is described by data from a relative humidity sensor installed inside the HATPC. The required relative humidity should be less than 4%, and the plot in Figure 4.6 (b), despite being influenced by pressure and temperature fluctuations, consistently shows values well below 3%.
The last plot, in Figure 4.7, shows the $\Delta p/\Delta T$ measurement as function of time. In the plot there are some fluctuations which are depending on the day-night cycle.

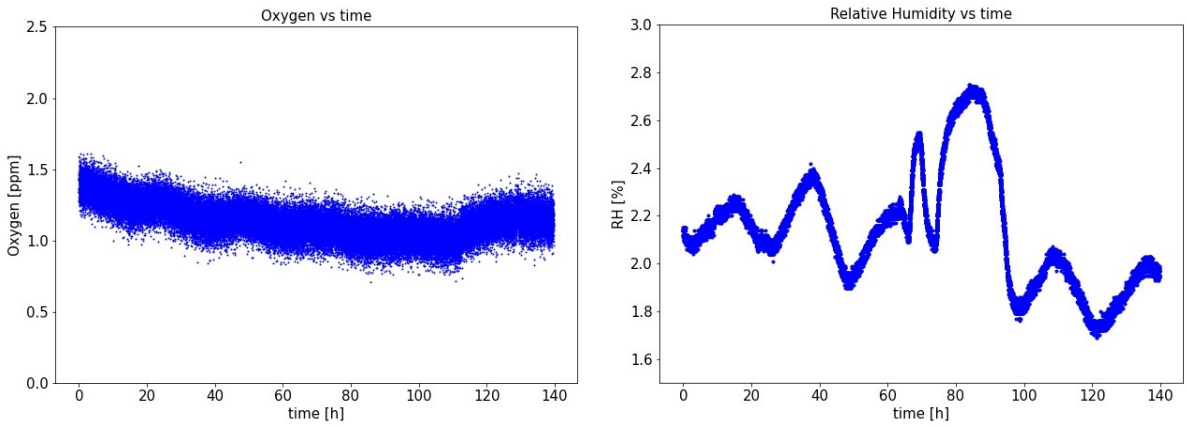

(a) (b)

Figure 4.6: The plot (a) shows the O_2 concentration in function of the time and the plot (b) shows the relative humidity stably under the required 4%.

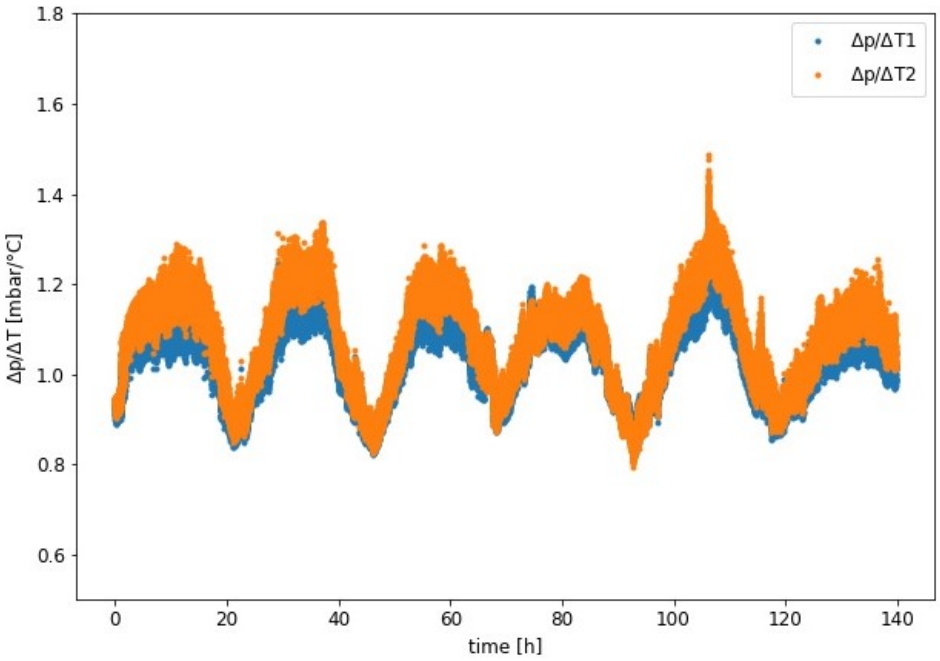

Figure 4.7: Plot of $\Delta p/\Delta T$ for both the Field Cages.

4.3 The setup for cosmic data test

The main goal of the commissioning of the bottom HATPC at CERN was to qualify the detector's performance to confirm that it met the project-level requirements. After the purging phase, once the quality of the gas was good enough to safely switch on the ERAMs, an intensive campaign of cosmic data collection was performed. The trigger was built using the available scintillators and many configurations were adopted to cover all the volume of the HATPC. In particular there were two types of scintillators at our disposal:

- Four scintillator bars, each one covering an area of 20×100 cm^2 and read by one PMT;
- Four scintillator squares, each one covering an area of 100 cm^2 and read by two PMTs. One of the squares is made by two layers of pyramidal prism scintillators

disposed as shown in Figure 4.8. The signals from the two layers are guided to the respective PMT by WLS fibers.

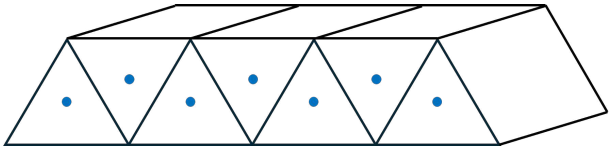

Figure 4.8: Internal shape of a layer inside the squared scintillators used to provide the trigger for cosmic rays. The blue dots are the WLS positions.

Dedicated mechanical structures were built using Bosch profiles that allowed to slide the scintillator squares from one side of the TPC to the other. In this way, even though in different runs, all the HATPC volume was tested.

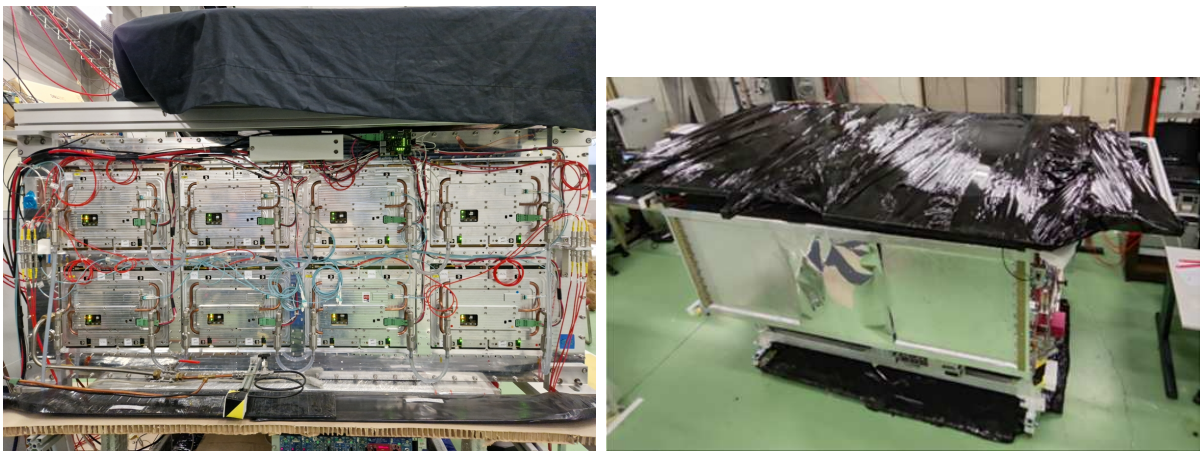

(a) (b)

Figure 4.9: Photos of the cosmic test setup. In (a), the position of two scintillator bars relative to the endplate is visible. In (b), the position of scintillator squares on the top and bottom of the HATPC is shown.

Multiple trigger configurations were made using NIM modules, setting different logic combinations of the signals from PMTs. At this point, it is necessary to mention that we found the signals from the square scintillators to be very noisy. The implications of this issue will be discussed later, as it affected the quantity of the collected data by showing differences between the two FCs and the quality introducing systematic errors. A drawing of the trigger configurations considered in the analysis performed using the algorithm I developed is provided in Figure 4.10.

RUN	**Trigger configuration**
Run 14	(S1+S2)*(S3+S4)
Run 26	(S1+S2+S3+S4)*(T_S^A+T_J^A)+B_S^{A*B}+B_J^{A*B}
Run 45	(S1+S2+S3+S4)*(T_S^A+T_J^A)+B_S^{A*B}+B_J^{A*B}

Table 4.4: Summary table of the analysed cosmic runs trigger configurations. S1,S2,S3 and S4 are the labels of the scintillator bars, while T_S,T_J,B_S,B_J, are the scintillator squares. A and B letters at the apex refer to the two PMTs reading each square.

The runs that I analysed are summarised in Table 4.4, where the correspondent trigger

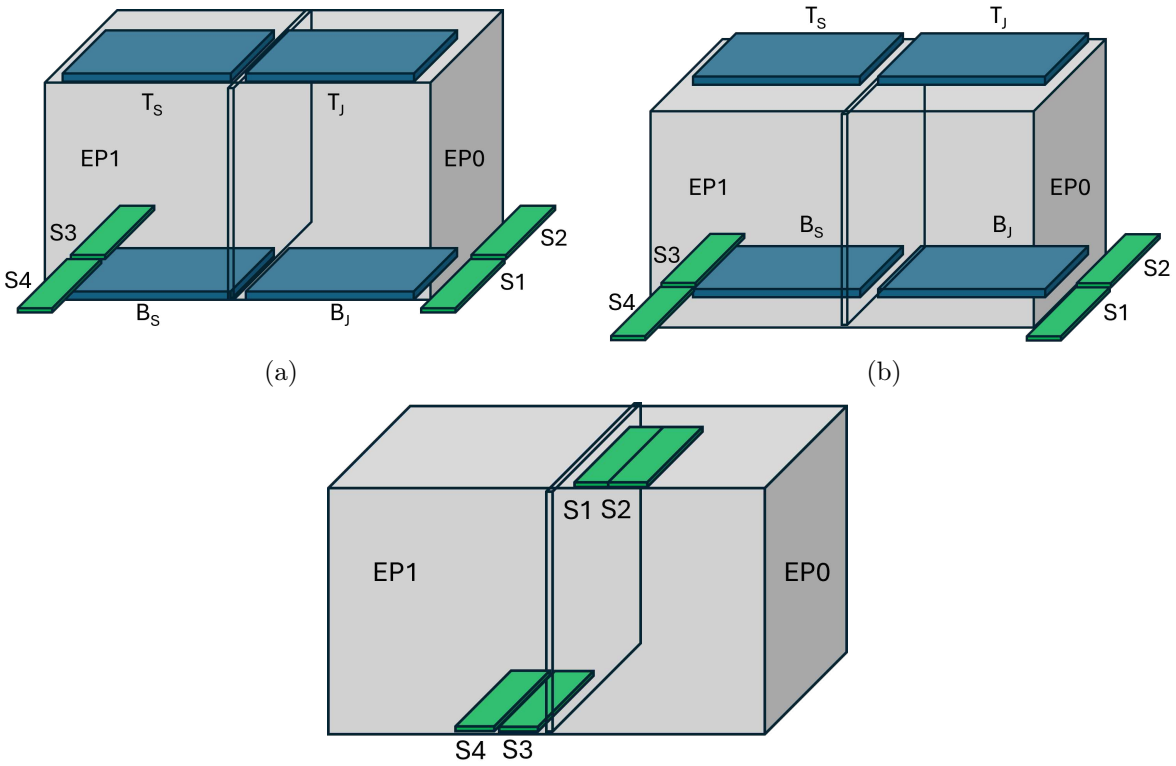

Figure 4.10: Schematic drawing of the trigger setups. The (a) disposition of scintillators is used for Run 26, the one in (b), moving the squared scintillator on the other side of the volume is used in Run 45, while the setup described in (c) provides the trigger of Run 14.

configuration for each run is indicated. Run 14 was chosen to test the analysis algorithm, as the trigger configuration was specifically designed for tracks crossing the cathode. Run 26 and Run 45 were selected for drift velocity measurements because their trigger setups could provide a subset of tracks crossing either the anode or the cathode among those collected.

4.4 The analysis of cosmic data

The code is divided in three main parts. The first one is dedicated to the track selection and to identify the last hit leading pad before the particle crosses the anode or the cathode. The second part is devoted to evaluate the properties of selected events, like how they are distributed in the xy plane, the goodness of the fit, the waveform amplitudes distribution, etc. In the third part, the drift velocity is computed from a fit of the anode and cathode peaks of the time spectrum. The latter part of the study, the results and the physical interpretation are discussed in Section (4.5).

4.4.1 Selection algorithm to identify tracks crossing anode or cathode

HATPC data collected by the DAQ are saved in Midas format and compressed. A converter program organizes the information from the Midas file in a TTree object in a new

CERN ROOT file. Another program implementing the mapping of the ERAMs, the monitoring program, permits to reconstruct and display events in the xy plane. These two tools were the starting point of my code, which aims to select the tracks crossing the cathode or the anode (or both).
Initially, the code takes one event of the run and organizes the hit pads following the original mapping of the detector. The code first processes the results in Endplate 0 (EP0) and after in Endplate 1 (EP1). A this stage, the selection is made via a sequence of filters where a new mapping is used. The mapping of the ERAMs is done looking from the point of view of EP0. The ERAM on the bottom left is labeled as "Module 0" and the numbers from 0 to 7 increase from left to right and from bottom to top. The pad numbers in the ERAMs increase in the same direction and cover the entire endplate. The pads in the x axis are ordered from 0 to 143, while those in the y axis are ordered from 0 to 63. A schematic drawing of the mapping is provided in Figure 4.11.

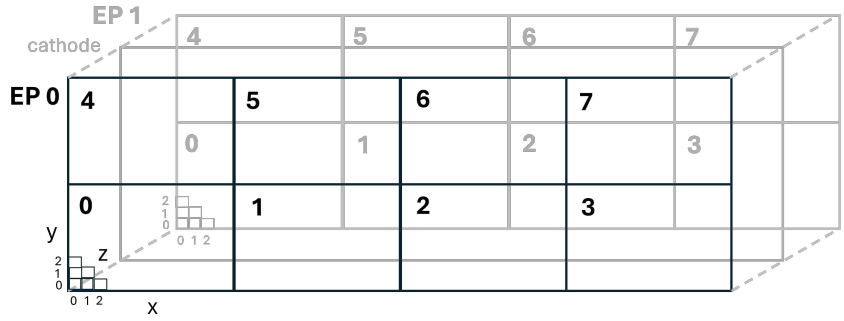

Figure 4.11: New mapping of ERAMs and pads used in this study. The x and y axes increase the number of pads from left to right and from bottom to top, respectively, while the time bins in the z direction increase the number from each endplate to the cathode.

A cut on the events in a selected EP is done looking at the number of hit pads to be greater than 45 but less than 100. In this way, double tracks or showers of cosmic rays, are excluded from the interesting events. If the event passes the first filter, the pads are arranged in ascending order in the y direction. If more than one hit has the same pad number in the y direction, the leading pad is selected by looking at the maximum waveform amplitude. The choice of identifying the leading pad among the pads with the same y number is based on the hypothesis that most of the cosmic muons cross the detector from the top. I refer to the selected pads as "fit pads" and, if the size of the subset is greater than 10, a linear fit of the "fit pads" is performed in the xy projection. In Figure 4.12, an example of a good track is shown before and after the selection of "fit pads", with the fit superimposed. Fit results are presented in Table 4.5.

Fit results y=a+bx	
a	412 ± 42
b	-4.5 ± 0.5
χ^2	5.853
ndf	16
χ^2/ndf	0.366

Table 4.5: Fit results for a selected track passing the χ^2/ndf<2 filter.

Once performed the fit, the last pad in the direction of the fit, among the previously

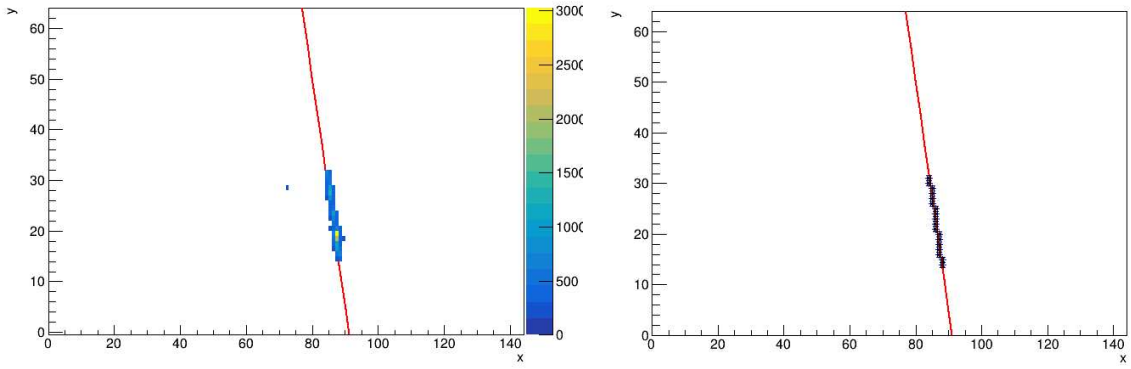

(a) (b)

Figure 4.12: The 2D histogram on the left side (a) shows a selected track projected in the xy plane where in each pads is accumulated the charge. On the right side (b), the pads selected for the fit are shown with error bars. In both cases, the fit is drawn in red.

selected "fit pads" is identified. At this point, another requirement is introduced: the "last fit pad" must be within the reduced ERAM area, which is defined by a distance of three pads from the borders in all directions. The total number of pads is 9216 and the selection removes 2976 pads. If the "last fit pad" is outside the reduced area, the track is not considered. Then the code searches the "next fit pad" by estimating its position from the fit. If the hit is missing, the track to which the fit belongs is selected. This requirement ensures that the "next fit pad" is not on the edge of an ERAM, guaranteeing that the track stops inside. Figure 4.13 shows the xy projection of a good track. The positions of the "fit pads" indicate that the track stops inside the ERAM.

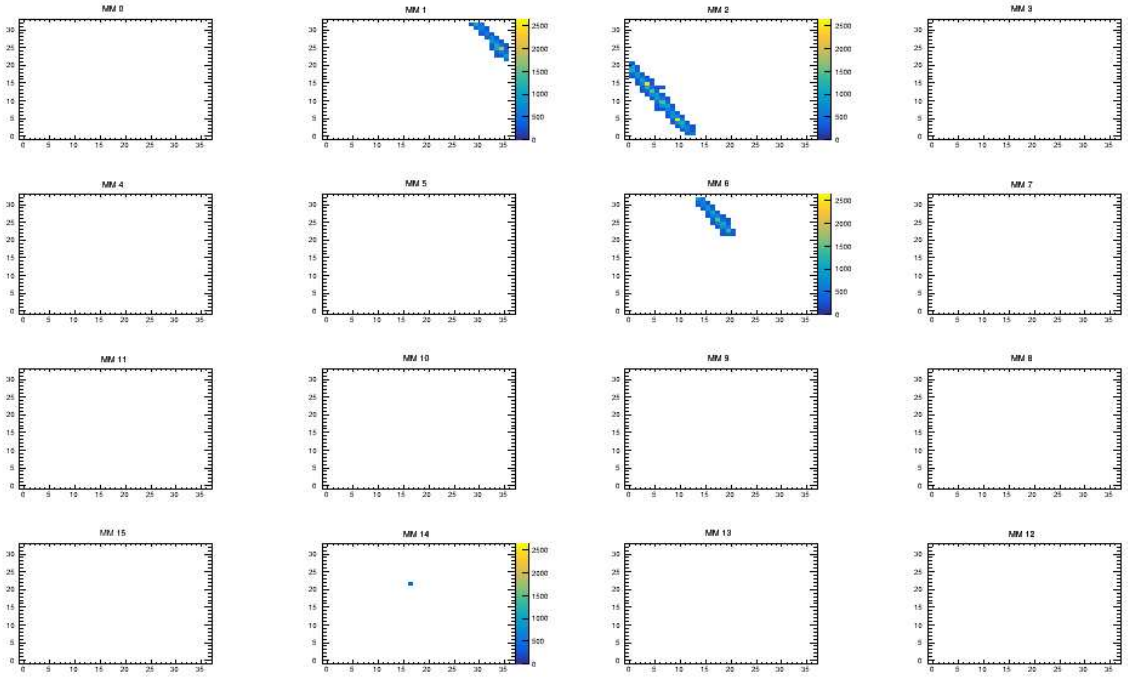

Figure 4.13: Example of track crossing the anode in EP0, with pad colors proportional to the cumulative charge collected. The number of the ERAM in this plot is the usual one used by the DAQ (labeled from 0 to 15).

The useful quantities to evaluate the goodness of the selection and to calculate the drift velocities are saved in a CERN ROOT TTree. The list is the following:

- Event number;
- Endplate ID;
- x position of the last pad of the fit (pad number on the ERAM in the x axis);
- y position of the last pad of the fit (pad number on the ERAM in the y axis);
- Time of the last pad of the fit in time bins (z axis);
- Number of hits selected for the fit;
- χ_2 of the linear fit;
- Number of degrees of freedom;
- Waveform amplitude.

The original datasets in Midas format are initially transferred to the IN2P3 CNRS scientific computing and data processing center in Lyon, where they are converted to CERN ROOT files. Subsequently, the analysis code is run over the interesting datasets, exploiting the computing power of the available machines. The analysis of the three considered runs provides the following occupancy plots, for both the EP0 and EP1, of the last hit pad for each track. These plots show the cumulative distributions of the points where the tracks cross the anode or the cathode (Figures 4.14, 4.15, 4.16). First of all, a good homogeneity of the crossing tracks can be noticed, which are spread in the triggered area without undesired recurring patterns. The major part of the selected events crosses one of the two planes around the center of it, correctly on the trigger side, as expected. The three runs have different triggers and scintillator positions as summarized in Table 4.4 and sketched in Figure 4.10.

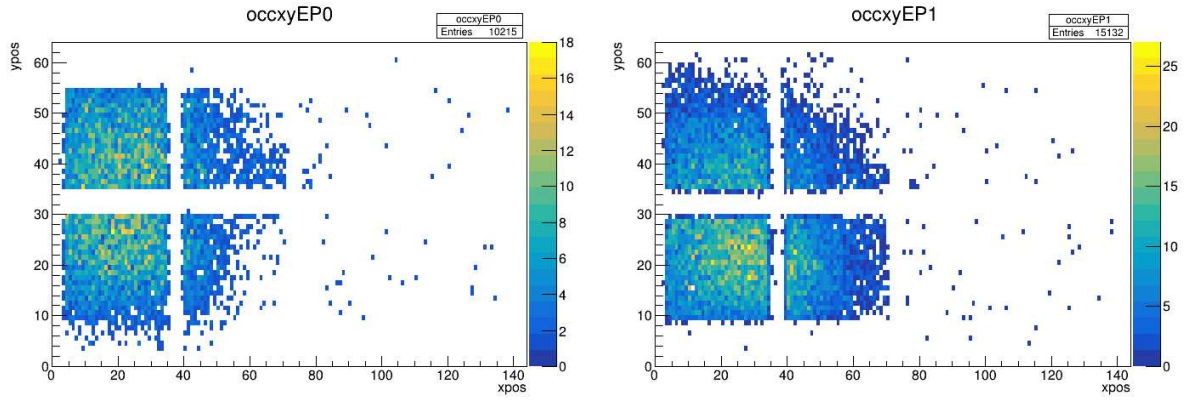

(a) (b)

Figure 4.14: Occupancy plots of Run 14 dataset divided in EP0 and EP1. The trigger scintillators are positioned in the configuration in Figure 4.10 (c). In (a), most of the tracks cross the cathode in the upper left region, while in (b), they cross in the lower left part, as expected from the trigger setup.

In Figure 4.17 (a,b,c and d) the projections of the plots in the x and y axis are provided to better explore the distribution of events. The set of tracks included in the occupancy

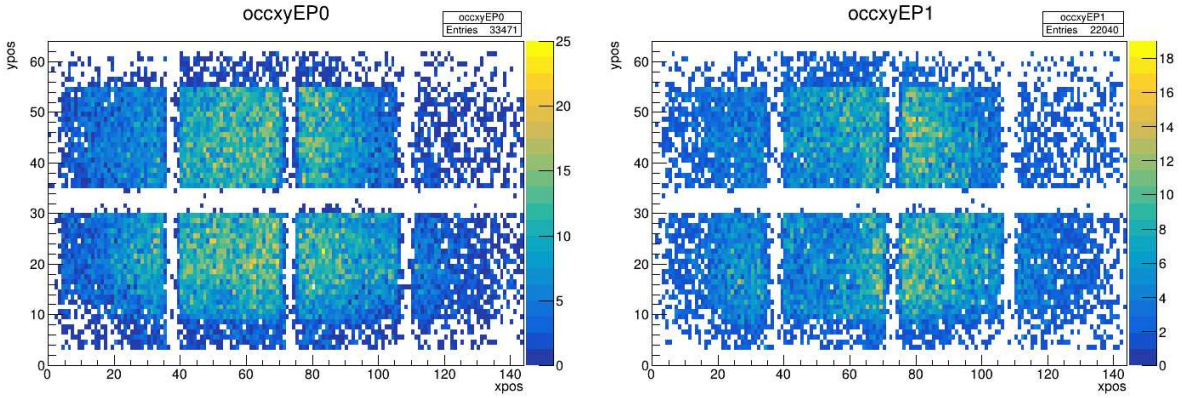

(a) (b)

Figure 4.15: Occupancy plots of Run 26 dataset divided in EP0 and EP1. The trigger scintillators are positioned in the configuration in Figure 4.10 (a). In (a), most of the tracks cross the cathode or the anode on the left side, and similarly in (b), as expected from the trigger setup.

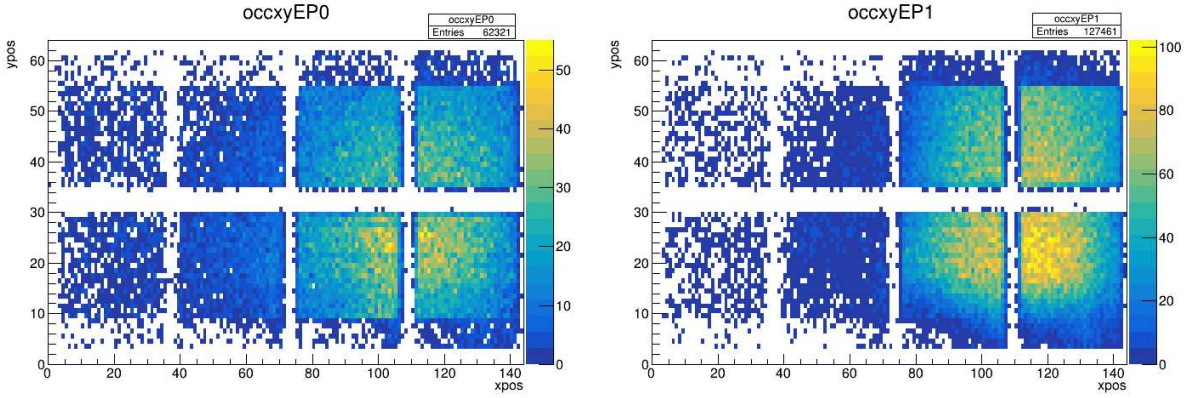

(a) (b)

Figure 4.16: The plots (a) and (b) show the occupancy plots of Run 45 in EP0 and in EP1 respectively. The trigger scintillators are positioned in the configuration in Figure 4.10(b). In (a), most of the tracks cross the cathode or the anode on the right side, and similarly in (b), as expected from the trigger setup. Pads are clustered in rectangles due to the selection requirements, which remove hits in those pads.

plots are the ones where $\chi_2/\text{ndf} < 2$ (the two parameters are taken from the linear fit). This requirement allows for the identification of good tracks where the fit converges and provides a compromise that ensures sufficient statistics in all three runs chosen for the study. The occupancy plots and their projections on the axis evidence the excluded pads of the ERAMs showing empty bands dividing the data in clusters. Without the selection, the xy plot is usually completely filled.

In-depth study of Run 14

The first run I analysed was Run 14, where the trigger was specifically dedicated to track only particles crossing the cathode plane and for this reason it was perfect to test the selection. From this dataset I could study the cathode position in the time spectrum, understand the shape of the events distribution, the goodness of the trigger efficiency for the two EPs and the effects of chosen selections. Starting from the time spectrum, the peak

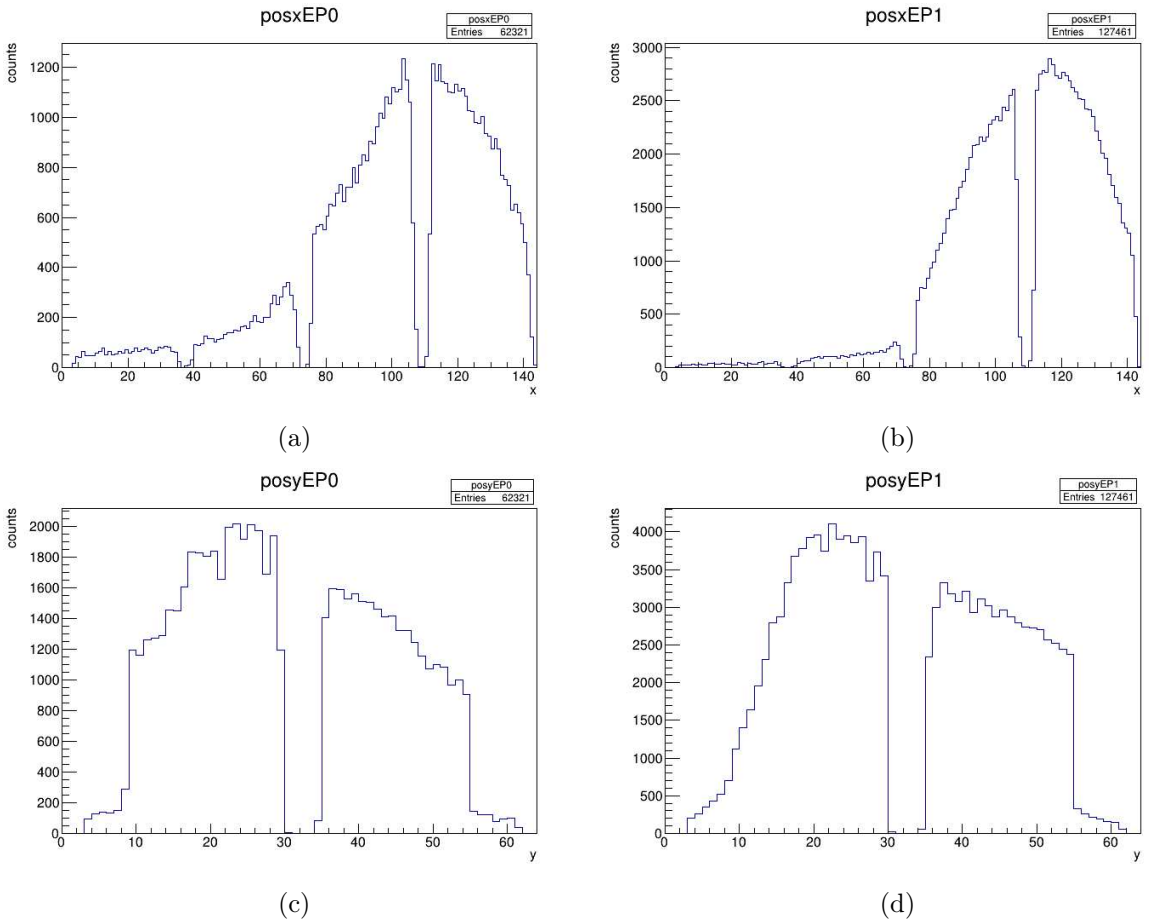

Figure 4.17: In (a) and (b), the histograms display the x projection of the occupancy plots in Figure 4.16, while in (c) and (d), the y projection is shown.

appears very narrow with a tail at higher values. A fit of the distribution with a Gaussian function is made allowing the extraction of the position of the centroid, corresponding to the time measured for the leading pad. The tail is instead the contribution of the neighbouring pads. Looking at Figures 4.18 (c) and (d), showing the cumulative plot of waveform maximum amplitudes as a function of time, it is evident that most of the events with high waveform amplitude values are concentrated in the same interval of the time spectrum peak.
The occupancy plots already presented in Figure 4.14 visualize the area where the filtered tracks cross the cathode. The number of good events is shown in Table 4.6. Both endplates detected a very similar quantity of good events, indicating that my pre-processing code works symmetrically and that the trigger setup for this run was equally efficient on both halves of the HATPC. The number of events in the selection drops when a filter is applied

Total events	**EP0**	**EP1**	**EP0 (χ^2/ndf<2)**	**EP1 (χ^2/ndf<2)**
47108	23496	23612	10215	15132

Table 4.6: This table shows the number of events in each selection of Run 14 using the trigger configuration in Figure 4.10(c).

asking for χ^2/ndf<2. The effect on the time spectrum can be seen in Figure 4.19 (a) and (b), where the red histograms, which are the same as those in Figure 4.18, are superimposed to the unfiltered ones. The main difference is the removal of events arriving

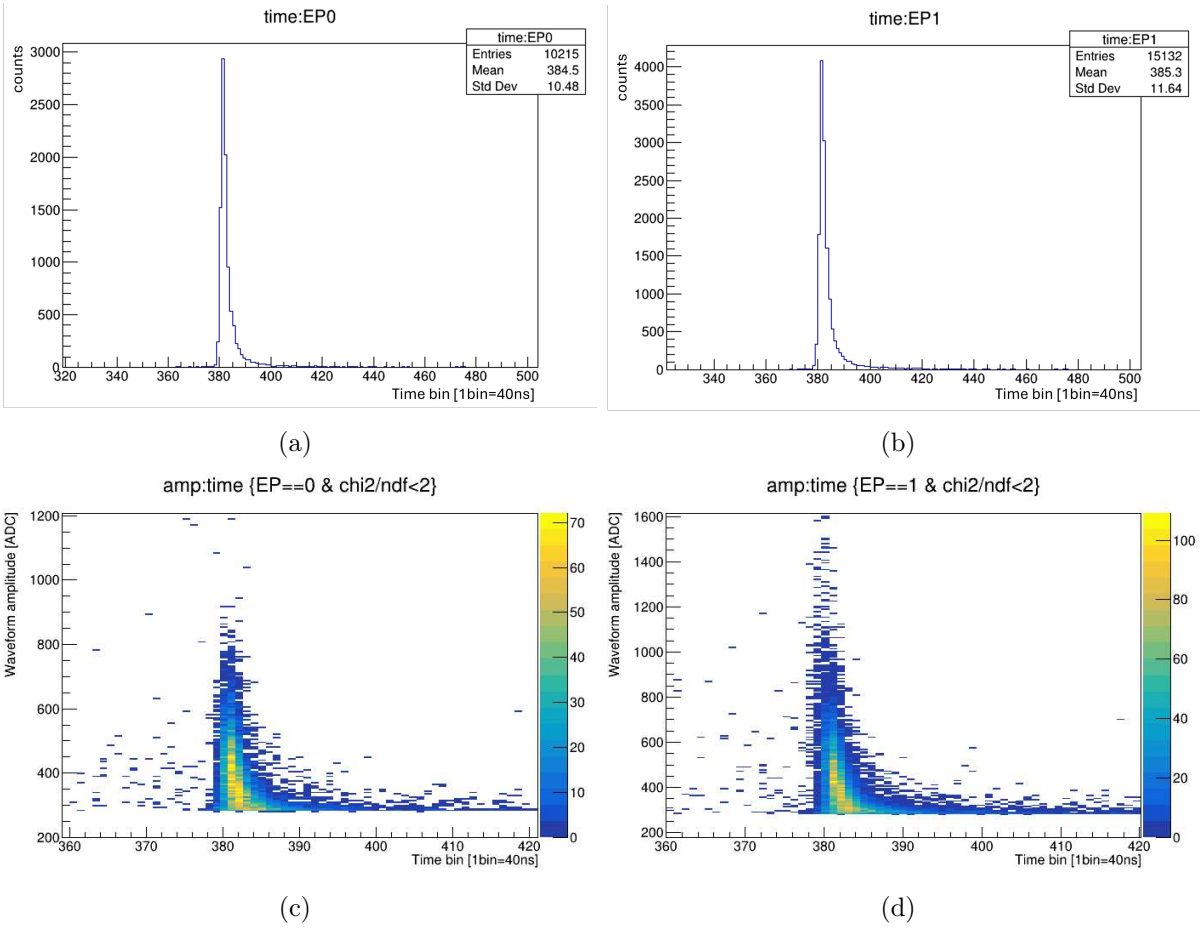

Figure 4.18: The plot in (a) and (b) shows the time spectrum for EP0 and EP1 of Run 14. Only a peak is visible because the trigger setup is set to see only tracks crossing the cathode. The 2D histograms of waveform amplitudes for the two endplates are plotted in (c) and (d). The peaks are primarily made up of leading pad waveforms, while the tails are composed of neighboring pads.

earlier than the centroids. The cut on the reduced χ^2 rejects tracks that initially pass

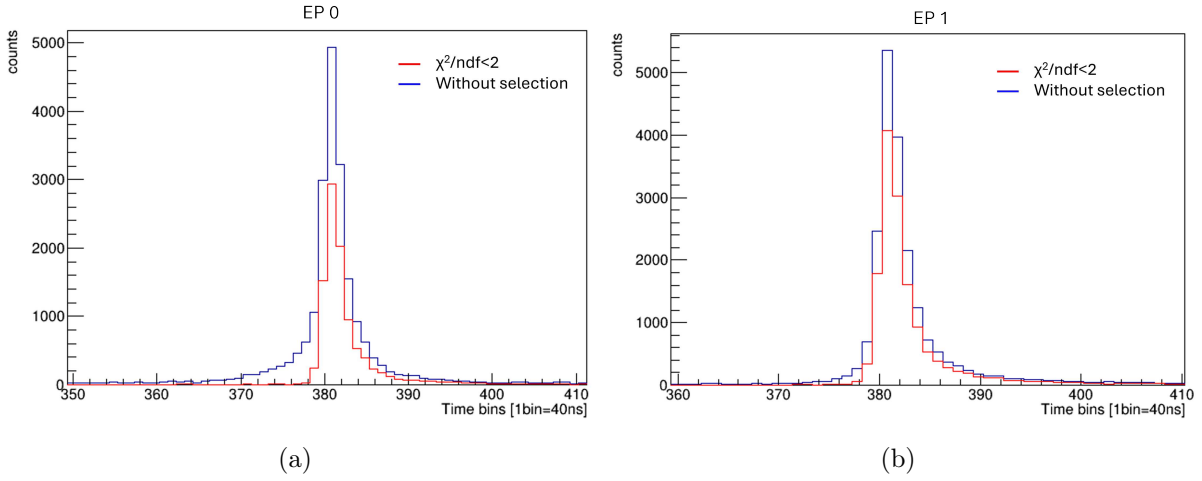

Figure 4.19: The two plots show the time distribution histograms for the two endplates of Run 14. The blue histograms represent the data without the filter on the quality of the fit (χ^2/ndf<2), while the red histograms show the two peaks after the cut.

the first selection but have poor χ^2 values in the xy plane projection fit, even if the fit converges. Figure 4.20 and Table 4.7 show fit results for a rejected track crossing the FC. At the lower side of the projection, it appears there are either two overlapping tracks. Most of these tracks are removed requiring $\chi^2/\text{ndf}<2$.

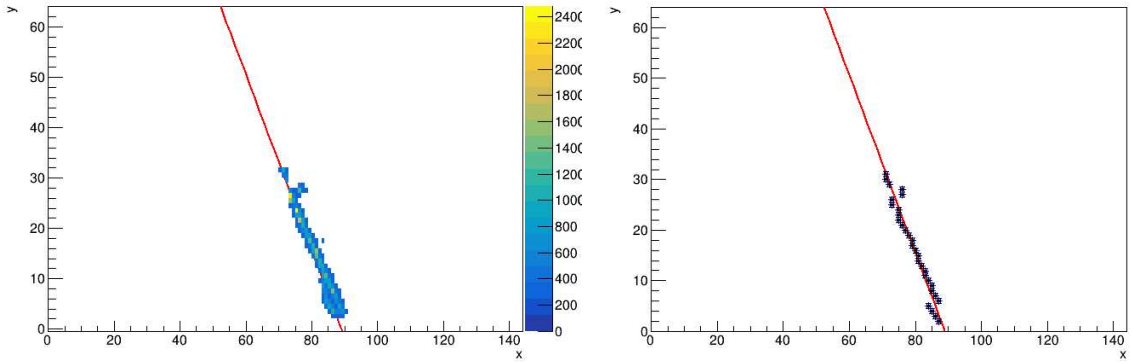

(a) (b)

Figure 4.20: Example of track discarded from the collection of very good tracks because the χ^2 is very high.

Fit results y=a+bx	
a	156 ± 3
b	-1.75 ± 0.04
χ^2	123.045
ndf	28
χ^2/ndf	4.394

Table 4.7: Fit results for a track that did not pass the $\chi^2/\text{ndf}<2$ filter.

The set of traces that survive the cuts are those that cross the anode or the cathode or horizontally cross the entire TPC. The analysis of Run 14 allowed to verify that the selection process works properly. The other plots provided insights into various features of the algorithm's behavior and performance. Feeling confident in the positive results obtained from the Run 14 analysis, I applied the code to the other two datasets (Run 26 and Run 45) to perform drift velocity measurements.

4.5 Drift velocity measurements

The study I conducted aims to map the drift velocity for all the ERAMs on both endplates. I chose to analyze Run 26 and Run 45 from the cosmic test data due to their high statistics and complementary trigger configurations. The two datasets were collected approximately five days apart, so the gas composition is expected to be cleaner in Run 45. A discussion on this topic will follow the presentation of the results.

The time spectrum of filtered events should count two peaks: the first one is the position of the anode and the second one is the cathode. However, if I plot the time spectrum for Run 26 and for Run 45, in Figure 4.21 and 4.22 respectively, I see more than one peak

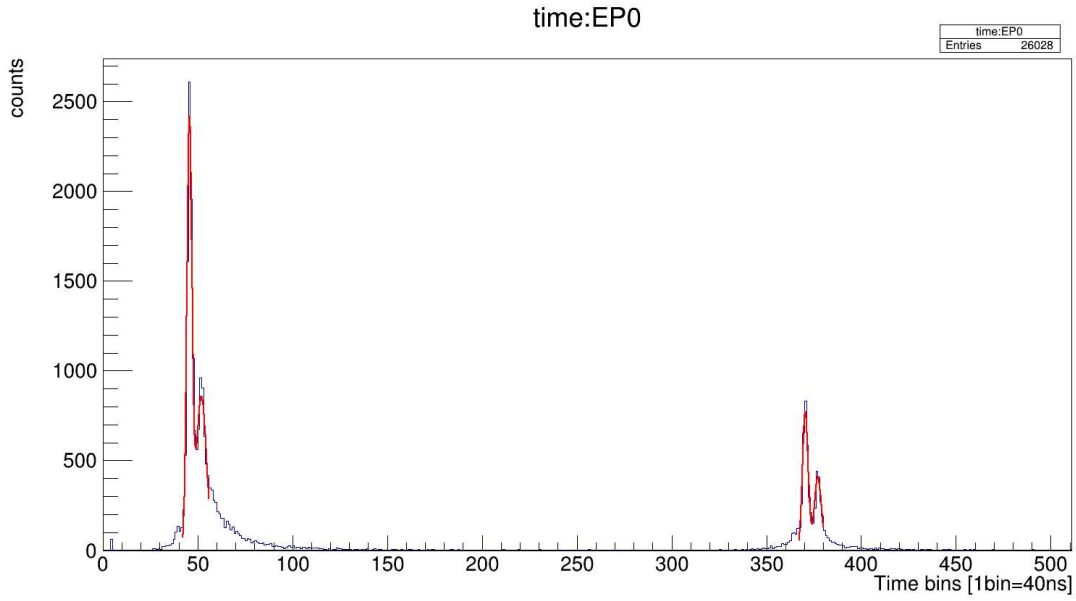

(a)

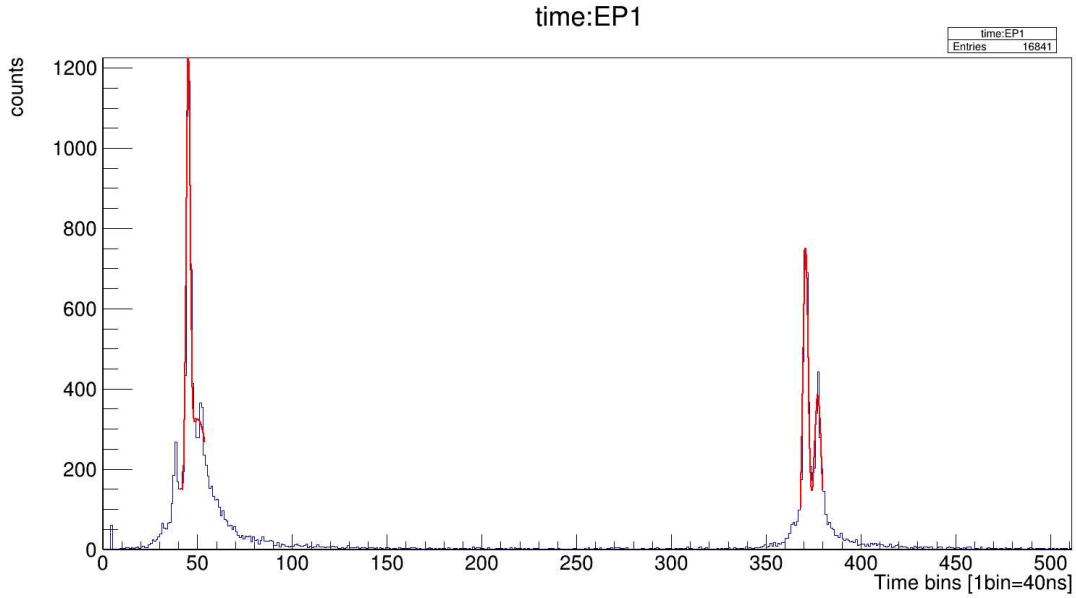

(b)

Figure 4.21: Time plots of Run 26 divided in EP0 (a) and EP1 (b), with double Gaussian fits.

both for the anode and the cathode. I investigated the possible reasons for the presence of multiple peaks. Initially, I examined the distribution of waveform amplitudes to determine if the peaks were created by neighboring pads. In Figure 4.23, the histograms show that both peaks present at the anode or cathode contain the time information primarily from the leading pads. In addition, the double peaks are equally spaced in terms of time intervals ($\sim$ 200 ns), suggesting that they might be due to a systematic error in some of the events. In order to check if the hypothetical bias is introduced by the selection I made requiring χ^2/ndf<2, I examined the ratio plot. An example is given in Figure 4.24.
The uniform distribution in the peak region seen in the ratio plot suggests that the filter does not account for the presence of multiple peaks instead of just one. Another possibility is that the trigger setup was not performing optimally, which seems to be the more credible hypothesis. One of the top scintillator squares was very noisy, and the PMTs

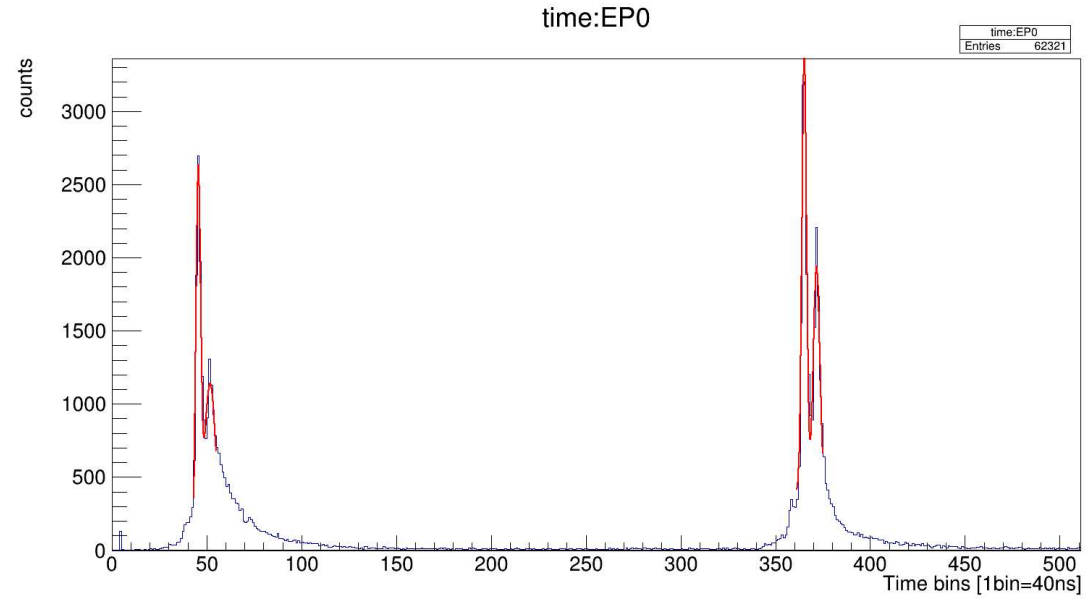

(a)

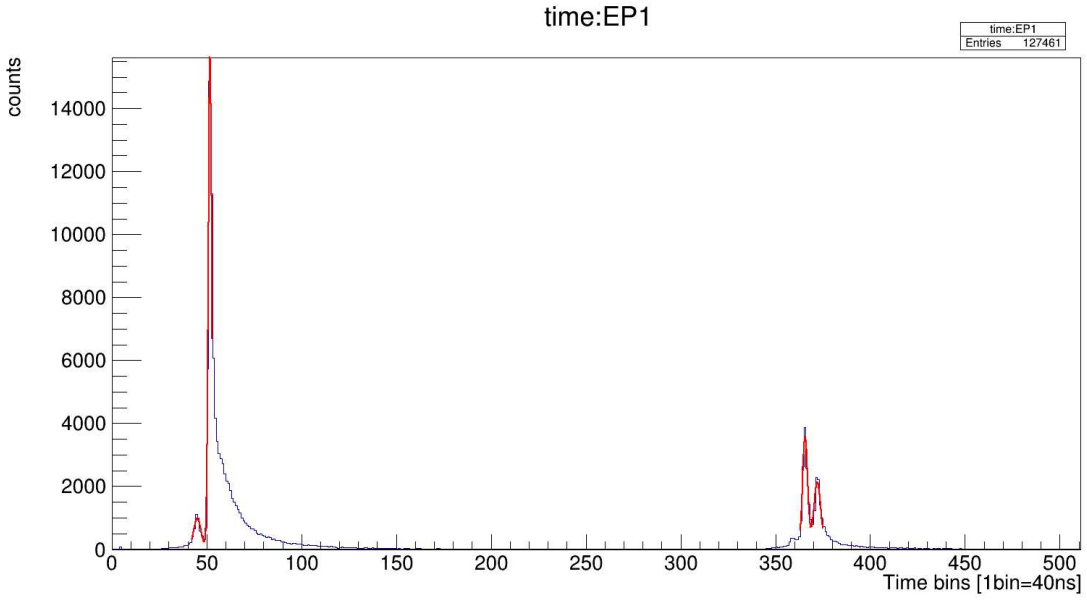

(b)

Figure 4.22: Time plots of Run 45 divided in EP0 (a) and EP1 (b), with double Gaussian fits.

were damaged. It is likely that the time difference between the two peaks is due to the noise from the scintillators. Multiple peaks are present in the time spectrum of Runs 26 and 45, but in Run 14, where only scintillator bars were used, there is only one peak for the cathode, as expected.

I performed the fit of the double peaks and computed the drift velocity by considering the pair of earlier peaks at the anode and cathode positions, taking advantage of the fixed time interval between both the double peaks. The fit is performed with a double Gaussian on the upper part of the peak because the significant background makes it difficult to model the shape of the distribution accurately. The double Gaussian fit has the

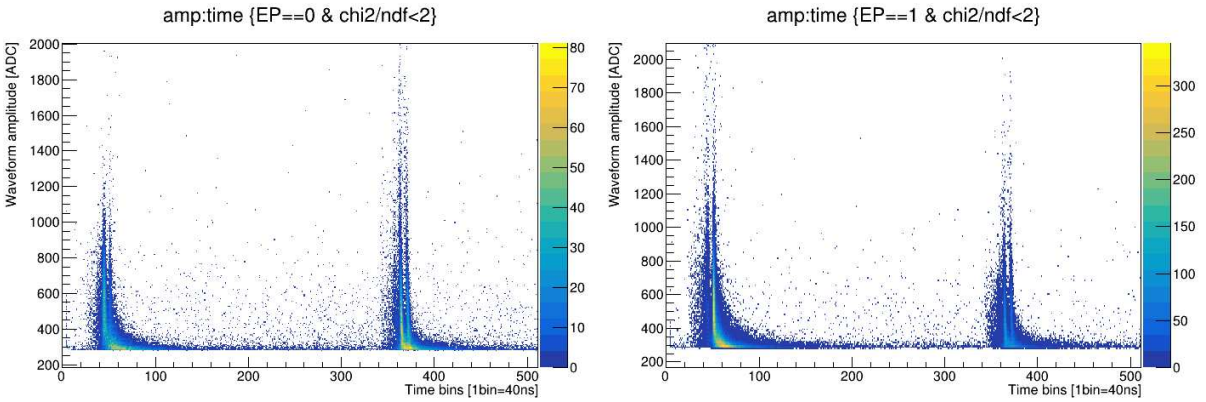

(a) (b)

Figure 4.23: Plot of the waveform amplitudes in function of the time. The distribution of the values shows that anode and cathode double peaks are both composed by leading pads signals. Neighbouring pads waveforms are also present in the tails.

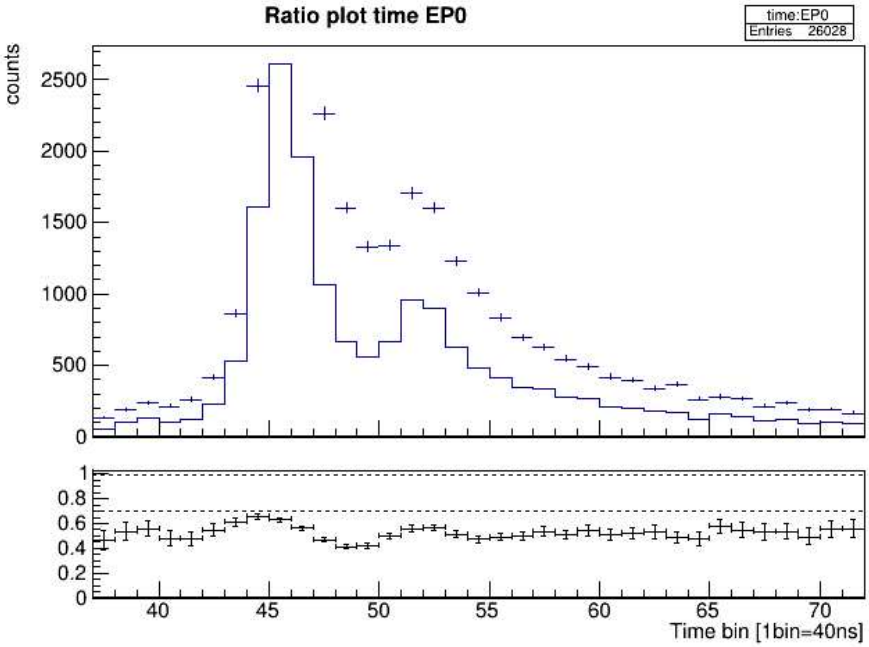

Figure 4.24: Example of ratio plot of the anode peak in Run 26 EP0. The implemented cut uniformly removes tracks from all parts of the spectrum, and the double peaks were already present.

following equation:

$$G(t) = G(t, t_1, \sigma_{t_1}) + G(t, t_2, \sigma_{t_1}) = A_1 e^{-\frac{(t-t_1)^2}{2\sigma_{t_1}}} + A_2 e^{-\frac{(t-t_2)^2}{2\sigma_{t_2}}} \tag{4.9}$$

The centroid t_1 is always considered as the reference and is termed t_a if the fit is performed on the anode double peak distribution, or t_c if the fit is performed on the cathode double peak distribution. In this way, if l is the distance between anode and cathode, the drift velocity v_d results to be:

$$v_d = \frac{l}{t_c - t_a} \tag{4.10}$$

The errors on the fit are computed through propagation using the following formula:

$$\begin{aligned}\sigma_{v_d} &= \sqrt{\left(\frac{\partial v_d}{\partial t_a}\sigma_{t_a}\right)^2 + \left(\frac{\partial v_d}{\partial t_c}\sigma_{t_c}\right)^2 + \left(\frac{\partial v_d}{\partial l}\sigma_l\right)^2} \\ &= \sqrt{l^2\left(\frac{1}{t_c - t_a}\right)^4(\sigma_{t_a}^2 + \sigma_{t_c}^2) + \left(\frac{1}{t_c - t_a}\right)^2\sigma_l^2};\end{aligned} \tag{4.11}$$

In this formula, the errors σ_{t_a} and σ_{t_c} are the standard deviations from the peak fit. The drift velocity values computed from both Run 26 and Run 45 are plotted together in Figure 4.25 with error bars.

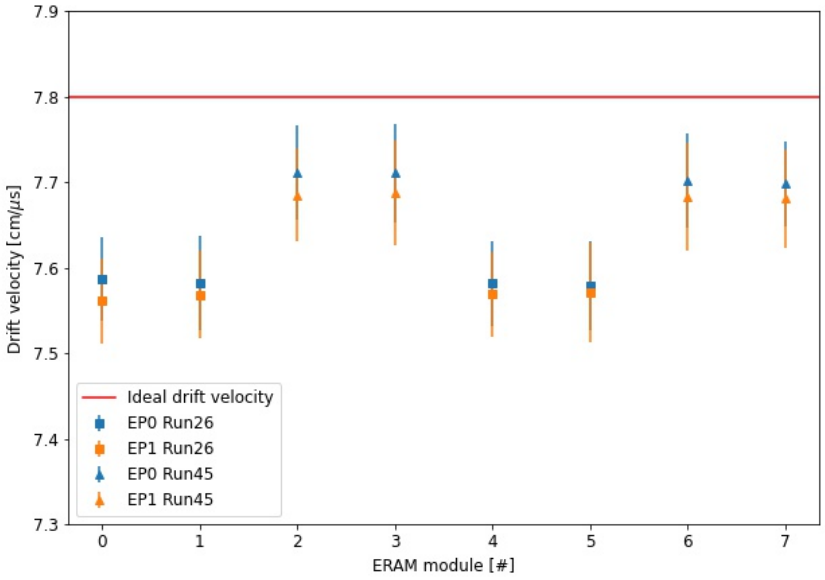

Figure 4.25: Drift velocity final plot. Values obtained from the time spectrum of Run 26 are the lower ones indicated with the square. The other values marked with triangles are computed from Run 45. In addition, the blue color is used to identify EP0 and the orange refers to EP1.

4.5.1 Summary and comments on drift velocity results

The method I developed to identify tracks crossing the anode or the cathode works effectively and provides a selection of high-quality tracks thanks to the strict cuts I implemented. A more precise determination of fit pads could be achieved by incorporating information from neighboring pads. On the other hand, the possibility to implement highly selective cuts must be supported by a very large dataset to obtain meaningful results. The results of the drift velocity calculation are shown in Figure 4.25. If the drift velocity mean difference between the endplates is negligible and within the error bars, the drift velocity computed in Run 26 is systematically lower compared to Run 45, with the latter values being closer to the ideal 7.8 cm/μs. The gas quality is indicated as the principal responsible of lower drift velocity values in Run 26. As already discussed at the beginning of this chapter, the drift velocity increases as the water content decreases. The gas flowing out of the TPC removes water from the inside, suggesting that the observed difference could be related to the amount of moisture removed during those two days.

From the Vaisala Dew-Point analyzer, the measured water contamination, after the conversion (see Section 4.2.2 for more details), was 128 ppm in Run 26 and 102 ppm in Run 45.

Chapter 5

TPC Characterization by a pulsed DUV Laser

The light of a pulsed Nd:YAG Q-switching Laser was used for the TPC characterization and calibration purposes. The Nd:YAG laser initially generates light with a wavelength of 1064 nm. By using specific crystals and lenses, the second harmonic with a wavelength of 532 nm is generated. Additional optical equipment already available with the laser is used to generate the third harmonic (355 nm) or the fourth harmonic (266 nm).
Considering the characteristics of high stability and repeatability of UV lasers, this kind of tracks, together with accurate monitoring of gas composition and density with a mass spectrometer, make possible the following studies:

- measurement of track distortions due to non-uniform electric field;
- precise measurements of the drift velocity by photo-extraction from the cathode and the anode;
- measurement of dE/dx energy resolution, by properly normalizing the ionization charge by the total energy of the single laser pulse in order to have Gaussian fluctuations of the local energy release;
- measurement of track space resolution and biases in reconstruction, by using appropriate beam focusing so to constrain the laser beam position fluctuations;
- measurements of the ERAM detectors alignment.

My thesis work addresses the first two goals, with an additional study on a modulation effect along the z direction of the track time spectrum.

The double-photon ionization

The T2K gas mixture is Ar:CF_4:iC_4H_{10} (95:3:2). In Chapter 4 the gas quality is discussed, addressing the problem of external contaminants such as H_2O, O_2, and N_2 to understand the detector performance. The data collected in that first phase came mainly from cosmic muons crossing the TPC ionizing the gas. While the cosmic rays in that setup were sufficiently energetic to ionize the gas, a single photon from the most energetic light component of the laser, so $\lambda = 266$ nm, provides an energy of 4.8 eV, which is not sufficient to ionize even isobutane, the gas with the lowest ionization energy in the mixture, equal to 10.8 eV. The same light cannot also ionize the above mentioned major contaminants, since they have a greater ionization energy than isobutane. However, in the TPC, a straight track is produced by the laser. The most probable interaction which is responsible for

track generation is the double-photon ionization of organic impurities [44] already present in the T2K gas. From the vendors, the gas purity of the Ar and CF_4 is usually 99.999%, but for the isobutane it is 99.9%. The contaminants introduced with the isobutane are organic impurities with ionization energies lower than 9 eV. Two photons of the 266 nm DUV light can ionize impurities in the gas providing ~ 9.6 eV through the double-photon ionisation process [45].

Additive [a]	Ionisation potential (eV)	Vapour pressure (Torr) 20 °C (0 °C)	Melting point/ boiling point (°C)	Ionisation (e^-/cm) for 1 μJ in 1 mm^2 and 10^{-3} Torr additive
Benzene C_6H_6	9.24	77	55/80	266: 5×10^3 [26,27]
Toluene C_7H_8	8.82	22	−95/110	266: 5×10^4 [26,27]
				0.5×10^4 [19]
Cumene C_9H_{12}	8.69	3.8	−96/152	266: 11×10^4 [26,27]
n-Butylbenzene $C_{10}H_{14}$	8.69	1	−88/183	266: 5×10^4 [26,27]
m-Xylene C_8H_{10}	8.56	6	−48/139	266: $\leq 4\times10^4$ [26,27]
TMA $(CH_3)_3N$	8.5 [21]		−117/2.9	266: 60–130 [15,17]
	7.8 [26]			80 [24]
1,3,5 Mesithylene C_9H_{12}	8.40	1.5	−45/165	266: 1.8×10^4 [26,27]
Phenole C_6H_5OH	8.3		41/	266: > 250 [25]
	8.51 [17]			
Naphthalene $C_{10}H_8$	8.12 [17]		81/	266: 560 [25]
TEA $(CH_3CH_2)_3N$	7.5 [26]	50 (12)	−114.7/893	266: 200 [17]

Figure 5.1: Properties of contaminants with low ionization potential. Values for ionization density (I.D.) extrapolated assuming I.D.$\propto I^2p$, a laser pulse of 1 μJ and 1 mm^2 cross section and a partial pressure of contaminants $p = 10^{-3}$ [44].

Moreover, for calibration purposes, the optimal incident laser energy density has been calculated according to literature to be in the interval between 1 μ J/mm^2 to 1.4 μ J/mm^2 for the T2K gas. This requirement is needed to perform TPC calibration because it simulates the signal of $1 \sim 2$ MIPs, which can generate $100 \sim 200$ electrons per centimeter in an argon-based gas mixture [45].

5.1 Experimental setup

The Minilite Nd:YAG laser [46] is a Q-switched laser producing light with a pulse width of approximately 5 ns and a trigger rate that can be adjusted between 1 Hz and 15 Hz. The laser light entered the TPC through the quartz window present in the aluminum box. A photo of the quartz window is provided in Figure 3.5(b). The angle of incidence of the beam could be varied in order to study different features of the detector. The drawing in Figure 5.2 shows the trajectory of the laser light in one TPC. The laser produces electrons in the volume through two-photon ionization as it interacts with the gas until reaching the cathode. At this point, the laser light interacts with the copper layer, extracting electrons via the photoelectric effect. Although reflections of the laser light can occur, they do not cause ionization in the gas.
A MgF_2 defocusing lens was attached to the quartz window and was used to demonstrate that focusing the laser light is necessary to produce a track in the gas, supporting the two-photon ionization hypothesis. See Section 5.3 for the plot.

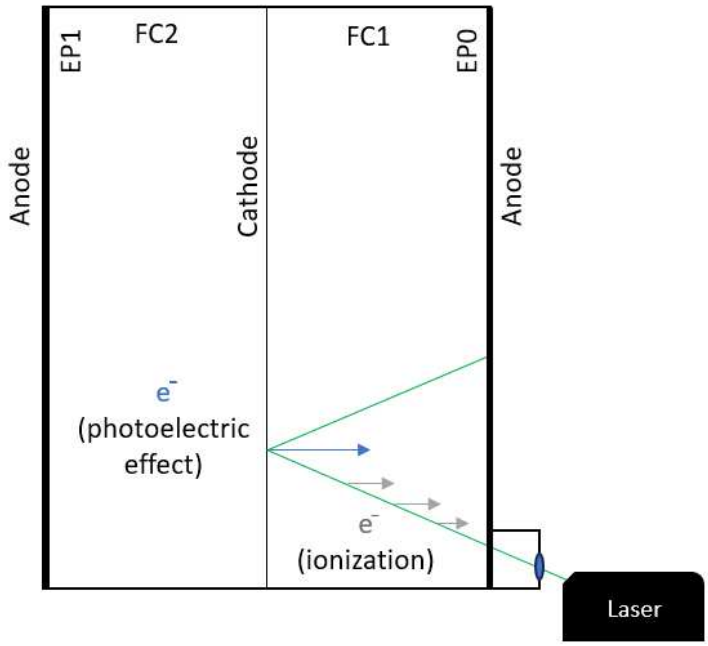

Figure 5.2: Drawing of the top view of the laser trajectory in the TPC. Along the track, electrons are generated by ionization, while at the cathode, they are generated by photoelectric effect.

5.2 Laser tracks description

Since the incident angle had very limited variability, the tracks were primarily read by a single ERAM, the top left one. The track appears in the anode projection, the xy plane, as a straight line with a spot at the end. This shape highlights the presence of two phenomena: the track produced by ionization and the arrival at the cathode, where a significant peak of charge is released due to the photoelectric effect of the light on the copper. The two plots I am showing in Figure 5.3 refer to two runs at different angles. The laser is horizontal, and only the incident angle, between the direction of the beam and the xy plane, which I will refer to as θ, could be changed between approximately 75° and 87°.

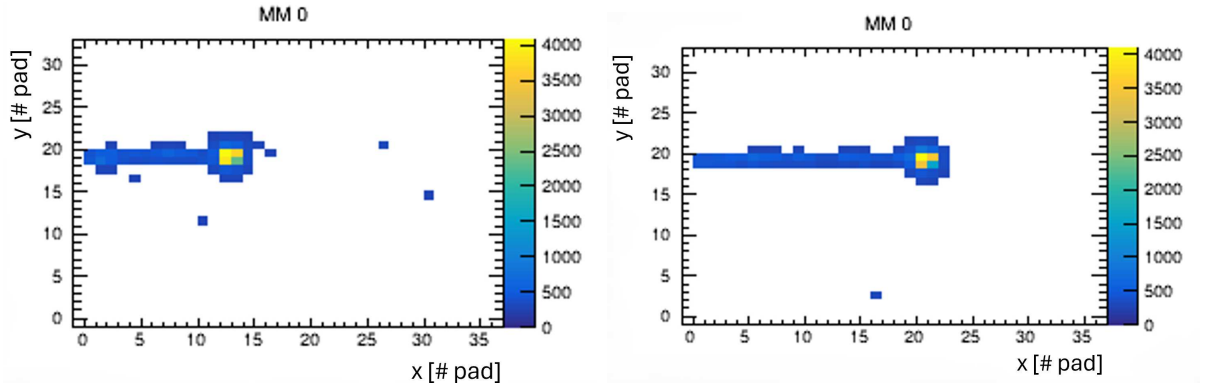

(a) (b)

Figure 5.3: Laser tracks at different angles: 81.4° in (a) and 78.9° in (b), the two runs were both taken with cathode HV=18 kV.

The typical waveforms produced by the laser have an amplitude between 450 and 800 ADC counts. An example is given in Figure 5.4, to be compared with the one provided

in Figure 3.8. The most evident characteristic is the very low signal amplitude, which is due to the few electrons generated by the laser.

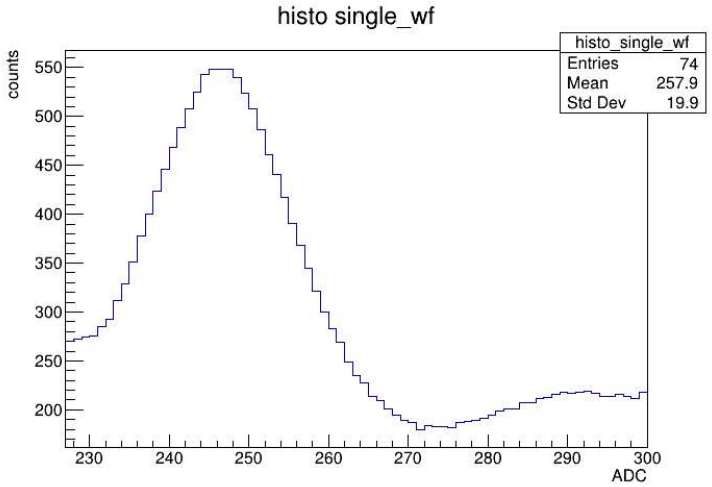

Figure 5.4: Typical waveform along the laser track.

If the previous example shows the waveform produced in the gas, the following Figure 5.5 provides a focus on waveforms generated by the charge extracted from the cathode. The yellow pad highlighted in the plot on the left side corresponds to the waveform in the middle of the matrix on the right. The spot is formed by the neighbouring pads collecting the charge spread in the resistive foil. It is clearly visible the saturation of the leading pad reaching the 4096 ADC counts.

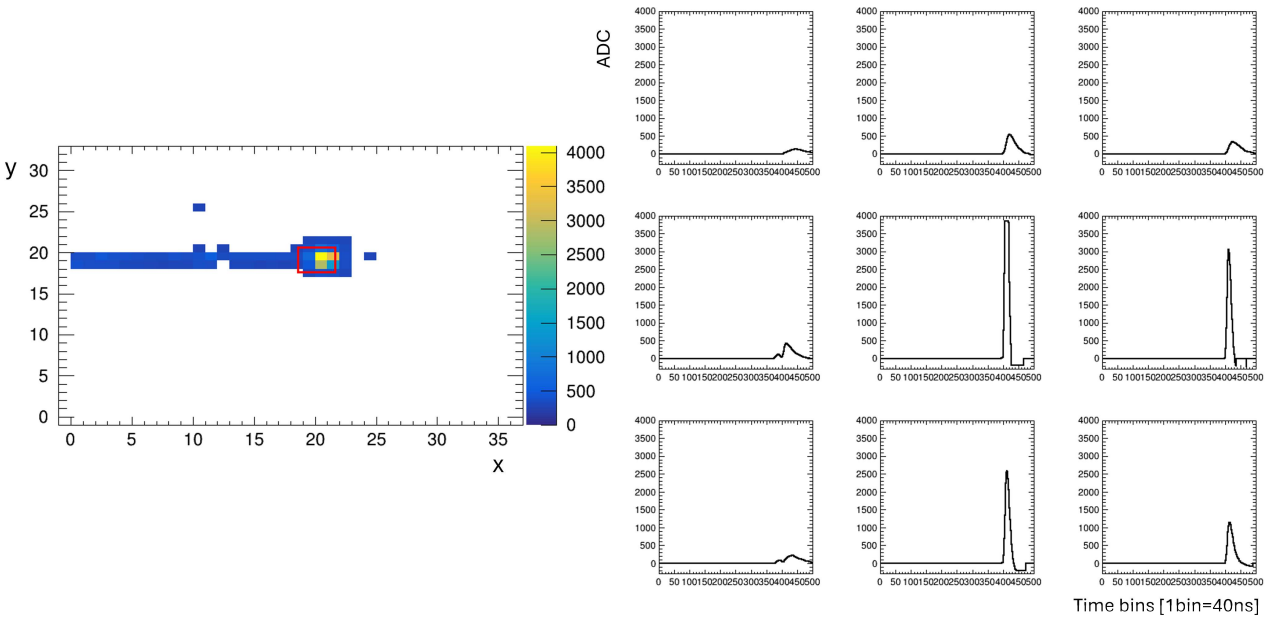

Figure 5.5: On the left, the xy projection of a track where the cathode spot is visible from the number of pads involved around the leading pad, highlighted in yellow. On the right, a matrix of waveform plots shows the spread of the charge from the leading pad to neighbouring pads.

The two previous plots 5.3 (a) and (b) show only the projection of the track in the xy plane, corresponding to the readout plane where the ERAMs are attached. The z direction inside a TPC is proportional to the time of arrival of the charge at the readout plane. The

3D reconstruction of the track is done by taking into account the two spacial projections and the time information (z-axis). For a laser track the typical time spectrum is the following.

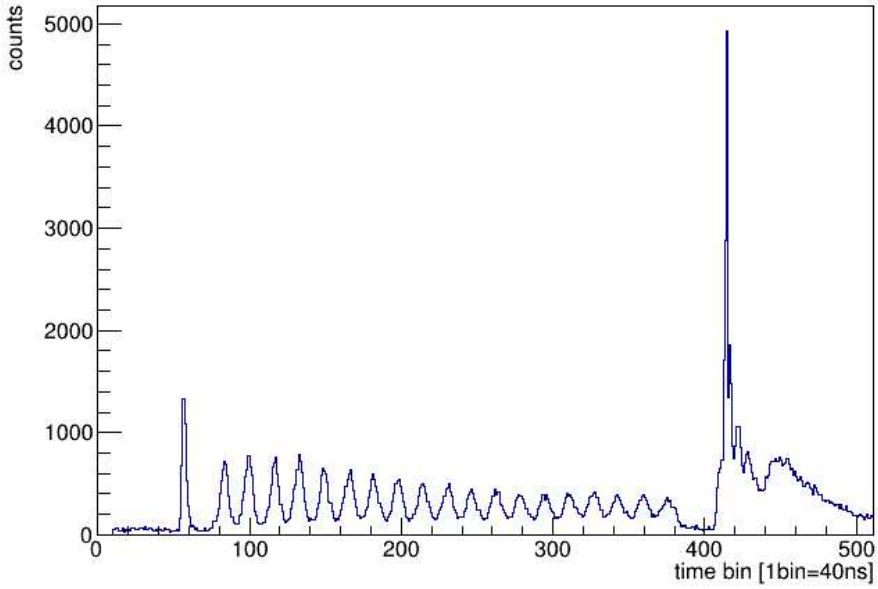

Figure 5.6: Time spectrum of Run 131, with $\theta = 78.9°$ and cathode HV=18 kV.

The total number of available bins is 511, but the ADC sampling rate can be varied from 100 MHz to 1.25 MHz. Depending on the cathode voltage set to perform the measurements the ADC sampling rate is varied to reach the optimal configuration. In the case of the plot in Figure 5.6, the time bin is set to the standard value of 40 ns.
The most noticeable characteristic of the time spectrum is the presence of multiple peaks. The only one expected is the highest peak on the right side of the plot corresponding to the cathode position. In my thesis, I conduct a detailed study of the laser tracks to understand the origin of the additional peaks. A full comprehension of the time spectrum distribution is essential for a deeper understanding of the signals generated by the laser tracks.

5.3 The time spectrum

In Figure 5.6 an example of a time spectrum is shown. As previously mentioned in the general description of the laser tracks, multiple peaks are present, most of which had unknown origins at the beginning of my thesis work. The only known peak from cosmic rays time spectrum is the highest one, which corresponds to the position of the cathode in time bins. The following discussion aims to identify the sources of the peaks and explain why they have their specific shapes.

A MgF_2 defocusing lens was used to determine if the track was visible with non-collimated light. Figure 5.7 shows the time spectrum of the run, where only the cathode peak is present. The cathode is visible because the light impinging on the copper plate generates electrons through the photoelectric effect. In the gas, double-photon ionization is necessary to produce charge.
Starting from the first peak on the left in Figure 5.6, which corresponds to the anode position, it can be considered as the reference time for computing distances. Electrons generated at the anode do not drift, but immediately produce an avalanche in the gap

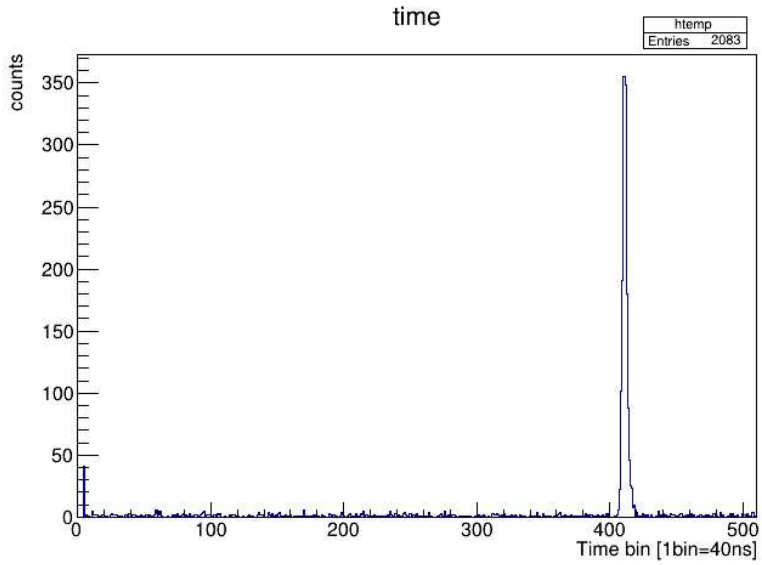

Figure 5.7: Time spectrum of a run where a MgF_2 lens was fixed to the quartz window, and the cathode voltage set to 18 kV.

between the mesh (at ground) and the resistive layer. A confirmation of the hypothesis comes from the occupancy plot on Figure 5.8, where the accumulation of events around 60 time bins on the time axis is present at all x positions. This demonstrates that laser light is reflected by the cathode to the anode surface.

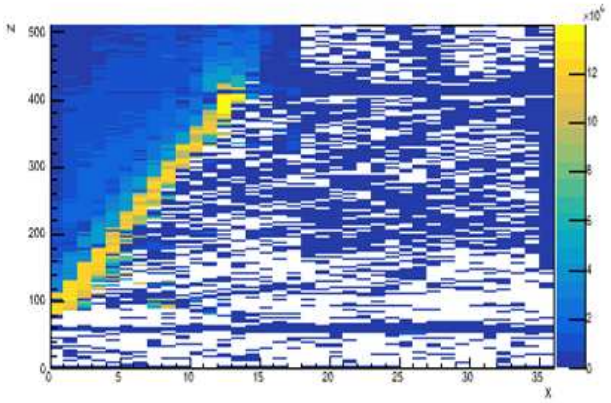

Figure 5.8: Occupancy plot cumulatively showing the tracks projected in the zx plane.

Considering again the plot in Figure 5.6, the peaks on the right side respect to the cathode peak correspond to the spreading of charges from the cathode high amplitude signal. This happens because the charge spreading circularly on the resistive layer takes some time to move on the material and the induced current to be collected by the underneath pad. In the time spectrum, the neighbouring pads appear as events arriving from a more distant point than the cathode position.
The other peaks belong to the track in the gas. The distance between the anode peak and the first peak of the track is proportional to the distance, in the z direction, between the ERAM plane and the point where the beam enters the volume read by the pads. On the other side, the distance between the last peak of the track and the cathode peak is due to the presence of double peaks in the waveform, and the reconstruction algorithm takes the highest one. An example of a waveform containing information from both the charge produced in the gas near the cathode and from the cathode itself is shown in the following

Figure 5.9. In the laser tracks, the signal from the neighbouring pad of the cathode is

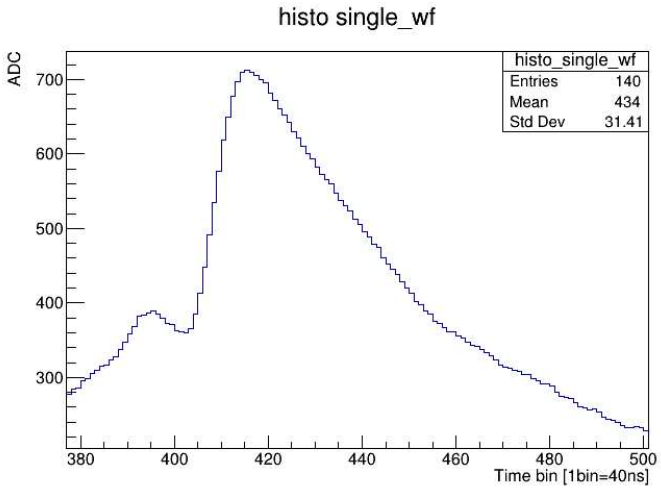

Figure 5.9: Waveform selected near the cathode showing two peaks: the first is the signal from the gas ionization generated close to the cathode, and the second is the neighbouring pad of the cathode signal.

higher than the waveform of the track. As a result, only the delayed signal is considered, appearing in the time spectrum as one of the peaks after the cathode peak.
Finally, the modulation of the track was completely unexpected. My analysis work on the laser tracks understood the issue and provided an explanation for the presence of those peaks. In Figure 5.10 the plot of all the waveforms of Run 131 in function of the time is provided. Looking at the waveforms around the cathode, we see that the top of the peak is cut off, indicating the effect of saturation on the cathode. Another noteworthy feature is the reproduced modulation along the track.

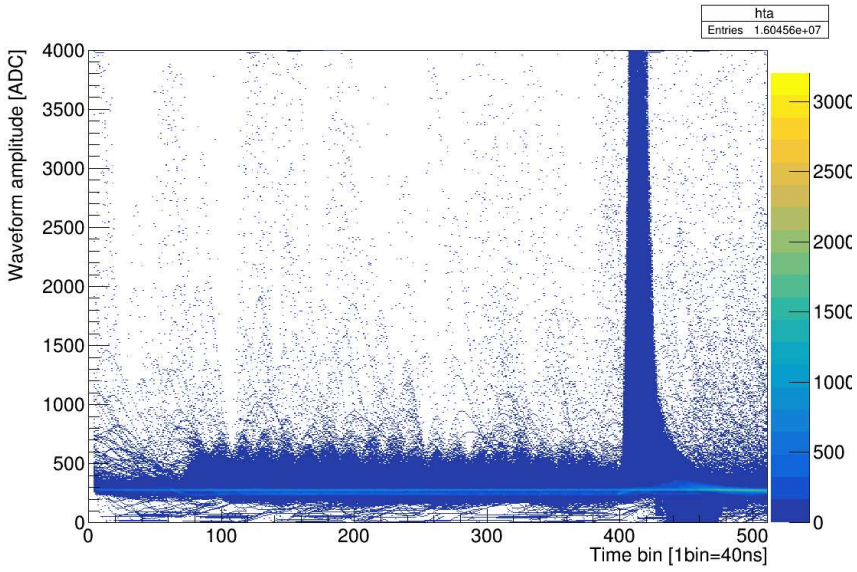

Figure 5.10: Full plot of Run 131 waveforms in function of z.

The oscillating behaviour of the time spectrum could be more appreciated from the focus on the track waveforms scale of the same plot. Figure 5.11 highlights also the presence of an unexpected "yellow line", indicating a region where events are more concentrated, appearing horizontally across the graph.

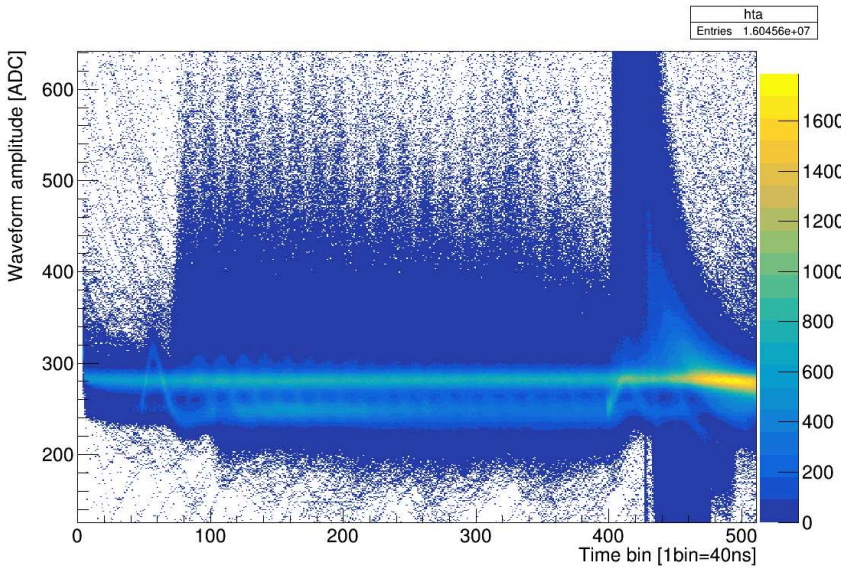

Figure 5.11: Same plot of Figure 5.10 with a zoom on the y axis revealing the modulation pattern on the waveform distribution.

The "yellow line" and the oscillations along the tracks can be beautifully isolated by a precise selection on the pads and on the size of the waveforms, as shown in Figure 5.12 (a) and (b).
The possibility of separating the waveforms collected from each pad, leads to the solution of the modulation issue. Scanning the array of hit pads along the x direction makes it possible to isolate each individual peak. The matrix of plots in Figure A.4 shows the perfect matching of the peaks with the selection of the pads in x.

5.3.1 Conclusions on the modulation issue

The modulation issue in the time spectrum is demonstrated to be related to the geometry of the ERAM detectors and to the geometry of the setup with an accumulation of the exact same tracks position and directions. An ERAM detector is a matrix of pads, with each pad reading the charge from a virtual column of the TPC volume. As already explained in Section 3.2.2, the time of maximum amplitude should be associated to the pad center. The reason of obtaining regular peaks on the time spectrum of the maximum of the waveforms is that a single pad in x is reading a single position of the tracks in z. Indeed in other setup, like cosmic tests, the tracks are randomly crossing the cage at different positions and angles. While in the specific case of laser, a single run corresponds to the accumulation of tracks having the same position and angles. The shape observed for each individual pad is given by the convolution of the electronic response and the charge collection on the anode plane. This initially results in high-amplitude, short-duration peaks followed by an undershoot as the charge spreads and leaves the main pad. The superposition of these high amplitude peaks gives the modulation observed on the initial time distribution. In this way, a peak in the time spectrum is linked to the spatial position of the pad center. Each peak of the time spectrum, in the region of the track produced in the gas, can be precisely isolated by selecting the corresponding x coordinate.

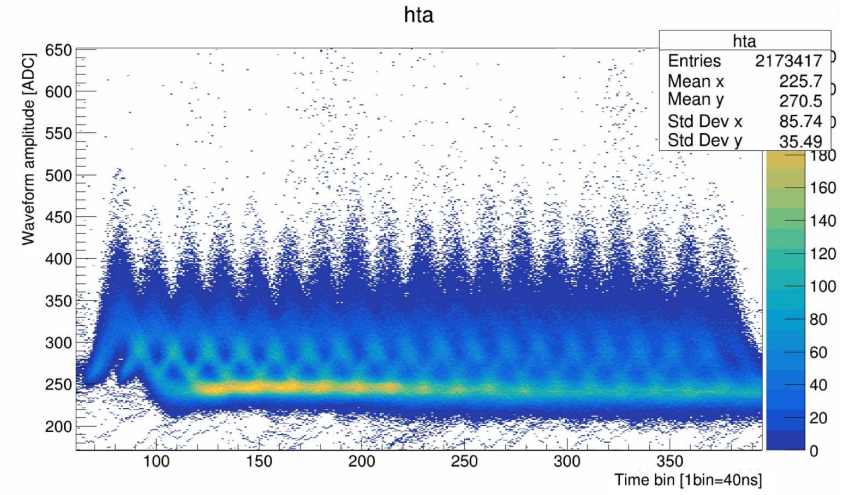

(a)

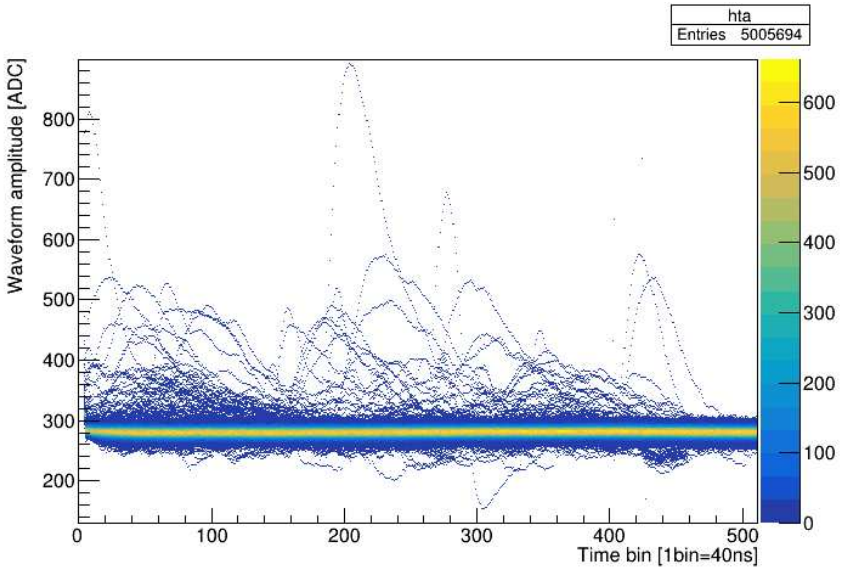

(b)

Figure 5.12: The waveforms cleaned by the noise (a) and the noise from a pad (b).

5.4 Preliminary study on laser tracks spreading and beam spot estimate

Once understood the modulation issue on the time spectrum, I focused the first goal of my analysis in describing the beam and evaluating the size of the laser beam spot. The importance of this analysis lies in the necessity to put an upper limit to the electric field non-uniformities. The nominal diameter of the laser beam is 3 mm, whereas the electric field non-uniformities are expected to be in the range of hundreds of μm. Therefore, the primary aim of this work is to first estimate the dispersion of the track direction, and then determine how much the laser beam to reach needs to narrow to achieve the required resolution. In addition, the analysis of the beam cross section should reveal the shape of the beam eventually showing the presence of reflected beams.

5.4.1 Laser tracks pre-analysis

My work began by extracting useful information from the data contained in the file provided by the DAQ system. Since I want to study only laser tracks, a first cut on the number of hits per event was set before the pre-processing step, cleaning data from possible cosmic ray particles. The code devoted to this first phase reconstructs and collects the following information for each hit:

- Event number;
- Endplate ID;
- Module ID;
- x position (pad number on the ERAM in the x direction);
- y position (pad number on the ERAM in the y direction);
- Maximum of the waveform (amplitude);
- Time of the maximum in time bins (z position);
- Waveforms;
- Waveforms size.

The first goal of the data analysis is to describe the laser tracks with a 3D fit in the TPC volume. This is a mandatory step to measure the uniformity of track directions and angular distributions. For this purpose, a second selection is made considering the hits belonging to the top left ERAM module where the laser tracks are projected. The cathode spot, visible in Figure 5.3, is excluded from the fit and removed from the analysis of the track. The motivation lies in the process of charge production at the cathode, which is due to photo-extraction. Multiple pads are involved in the readout of the charge from the cathode, spreading in the resistive foil, since the charge values are significantly higher with respect to the one produced in the gas, most of the time saturating the ADC.

A linear fit of the track was necessary to determine the distribution of laser tracks in the TPC volume. The collection of points to be fitted, with coordinates x_{fit}, y_{fit} and z_{fit}, was calculated from the available hit pad information. Since the laser produces straight tracks and the direction was chosen to be horizontal to the floor, I sliced the track in vertical columns computing a y_{fit} coordinate for each x_{fit}, actually corresponding to the ERAM pad number in the x direction, using the information from the waveforms. Specifically, the hit pads of the column have been summed and weighted with the waveform amplitudes in the following way:

$$y_{fit} = \frac{\sum_i (y_i \times A_{wf_i})}{\sum_i A_{wf_i}} \tag{5.1}$$

The z_{fit} coordinate is calculated in the same way. Each point is associated with the mean of the waveform amplitudes. The set of points describing the track is subsequently fitted with the Principal Component Analysis method.

5.4.2 The Principal Component Analysis (PCA)

Each selected hit contains the information enumerated in the previous paragraph. From the information on the x, y and z position I want to perform a 3D fit. The approach I chose to use for this task is the Principal Component Analysis (PCA).

The main objective of PCA is to find a set of new variables, called principal components, which describe the dataset identifying the direction where there is maximum variance. Data are firstly transformed to the same scale in a process called *standardization*, in this way an equal contribution of all the values is guaranteed. For each value I calculate:

$$z = \frac{value - mean}{\sigma_{dev}} \tag{5.2}$$

where σ_{dev} is the standard deviation.
The second step is the *covariant matrix* computation, which is a square matrix. In the case of the TPC volume the dimensions are three (x,y,z):

$$C = \begin{pmatrix} \sigma_{xx} & \sigma_{xy} & \sigma_{xz} \\ \sigma_{yx} & \sigma_{yy} & \sigma_{yz} \\ \sigma_{zx} & \sigma_{zy} & \sigma_{zz} \end{pmatrix}. \tag{5.3}$$

The diagonal terms represent the variances, while the upper and lower triangles indicate the degree of correlation between the variables. In the following step eigenvalues and eigenvectors are computed solving the characteristic equation:

$$CV_i = \lambda_i V_i \tag{5.4}$$

where i=1,2,3, λ_i are the eigenvalues and V_i are the correspondent eigenvectors. The latter are arranged in a matrix like:

$$V = \begin{pmatrix} V_{1x} & V_{2x} & V_{3x} \\ V_{1y} & V_{2y} & V_{3y} \\ V_{1z} & V_{2z} & V_{3z} \end{pmatrix} \tag{5.5}$$

where V_1, V_2 and V_3 are the eigenvectors decomposed into the three original coordinates, ordered from the greatest eigenvalue to the smallest. This method is typically used to reduce the number of dimensions in a dataset while retaining as much information as possible.

My goal was to perform a 3D fit, so I created a matrix where the three spatial coordinates were converted to millimeters: x_{fit} was multiplied by 10.09 mm, y_{fit} by 11.18 mm, and the time information z_{fit} by the bin width of 40 ns and the drift velocity I computed in the previous Chapter (4). On the matrix of hits coordinates converted to mm selected to be fitted, is then performed the PCA.

Calculating the angles: θ and ϕ

From the PCA I have the eigenvectors describing the track in the volume. I define the θ angle as the one between the xy-plane, so the anode, and the z direction. The other angle, ϕ, is the angle swept in the xy-plane. I can compute the two angles θ and ϕ in the following way:

$$\theta = \frac{\pi}{2} - \arctan \sqrt{\frac{V_{1x}^2 + V_{1y}^2}{V_{1z}^2}} \tag{5.6}$$

$$\phi = \arctan \frac{V_{1y}}{V_{1x}} \tag{5.7}$$

where V_{1x}, V_{1y} and V_{1z} is the principal component normalized vector found with the PCA. The plots in Figure 5.13 show the two distributions.

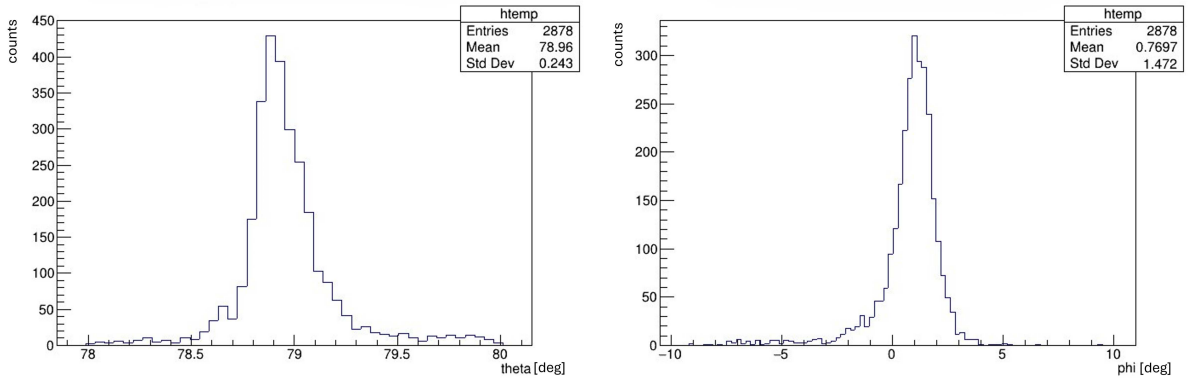

(a) (b)

Figure 5.13: In these plots is shown the distribution of the angle θ in (a), and in (b) the distribution of the angle ϕ.

Finally, I computed from the PCA information the beam spot on the xy plane. The plot in Figure 5.14 shows the distribution on the plane of reconstructed positions of tracks crossing the plane in $z = 0$.

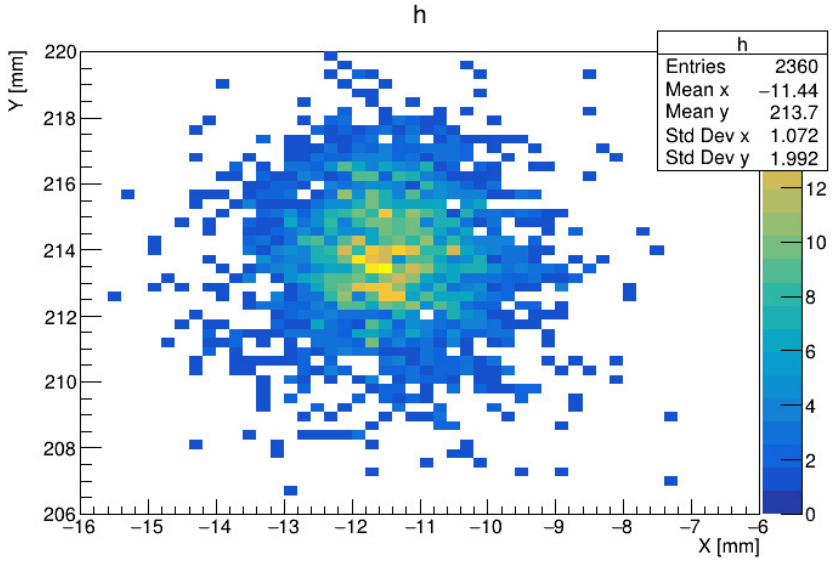

Figure 5.14: Reconstructed spreading of the tracks in the projection plane with z=0 providing the shape of the beam spot.

5.4.3 Comments on beam spot measurement

The nominal beam spot size from the laser data-sheet is 3 mm [46]. The measured beam spot inside the TPC is a statistical estimation, where the standard deviations on the two directions indicate that the 68% of the tracks cross the anode plane in that region. Taking as beam spot size two time the standard deviation (in this way including the 95.5% of the tracks), in the y direction the beam is large 3.67 mm, while in the x axis the beam is 2.14

mm. The size is compatible with the data-sheet previously cited. The angular spreading of the track direction can be evaluated by examining the θ and ϕ angle distributions. Lastly, it is noteworthy that no secondary reflected beam is visible in the beam spot plot (Figure 5.14).

5.5 Drift velocity study from laser tracks

In Section 5.3 i discussed the shape of the time spectrum for laser track runs. Among the recognised peaks, the anode and the cathode peaks positions are used to determine the drift velocities. This study was conducted by collecting data over several runs, setting different cathode voltages between 10 kV and 30 kV in increments of 2 kV. The laser was kept at the same fixed angle, but the time bins along the z direction were adjusted at different intervals to measure the electrons arriving from the cathode at each set voltage. The drift velocity of electrons is expected to increase with the cathode voltage until it reaches a maximum, after which it slowly decreases. The electrons increase their velocity in the gas while the interactions remain elastic scattering. After the peak, electrons have enough energy to interact with the gas through inelastic channels. The observed effect is a reduction of the drift velocity. In Figure 5.15 and 5.16 the measured drift velocities are plotted as a function of the cathode voltage and of the electric field respectively, expecting to reach the highest value of drift velocity at 27.5 kV. The drift velocities are computed following the same method used in Chapter 4, so dividing the length of the TPC, l, measured by metrology, by the time an electron generated at the cathode takes to reach the anode. The positions in the time spectrum of the anode and cathode peak centroids are measured performing Gaussian fits. The drift velocity errors are computed through error propagation.

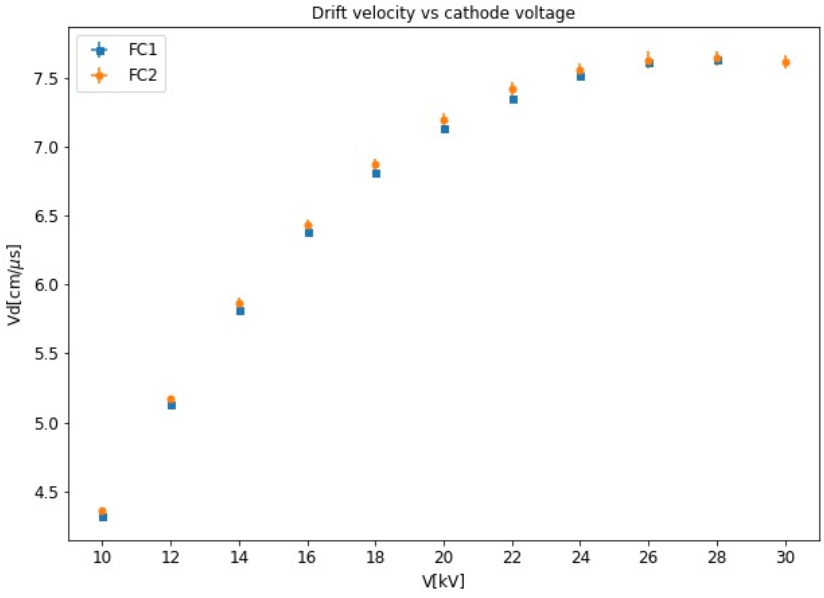

Figure 5.15: Drift velocity from the laser as a function of the cathode voltage. Data in blue are taken from FC1, so EP0, while the orange from FC2, corresponding to EP1.

The plot of drift velocities as a function of the electric field (Figure 5.16) displays both simulated values for a pure T2K gas mixture, with Magboltz and Garfield, and the measurements obtained in the TPC. A systematic shift of the measured data to lower values

is evident, and this behavior can be attributed to two possible causes. The first is the level of water contaminants inside the gas. As already explained in Chapter 4, water molecules are polarized and slow down the drift of electrons. The second issue arises from the waveforms saturating at the cathode. The magnitude of charge generated by the laser through the photoelectric effect is so high that the electronic readout of the pad reaches its limit. Since the DAQ associates the time of the maximum amplitude of the peak with the falling edge, the recorded time is greater and the calculated velocity is smaller.

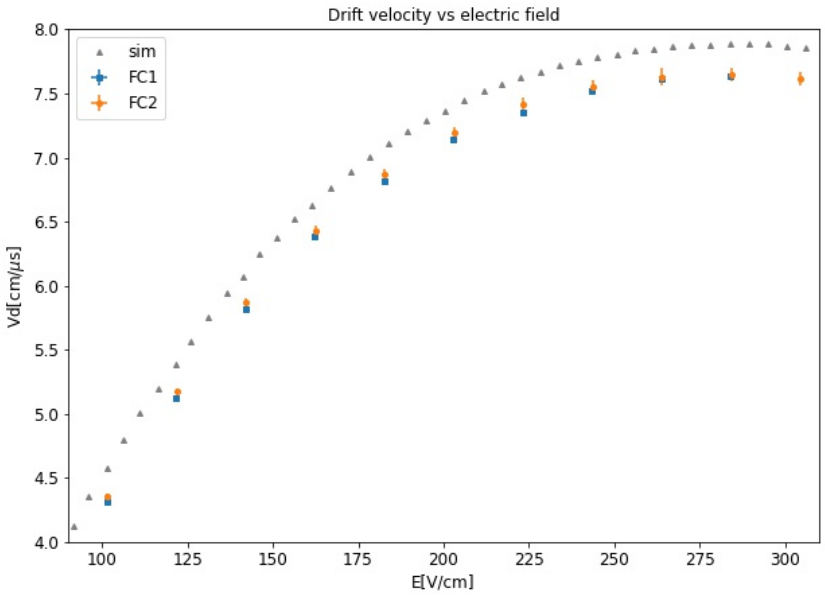

Figure 5.16: Drift velocity from the laser as a function of the electric field with simulated data. In blue are shown data from FC1, so EP0, while in orange data from FC2, corresponding to EP1.

The drift velocity measurements greatly follow the same trend of the simulation and shows that the working conditions of the HATPC (electric field E=275 V/cm) provide the highest possible drift velocity in the T2K gas. This study must be compared with the previous study of the drift velocity from cosmic data.

5.6 Final comments on laser tracks

The high stability and repeatability of the laser tracks, combined with accurate monitoring of gas composition and density, can be utilized to study detector performance in a future laser data-taking campaign. The study I conducted on these tracks confirms the necessity of narrowing the beam to a width below one millimeter to perform measurements of spatial resolution, potential reconstruction biases, dE/dx measurements, electric field non-uniformities, and alignment. However, the measurement of drift velocity was successfully performed.

The Nd:YAG Q-switching laser was tested for calibration purposes to study the track characteristics inside the HATPC detector. Initially, I examined the shape of the tracks at the waveform level to understand the detector's response to the two charge production processes 5.2. The track in the gas is produced through two-photon ionization, resulting in very low amplitude waveforms collected from the pads. At the cathode, however, the

charge is produced through the photoelectric effect. In this case, the waveform of the leading pad shows saturation of the readout electronics, and the charge spreading on the DLC generates signals in several neighboring pads.
The analysis of laser tracks can be summarized in three main goals. First, an unexpected modulation was found in the time spectrum, and the origin of this effect was unknown. Studying the waveform distribution I found that the modulation comes from the shape of the ERAM detector, from the way the signal is generated, from the straight tracks produced by the laser and from their horizontal direction. A single pad in x is reading a single position of the tracks in z showing in the z axis a peak for each pad along x. Second, I computed a estimation of the beam spot exploiting the PCA method to find the distribution of the points where the laser tracks cross the anode plane. In this way, I could evaluate the spreading of the tracks. I found that the measurements are compatible with the 3 mm nominal size on the laser data-sheet. The last part in section 5.5 is devoted to the drift velocity calculation. I took several laser runs varying the cathode voltage from 10 kV to 30 kV at step of 2 kV. The results are shown in Figure 5.15 and 5.16, where the measurements beautifully follow the trend of the simulation.

Chapter 6

HATPC commissioning at Tokai

At the beginning of December, I arrived at J-PARC to participate in the activities during the first neutrino Run after that ND280 temporarily stopped its operations in 2021 to prepare for the significant upgrades planned for the detector.
Once the the bottom HATPC arrived to J-PARC, after being shipped from CERN, it was lowered into the pit and fitted into the Upgrade Basket. Commissioning runs were conducted using cosmic rays to ensure that everything was functioning correctly. The configuration of the ND280 detector in December accounted for the legacy detectors, except for the P0D, which was removed and its volume filled with Upgrade detectors ready at that moment: the bottom HATPC, the SFGD, and four panels of the TOF. The performance of the SFGD was limited due to the absence of electronics necessary to read signals from scintillating fibers in all three directions, as only two directions were instrumented. Although all six TOF panels were available at J-PARC, only four were installed to avoid the risky "put in and take back" dynamics.

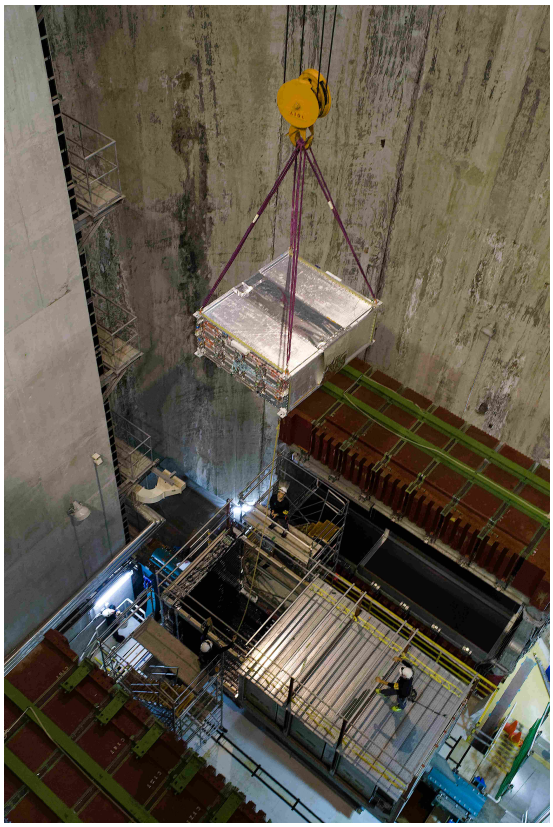

Figure 6.1: Bottom HATPC instrumented with ERAMs lowered in the ND280 pit.

Figure 6.2: Bottom HATPC, SFGD and three TOF panels installed in the Upgrade Basket.

Figure 6.1 shows a photo taken during the installation of the bottom HATPC. In the picture, you can see the original detectors inside the opened UA1 magnet, and above them, the TPC being lowered 30 meters from the surface to be fitted into the ND280 detector. In Figure 6.2, the detectors installed before the beginning of Run 12 are shown. The empty volume in the basket is the space for the top HATPC, which was still under construction at CERN at that time.

During my stay, I joined the members of the collaboration in the control room, participating in all activities. I contributed to the efforts of running all detectors synchronously in the global DAQ, monitoring the HATPC functioning, and checking data quality parameters. I also learned a lot about the procedures for supervising data taking and ensuring detector functionality by shadowing the shifters in their tasks.

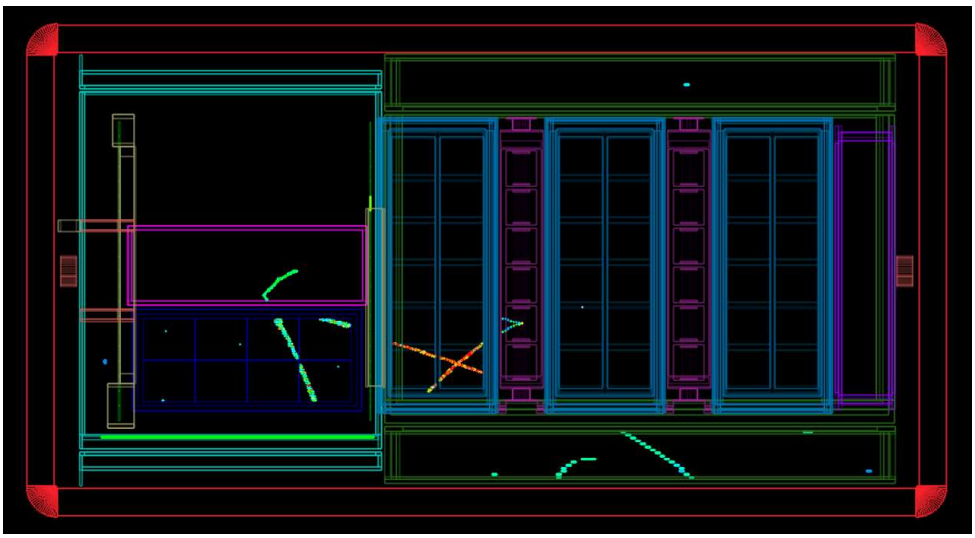

Figure 6.3: Neutrino interaction visualized with the ND280 event display. The interaction vertex is inside the SFGD, and one of the charged particles, going downward in the picture, is crossing the HATPC.

I was in the control room when the global DAQ saw the first neutrino interactions in the

online event display of the detectors — a very emotional moment for everyone present. I was also there when the neutrino beam power reached the milestone of running stably at 760 kW. A press release followed the achievement of these goals [47].

In May 2024 the top HATPC was completed and also the SFGD electronics, while the TOF was already available at J-PARC. Another installation period followed the magnet opening before the closure for the neutrino Run 13, which started in June. The complete configuration of the Upgrade is shown in Figure 6.4, without the TOF panel covering the volume.

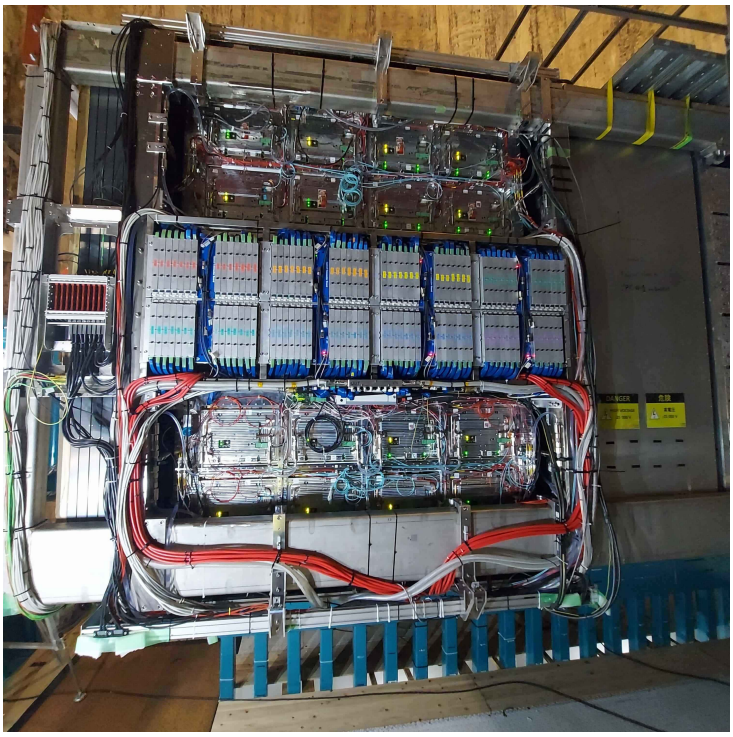

Figure 6.4: Photo of Upgrade detectors installed inside the basket.

One of the first recorded neutrino events is shown in Figure 6.5, displayed in the frame of the detectors. The neutrino interacts with the SFGD, and the particles generated in the interaction become visible from the tracks in the detectors. In this spectacular event, the magnetic field causes the spiral trajectories of some charged particles.
Run 13, which was recently concluded, successfully collected data with the fully upgraded ND280, marking a significant achievement for the T2K collaboration. In Figure 6.6, the updated POT plot is shown, now including data from both Run 12 and Run 13..

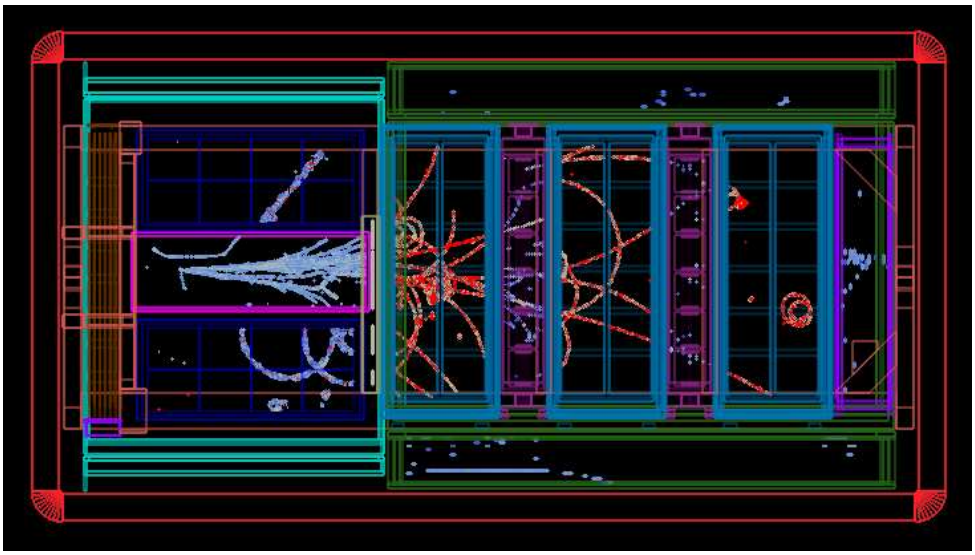

(a)

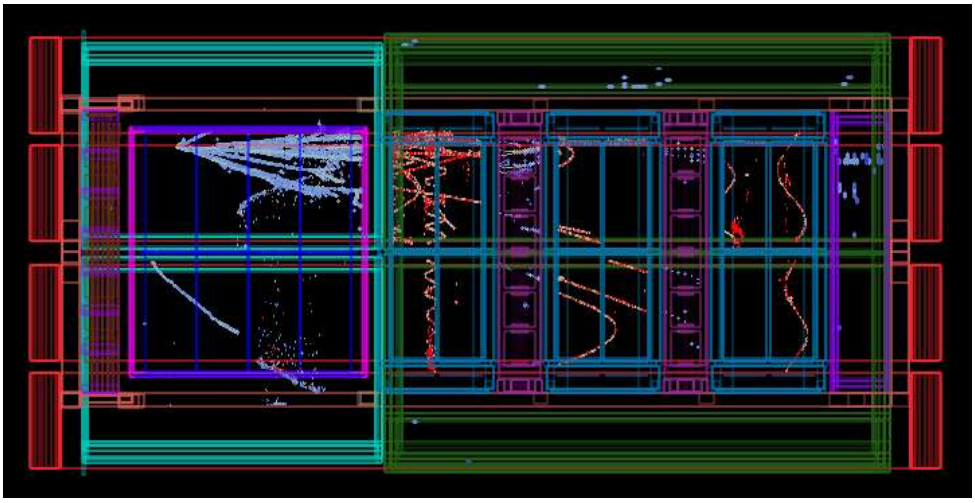

(b)

Figure 6.5: The neutrino interaction inside ND280 is shown in the ND280 event display, in which the upgrade detectors are enclosed within the turquoise box, representing the TOF. The detector displayed in pink is the SFGD, while the two TPCs are shown in blue at the top and bottom. In (a), the side view of the event is displayed, and in (b), the top view is provided.

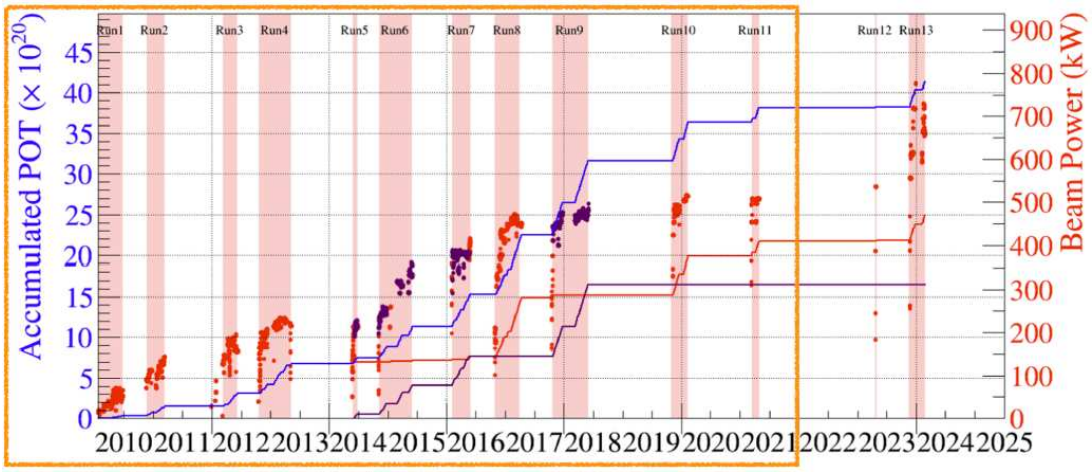

Figure 6.6: POT plot update with Run 12 and Run 13. The orange rectangle highlights the Runs with the original configuration. In the plot, the blue line is the trend of accumulated POT, the red line is the accumulated POT for neutrinos, and the violet is for antineutrinos.

Figure 6.7: Group photo at CERN.

Chapter 7

Conclusions

After reviewing the theoretical physics of neutrino oscillations in Chapter 1, the design and the results of the T2K experiment and the description of the Upgrade in Chapter 2, in Chapter 3 I describe the technical design of the HATPC and the experimental activities where I was involved.

I participated in the commissioning of the bottom HATPC at CERN laboratories, arriving at the laboratories just after the assembly phase. This thesis reports my experimental activities and the analysis results I obtained from data collected during the commissioning at CERN. My work was primarily experimental, involving several technical activities on the bottom HATPC. I contributed to the adjustment of the gas system, building pipes and junctions. I performed leakage tests to validate the TPC's tightness outside the clean room after the ERAM detectors were mounted. I definitely sealed the cathode junction, where the two field cages were assembled, using a specific glue and spraying anticorona lacquer on the entire junction and the cathode connector. Additionally, I was responsible for the cathode junction covering.
In this chapter, I also describe my contribution to the development and test of the "T2K HATPC monitoring system," which consists of two sets of sensors installed on two PCBs, with one PCB inside and one outside each field cage. This monitoring system provides data from each of the four FCs and gives information about both sides of the detector.

In Chapter 4, I discuss the measurement of drift velocity from cosmic ray data, which also implied a deep study of the gas properties. First, I verified that oxygen and water contamination during the purging phase followed the expected models and subsequently I demonstrated that the gas quality was sufficiently high to safely turn on the ERAM detectors. Specifically, I showed through some measurements that the oxygen and water content decreased gradually during the entire data collection period. This was a very positive result as it indicated that the gas quality improved over time. Additionally, the $\Delta P/\Delta T$ ratio remained mostly stable during the same period.
I was actively involved in setting up the detector for the cosmic data collection campaign, which was one of the most significant parts of the commissioning process. I participated in all stages of the setup and data collection, collaborating closely with other members of the research team throughout the entire duration of the activities.
In this chapter, I also detail my study on drift velocity measurements using cosmic data. I developed an algorithm to selectively identify cosmic ray tracks that traverse the anode and/or cathode of the HATPC. Utilizing this algorithm, I extracted a subset of events suitable for calculating the drift velocity for each ERAM module. Initially, I validated the algorithm's performance using data from a run where the trigger was configured to

capture only cathode-crossing tracks. This initial validation provided crucial insights into the algorithm's behavior. Subsequently, I applied the complete algorithm to two additional runs (named Run 26 and Run 45), complementary in the trigger coverage, taken at 5 days of distance. From these runs, I derived the drift velocity measurements for each ERAM module located on both endplates. The results are shown in Figure 4.25. The drift velocity mean difference between the endplates and between ERAMs in the same run is negligible and within the error bars. However, the drift velocities computed in the two runs are slightly different. The difference is explained in the better quality of the gas at five days of distance.

In Chapter 5, a Nd:YAG Q-switching laser was tested for calibration purposes to study the track characteristics inside the HATPC detector. Initially, I examined the shape of the tracks at the waveform level to understand the detector's response to the two charge production processes 5.2. The track in the gas is produced through two-photon ionization, resulting in very low amplitude waveforms collected from the pads. At the cathode, however, the charge is produced through the photoelectric effect. In this case, the waveform of the leading pad shows saturation of the readout electronics, and the charge spreading on the DLC generates signals in several neighboring pads.
The analysis of laser tracks can be summarized in three main goals. First, an unexpected modulation was found in the time spectrum, and the origin of this effect was unknown. By studying the distribution of the waveforms along the time axis, I found that the modulation comes from the pad shape of the ERAM detector, the way the signal from a pad is generated, the fact that tracks produced by the laser are straight, and the chosen horizontal direction of the laser beam. Fixing y, with the laser horizontal to the xz plane, the effect is that a single pad in x direction reads a single position of the tracks in z, showing a peak in the z axis for each pad along x. Second, I computed a estimation of the beam spot exploiting the PCA method to find the distribution of the points where the laser tracks cross the anode plane. In this way, I could evaluate the spreading of the tracks. I found that the measurements are compatible with the 3 mm nominal size on the laser data-sheet. The last part in Section 5.5 is devoted to the drift velocity calculation. I took several laser runs varying the cathode voltage from 10 kV to 30 kV at step of 2 kV. The results are shown in Figure 5.15 and 5.16, where the measurements beautifully follow the trend of the simulation.

Last but not least, during my thesis work, I had the opportunity to follow the first neutrino run since ND280's new switch-on, with part of the installed upgrade. When I was in J-PARC, I participated in all activities in the control room. I contributed to the efforts of running all detectors synchronously in the global DAQ, monitoring the HATPC functioning, and checking data quality parameters. I also learned a lot about the procedures for supervising data taking and ensuring detector functionality by shadowing the shifters in their tasks. I was present when the first neutrino interaction appeared in the ND280 detector event display.

Appendix A

Plots and technical schemes

A.1 T2K HATPC monitoring system

In this section, the schemes of the two PCB composing the T2K HATPC monitoring system are presented together with the two circuit technical projects. Figure A.1 (a) is the external PCB where the devices listed in Section 3.1.3 are soldered. Figure A.1 (b) is its correspondent internal PCB.

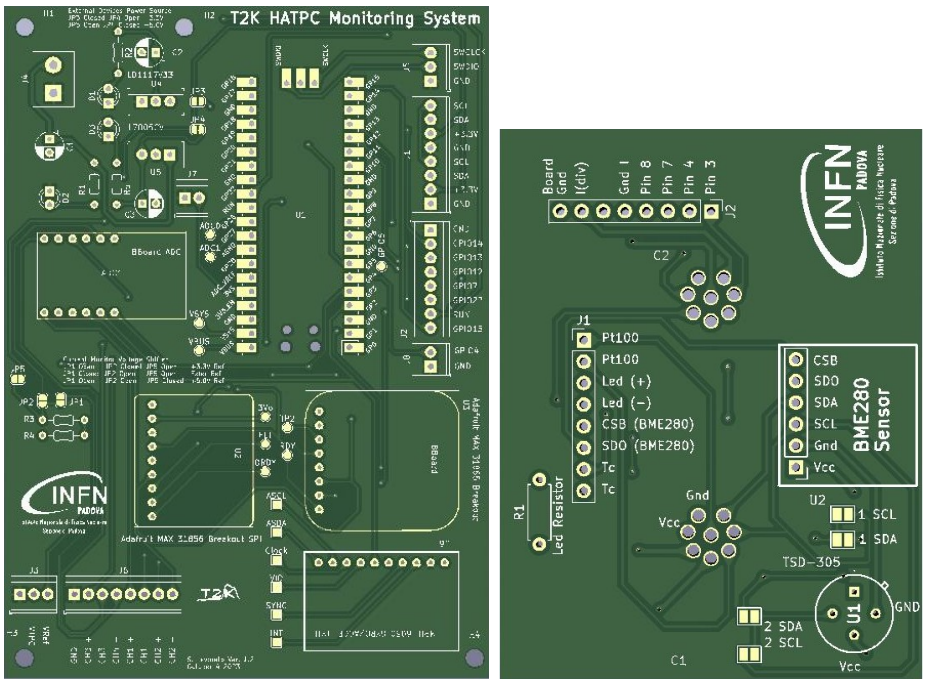

(a) (b)

Figure A.1: PCBs of the T2K HATPC monitoring system: (a) external (b) internal.

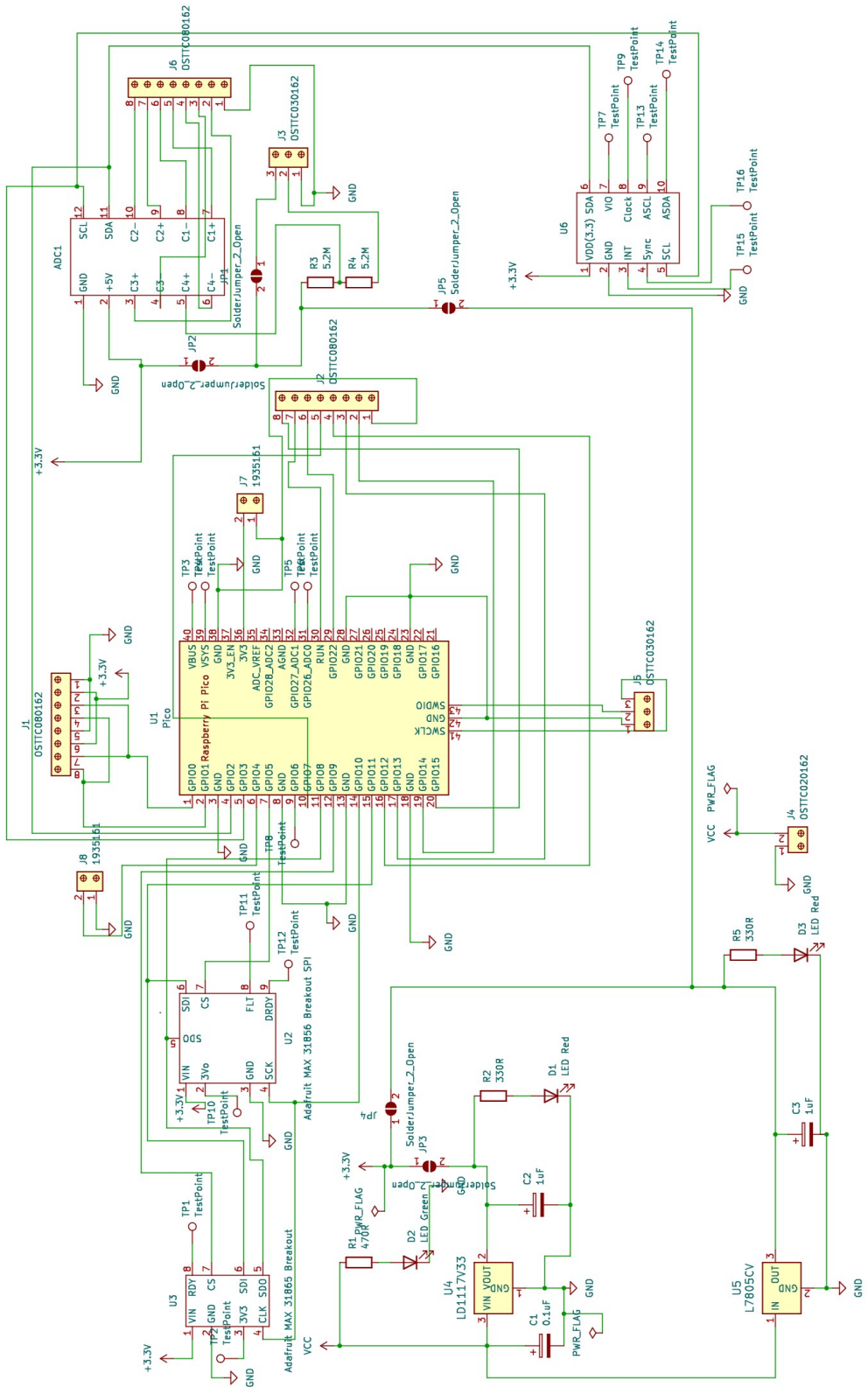

Figure A.2: PCB scheme with the Raspberry PicoPI 2024.

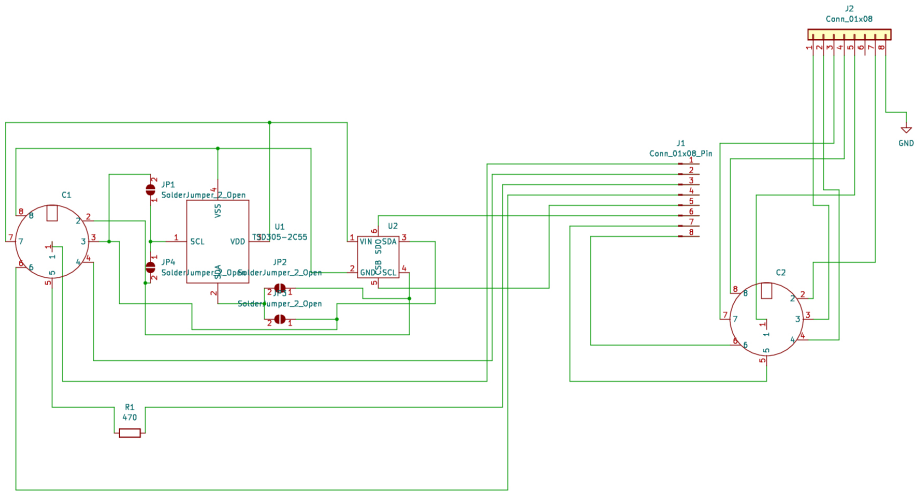

Figure A.3: Interface board circuit installed inside the Aluminum box in contact with the T2K gas.

A.2 Laser time spectrum additional plots

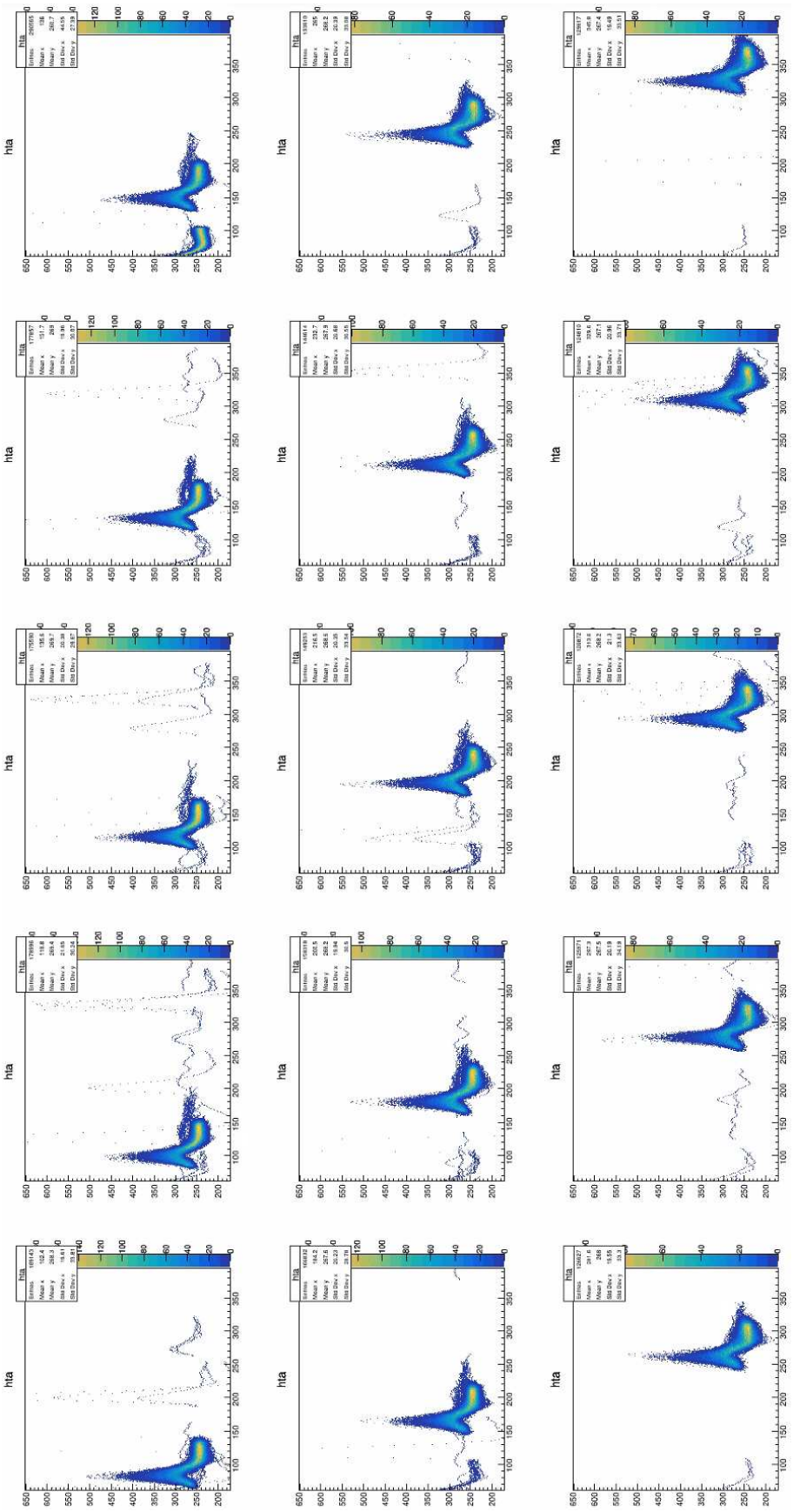

Figure A.4: Waveforms multiplot selecting the pad number in the x direction.

Bibliography

[1] K. Abe et al. The T2K Experiment. *Nucl. Instrum. Meth. A*, 659:106–135, 2011.

[2] K. Abe et al. Indication of Electron Neutrino Appearance from an Accelerator-produced Off-axis Muon Neutrino Beam. *Phys. Rev. Lett.*, 107:041801, 2011.

[3] K. Abe et al. Measurements of neutrino oscillation parameters from the T2K experiment using 3.6×10^{21} protons on target. *Eur. Phys. J. C*, 83(9):782, 2023.

[4] K. Abe et al. Constraint on the matter–antimatter symmetry-violating phase in neutrino oscillations. *Nature*, 580(7803):339–344, 2020. [Erratum: Nature 583, E16 (2020)].

[5] K. Abe et al. Hyper-Kamiokande Design Report. 5 2018.

[6] Y. Fukuda et al. The Super-Kamiokande detector. *Nucl. Instrum. Meth. A*, 501:418–462, 2003.

[7] K. Abe et al. T2K ND280 Upgrade - Technical Design Report. 1 2019.

[8] B. Pontecorvo. Mesonium and anti-mesonium. *Sov. Phys. JETP*, 6:429, 1957.

[9] B. Pontecorvo. Inverse beta processes and nonconservation of lepton charge. *Zh. Eksp. Teor. Fiz.*, 34:247, 1957.

[10] Ziro Maki, Masami Nakagawa, and Shoichi Sakata. Remarks on the Unified Model of Elementary Particles. *Progress of Theoretical Physics*, 28(5):870–880, 11 1962.

[11] R. L. Workman and Others. Review of Particle Physics. *PTEP*, 2022:083C01, 2022.

[12] Y. Fukuda et al. Evidence for oscillation of atmospheric neutrinos. *Phys. Rev. Lett.*, 81:1562–1567, 1998.

[13] F. P. An et al. Observation of electron-antineutrino disappearance at Daya Bay. *Phys. Rev. Lett.*, 108:171803, 2012.

[14] J. K. Ahn et al. Observation of Reactor Electron Antineutrino Disappearance in the RENO Experiment. *Phys. Rev. Lett.*, 108:191802, 2012.

[15] M. A. Acero et al. Improved measurement of neutrino oscillation parameters by the NOvA experiment. *Phys. Rev. D*, 106(3):032004, 2022.

[16] Q. R. Ahmad et al. Direct evidence for neutrino flavor transformation from neutral current interactions in the Sudbury Neutrino Observatory. *Phys. Rev. Lett.*, 89:011301, 2002.

[17] Eguchi et al. First results from kamland: Evidence for reactor antineutrino disappearance. *Phys. Rev. Lett.*, 90:021802, Jan 2003.

[18] J. H. Christenson, J. W. Cronin, V. L. Fitch, and R. Turlay. Evidence for the 2π Decay of the K_2^0 Meson. *Phys. Rev. Lett.*, 13:138–140, 1964.

[19] C. Jarlskog. Commutator of the Quark Mass Matrices in the Standard Electroweak Model and a Measure of Maximal CP Nonconservation. *Phys. Rev. Lett.*, 55:1039, 1985.

[20] A. G. Olshevskiy. Neutrino Oscillation Results and Search for Neutrino Sterile States. *Phys. Part. Nucl. Lett.*, 20(3):202–212, 2023.

[21] Babak Abi et al. Deep Underground Neutrino Experiment (DUNE), Far Detector Technical Design Report, Volume I Introduction to DUNE. *JINST*, 15(08):T08008, 2020.

[22] Angel Abusleme et al. JUNO physics and detector. *Prog. Part. Nucl. Phys.*, 123:103927, 2022.

[23] S. Assylbekov et al. The T2K ND280 Off-Axis Pi-Zero Detector. *Nucl. Instrum. Meth. A*, 686:48–63, 2012.

[24] N. Abgrall et al. Time projection chambers for the t2k near detectors. *Nuclear Instruments and Methods in Physics Research Section A: Accelerators, Spectrometers, Detectors and Associated Equipment*, 637(1):25–46, 2011.

[25] P. A. Amaudruz et al. The T2K Fine-Grained Detectors. *Nucl. Instrum. Meth. A*, 696:1–31, 2012.

[26] S. Fukuda et al. Solar B-8 and hep neutrino measurements from 1258 days of Super-Kamiokande data. *Phys. Rev. Lett.*, 86:5651–5655, 2001.

[27] A. Takenaka et al. Search for proton decay via $p \to e^+\pi^0$ and $p \to \mu^+\pi^0$ with an enlarged fiducial volume in Super-Kamiokande I-IV. *Phys. Rev. D*, 102(11):112011, 2020.

[28] A. Blondel et al. The WAGASCI experiment at JPARC to measure neutrino cross-sections on water. *PoS*, EPS-HEP2015:292, 2015.

[29] M. Antonova et al. Baby MIND: A Magnetised Spectrometer for the WAGASCI Experiment. In *Prospects in Neutrino Physics*, 4 2017.

[30] L. Munteanu, S. Suvorov, S. Dolan, D. Sgalaberna, S. Bolognesi, S. Manly, G. Yang, C. Giganti, K. Iwamoto, and C. Jesús-Valls. New method for an improved antineutrino energy reconstruction with charged-current interactions in next-generation detectors. *Phys. Rev. D*, 101(9):092003, 2020.

[31] S. Dolan, V. Q. Nguyen, A. Blanchet, S. Bolognesi, M. Buizza Avanzini, J. Chakrani, A. Ershova, C. Giganti, Y. Kudenko, M. Lamoureux, A. Letourneau, M. Martini, C. McGrew, L. Munteanu, B. Popov, D. Sgalaberna, S. Suvorov, and X. Y. Zhao. Sensitivity of the upgraded t2k near detector to constrain neutrino and antineutrino interactions with no mesons in the final state by exploiting nucleon-lepton correlations. *Phys. Rev. D*, 105:032010, Feb 2022.

[32] Y. Giomataris, P. Rebourgeard, J. P. Robert, and Georges Charpak. MICROMEGAS: A High granularity position sensitive gaseous detector for high particle flux environments. *Nucl. Instrum. Meth. A*, 376:29–35, 1996.

[33] Resoltech 1054: online datasheet. Available at: https://www.castrocompositesshop.com/img/cms/Resoltech%201050%20nueva%20English.pdf.

[34] Raspberry pi pico 2024: online datasheet. Available at: https://datasheets.raspberrypi.com/pico/pico-datasheet.pdf.

[35] Bme280 bosch: online datasheet. Available at: https://www.mouser.com/datasheet/2/783/BST-BME280-DS002-1509607.pdf.

[36] Mpu6050 sparkfun: online datasheet. Available at: https://cdn.sparkfun.com/datasheets/Components/General

[37] Max31856 thermocouple-to-digital converter: online datasheet. Available at: https://www.analog.com/media/en/technical-documentation/data-sheets/max31856.pdf.

[38] Max31865 resistance-to-digital converter: online datasheet. Available at: https://www.analog.com/media/en/technical-documentation/data-sheets/max31865.pdf.

[39] L. Ambrosi et al. Characterization of charge spreading and gain of encapsulated resistive Micromegas detectors for the upgrade of the T2K Near Detector Time Projection Chambers. *Nucl. Instrum. Meth. A*, 1056:168534, 2023.

[40] D. Attié et al. Analysis of test beam data taken with a prototype of TPC with resistive Micromegas for the T2K Near Detector upgrade. *Nucl. Instrum. Meth. A*, 1052:168248, 2023.

[41] Claudio Giganti. *Particle Identification in the T2K TPCs and study of the electron neutrino component in the T2K neutrino beam.* PhD thesis, IRFU, Saclay, 2010.

[42] Vaisala dmt152: online datasheet. Available at: https://docs.vaisala.com/v/u/B210750EN-M/en-US.

[43] F. Bellucci, I. Khamis, S.D. Senturia, and R.M. Latanision. Moisture Effects on the Electrical Conductivity of Kapton Polyimide. *J. Electrochem. Soc.*, 137:1778–1784, 1990.

[44] H. J. Hilke. Detector Calibration With Lasers - a Review. *Nucl. Instrum. Meth. A*, 252:169–179, 1986.

[45] Y. Cai, Y. Li, H. Qi, Y. Li, J. Yang, Z. Yuan, Y. Chang, and J. Li. Investigation of uv laser ionisation in argon-based gas mixtures with a triple-gem detector. *Journal of Instrumentation*, 15(02):T02001, feb 2020.

[46] Minilite nd:yag laser: online datasheet. Available at: https://www.photonicsolutions.co.uk/upfiles/DatasheetforMiniliteIandIILG07Dec17.pdf.

[47] ICRR. T2k experiment enters a new phase with significantly improved sensitivity for its world leading neutrino oscillation research, 2024.

Acknowledgements

I would like to sincerely thank all the people who supported me and allowed me to grow as a scientist and as a person during my Master's Degree in Physics.

My heartfelt thanks go to my supervisor, Prof. Gianmaria Collazuol, for inviting me to join the Test Beam activities at CERN in the summer of 2022, as part of the "Introduction to Research" exam. This experience was a crucial point in my scientific career, as it gave me the possibility to engage in real scientific research for the first time. Delighted to come back for a second extended period at CERN for the commissioning activities of the first HATPC while working on my thesis. I am also grateful for the opportunity of working in Japan at the J-PARC laboratories during the first neutrino run with upgraded detectors.

I wish to extend my thanks to my co-supervisor, Stefano Levorato, for all the technical expertise he taught me and for having been one of my greatest supporters in this significant moment.

I want to thank David Henaff for the hours spent doing data analysis together, for the daily meetings on zoom, and for sharing the happiness of understanding unknown features of the detector.

I would like to thank Mauro Mezzetto for reading and correcting my thesis, for the hours spent discussing neutrino physics, past and future experiments, and for agreeing to redo the seminar on long-baseline neutrino experiments in Padova.

I sincerely thank the T2K Padova group for having welcomed me as part of the team, in particular Matteo Feltre, Daniele D'Ago and Marco Mattiazzi.

I want to thank the T2K HATPC collaboration for the possibility of participating in the Collaboration Meetings and in the weekly analysis meetings, in particular Lorenzo Magaletti, Gabriella Catanesi, Emilio Radicioni, Thorsten Lux, Merlin Varghese.

I want to thank my family, my parents and my sister, for allowing me to complete my studies, for always cheering me on, and for encouraging me.

I want to thank my dear friend Francesco, for his infinite patience and his lectures that contributed to help me understand the most intricate exams.

I want to thank Matteo, for listening to me talking about detectors and neutrinos in every moment, for waiting for my return when I was abroad and for sharing all the happy and sad moments of this journey.